Mapping of strain mechanisms in barium titanate by three-dimensional X-ray diffraction

Majkut, Marta

Publication date:
2016

Document Version
Publisher's PDF, also known as Version of record

Mapping of strain mechanisms in barium titanate by three-dimensional X-ray diffraction

Marta Majkut

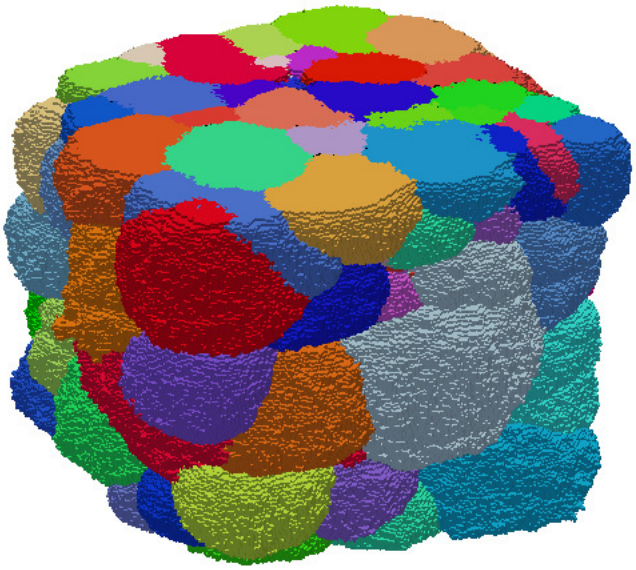

Kongens Lyngby 2016

Mapping of strain mechanisms in barium titanate by three-dimensional X-ray diffraction

Ph.D. thesis by

Marta Majkut

Supervisor: Søren Schmidt, Senior Scientist
Co-supervisor: Jette Oddershede, Research Engineer

March 2016

Neutrons and X-rays for Materials Physics
Department of Physics
Technical University of Denmark

Preface

The work presented in this thesis was conducted in the Neutrons and X-rays for Materials Physics (NEXMAP) group of the Department of Physics at the Technical University of Denmark under the supervision of Søren Schmidt and Jette Oddershede. Support for this project was provided by Danish Independent Research Council | Technology and Production Sciences case no. 12-127449. I would also like to acknowledge the The Danish Agency for Science and Technology for covering expenses in relation to synchrotron experiments (through Danscatt).

I would first like to thank my supervisors for the opportunity to work on this project and all of their support and guidance throughout my time here.

Thank you also to my colleagues and collaborators on this project: John Daniels from UNSW for an interesting and fruitful collaboration; Jonathan Wright at the ESRF and Peter Kenesei at the APS for support before, during, and after beamtimes; Hugh Simons for helpful discussions and proofreading.

A special thank you to my wonderful colleague and officemate Alberto, who has been there for me from the start.

Thank you also to the friends I have made at DTU: Falco, Simone, Elisa B., Elisa P. Ana Sofia, and Ivano; and those at GHK for all of the great times away from DTU, on and off the pitch.

Lastly, I want to thank my family: my dad Zbigniew, my mom Krystyna, my sister Aleks, and my brother Konrad, who have been so loving and supportive during my time here in Denmark and throughout my studies.

Abstract

This thesis presents an *in-situ* three-dimensional study of the grain-scale response of a prototypical piezoelectric ceramic, barium titanate (BT), to an exernally applied electric field. Piezoceramics take advantage of the coupling of electrical and mechanical energies for use in sensors and actuators, found in both common applications such as fuel injectors and specialized applications such as medical imaging equipment. Since piezoceramics are typically used in the polycrystalline state it is important to consider not just the crystal structure but also the role of intergranular effects in the structure-properties relationships. Such effects are difficult to observe using destructive two-dimensionsional microscopy techniques and averaged over the entire sample in conventional powder diffraction studies. We instead use a combination of non-destructive three-dimensional X-ray diffraction techniques to study the material at the grain scale.

First, we use the intensity ratios of split diffraction peaks to extract grain-scale domain volume fractions for 139 grains. We find that even in the as-processed state there exist unequal volume fractions of each domain type, which we attribute to a heterogeneous local environment at the cubic to tetragonal transition during processing. When a field is applied, we observe a first-order orientation dependence with second order deviations, again attributed to the grain neighbourhood effect. Corellation of this with microstructural parameters such as grain size, neighbour misorientation and position within the sample did not reveal any obvious causes.

Next we develop a novel indexing and refinement method whereby the peak positions of domains are forward projected from crystallographic twinning orienations and the deviation between projected and measured diffraction patterns is minimized to refine domain-scale orientations and lattice parameters. We present the results of refinement for a bulk grain in which the domains are found to be misoriented from perfect crystallographic twins by 0.1-0.3°, suggesting a strained microstructure. The data set was collected by illuminating the entire width of the sample with a box beam, thus it contains a statistically significant number of grains for which domain-scale parameters will be refined in the future.

Resumé

Denne afhandling omhandler et tredimensionelt in-situ studie af responset fra enkelte korn i en prototypisk piezokeramik, bariumtitanat (BT), som funktion af et eksternt påtrykt elektrisk felt. Den piezokeramiske kobling mellem elektrisk og mekanisk energi udnyttes i sensorer og aktuatorer, der bruges både til noget så dagligdags som brændstofindsprøjtning og i mere specialiserede anvendelser som eksempelvis udstyr til medicinsk billeddannelse. Fordi de anvendte piezokeramikker typisk er polykrystallinske er det vigtigt at tage højde ikke bare for krystalstrukturen, men også for effekten af korninteraktioner, i forholdet mellem struktur og egenskaber. Denne effekt er vanskelige at observere med destruktiv todimensionel mikroskopi, og der midles over mange korn ved brug af konventionel pulverdiffraktion. Vi benytter i stedet en kombination af ikke-destruktive tredimensionelle røntgendiffraktionsteknikker til at studere materialet på enkeltkornniveau.

Først har vi udnyttet intensitetsforholdet i splittede diffraktionstoppe til at beregne volumenfraktionen af forskellige domænetyper i 139 enkelte korn. Vi finder at selv i det nyfremstillede materiale er volumenfraktionerne af de forskellige domænetyper i et korn uens, hvilket vi tilskriver det heterogene lokale kornmiljø ved overgangen fra kubisk til tetragonal krystalsymmetri under fremstillingsprocessen. Når et elektrisk felt påtrykkes, observerer vi en førsteordens-sammenhæng mellem responset og orienteringen på kornniveau med andenordens-afvigelser, der igen tilskrives effekten af nabokorn. En sammenstilling af afvigelserne og mikrostrukturelle parametre som kornet størrelse, position i prøven og misorientering i forhold til naboerne afslører ikke umiddelbare korrelationer.

Dernæst har vi udviklet en ny metode til indicering og forfining af orienteringer og gitterparametre for domænerne i enkeltkorn. Metoden bygger på minimering af afstanden mellem de observerede diffraktionsmønstre og mønstre projiceret under antagelse af krystallografiske tvillingerelationer mellem domænerne. Vi præsenterer resultatet af forfiningen for et bulk korn, hvor domænernes orientering afviger 0.1-0.3° fra de perfekte krystallografiske tvillingerelationer, hvilket antyder at mikrostrukturen er deformeret. De eksperimentelle data er opnået ved at belyse hele bredden af prøven med røntgenstråling, så de indeholder information om et statistisk signifikant antal korn for hvilke domæneparametrene vil blive forfinet i fremtiden.

Introduction

Many industrial and scientific devices make use of the coupling between electrical and mechanical energies that is exhibited by some materials. One example of this is the piezoelectric effect, in which an electric charge is generated when a material is deformed, and conversely, a material deforms under an externally applied electric field. Most such devices are manufactured from polycrystalline ceramics, which exhibit a piezoelectric-like response that is actually due to ferroelectricity. A ferroelectric material exhibits a spontaneous polarization that can be reversed by an externally applied electric field or a mechanical stress.

Crystals of ferroelectric material are typically composed of regions with common a polarization called domains. Domains are seperated from regions with different polarization by domain walls. The domain walls are characterized by the angle between the direction of polarization of the adjacent domains, for example 180° in the case of anti-parallel directions and non-180° otherwise. Because the polarization is intimately linked with the crystal structure, the domains also represent reorientations of the crystal. When a mechanical stress or electrical field is applied the polarization may be switched and a portion of the crystal reoriented. Considering, for example, a tetragonal crystal, domain switching results in a net strain in the grain as the elongated c-axis is reoriented towards another direction. This is referred to as the non-180° switching strain, or the extrinsic strain, and represents a large contribution to the overall piezoelectric response of the material. There is also a contribution from the displacement of atoms in the lattice called the intrinsic strain.

In a polycrystal the material response is complicated because the grains must respond together, and in doing so, impose constraints on one another. These constraints can play a role even in the as-processed material. For example, in the case of a tetragonal ferroelectric, the domain structure is formed when the material cools through the transition temperature during processing. Heterogeneities in the state of stress of different grains can affect the resulting domain structure. When an electric field or mechanical

stress is imposed, the effect of neighbour grains may serve to either enhance or inhibit a response. Such local effects are difficult to observe since microscopy methods are destructive and two-dimensional, and powder diffraction methods average the response for all crystals in the specimen.

In this thesis, we develop two novel methods for studying domains at the grain scale, in a bulk polycrystalline sample. We strive to provide a comprehensive data set that cen be used for phenomenological considerations and statistical analyses, as well as input for models and simulations.

This thesis is divided into five chapters, with publications stemming from this work included in the Appendix:

- In Chapter 1, basic concepts of ferroelectricity are introduced. The work to be presented is placed in the context of both the development of lead-free materials as well as the growing field of computational materials science as a whole.
- In Chapter 2, X-ray diffraction concepts are introduced and explained. The characteristics of synchrotron radiation are discussed with reference to the experimental work of the thesis, which is a combination of two three-dimensional X-ray diffraction techniques. Emphasis is placed on the specific requirements for such experiments and the information that can be obtained from them.
- In Chapter 3 the experimental details and data analysis procedures are described. A novel technique for extracting grain-scale non-180° switching strains is introduced, and detailed results pertaining to the experimental work of this thesis are presented. Chapter 3 contains a technique description that is the subject the included Paper III, a brief comparison of results published in Paper IV, and the majority of results that are the subject of a submitted paper, Paper II.
- In Chapter 4 the diffraction data is closely examined for a select few grains in order to gain insight into the crystallographic structure and relationship of twin domains. A new procedure for indexing and refinement of domain-scale parameters is described and perspectives for further development and up-scaling are discussed. The work is included as a brief abstract in Paper I, to be published in the future.
- In Chapter 5 the goals of the study are reiterated and again placed in the context of comprehensive three-dimensional studies and computational materials science approaches.

Contents

Preface **i**

Introduction **vii**

1 Piezoceramics in the past, present, and future **1**
1.1 Domains and domain wall motion 7
1.2 PZT-based piezoceramics 13
1.3 Modeling and simulations 14
1.4 Lead-free alternative piezoceramics 16

2 Structural characterization by high-energy X-ray diffraction **19**
2.1 The crystal lattice 20
2.2 X-ray diffraction by crystalline materials 22
2.2.1 Diffraction by a rotated crystal 23
2.3 X-ray sources 26
2.3.1 High energy X-rays for materials science 26
2.4 Three-dimensional X-ray diffraction 29

3 Evolution of non-180° domain volume fractions on the grain scale **31**
3.1 Mapping the grain structure 32
3.2 Mapping the grain-scale non-180° switching strain 35
3.3 Strain response heterogeneity 41
3.4 Ferroelastic strain response as a function of grain orientation 42
3.5 Effect of grain size and bulk location 45
3.6 Effect of grain neighbour relations 47
3.7 Quantification of grain interactions by experiments and modelling . . . 50
3.8 Conclusions and perspectives 51

4 Indexing and refinement of domain-scale parameters **53**
4.1 Forward projection 57
4.2 Feasibility study for a single grain 64
4.3 Domain-scale orientations and lattice parameters 69
4.4 Conclusions and Perspectives 71

5 Conclusions **73**

Bibliography **75**

Included Papers **81**
Paper I: Grain-scale domain orientations and lattice parameters in a bulk barium titanate ceramicmeasured by three-dimensional X-ray diffraction (*Abstract*) 83
Paper II: Ferroic Material Response Resolved at the Grain-Scale (*Submitted*) 87
Paper III: Quantitative grain-scale ferroic domain volume fractions and domain switching strains from threedimensional X-ray diffraction data . . 125
Paper IV: Heterogeneous grain-scale response in ferroic polycrystals under electric field 135

Chapter 1

Piezoceramics in the past, present, and future

Electrical phenomena of solid materials have fascinated us since long before we could explain them or conceive of their practical applications. The word 'electric' actually comes from the Greek word for amber, *elektron*, which develops attractive forces when rubbed due to the build up of triboelectricity and can pick up light objects such as dust and feathers. Tourmaline, a crystalline boron silicate mineral, in which the electric properties are actually temperature dependent, was thought to possess magical or medicinal powers. [1] When heated, it attracts small objects such as dust or ashes and was also used to clean smoking pipes. It was not until the 1800s and the development of a more systematic and rigorous study of the natural world and its materials that we began to understand the origins of these phenomena. Mineralogists recognized and classified crystal symmetries, first by observing the natural habit planes of rocks and minerals and then using polarized light techniques developed by Sir David Brewster. Brewster introduced the term *pyroelectricity* to describe the temperature-dependent effect observed in tourmaline and other materials in 1824. [2] Pyroelectricity is defined as :

> ... the property presented by certain materials that exhibit an electric polarization P_i when a temperature variation $\delta\Phi$ is applied uniformly:
>
> $$P_i = p_i^T \delta\Phi \tag{1.1}$$
>
> where p_i^T is the pyroelectric coefficient at constant stress. [3]

To demonstrate, consider a thin sample of tourmaline cut so the axis of symmetry is perpendicular to the flat surfaces, shown schematically in Figure 1.1. The unit cell of a pyroelectric material has a permanent dipole moment, and the dipoles add up in the direction normal to the flat surfaces. The dipole moment per unit volume is called the spontaneous polarization, P_s. This moment is balanced by nearby free charges, such as electrons and ions, which are attracted to its surface. When heated or cooled the magnitude of the dipole moment changes, changing P_s as well as the quantity of bound charge on the surface. If the two opposite faces of the material are coated with a conductive electrode and connected in circuit with an ammeter, the redistribution of these surface charges (to balance the new dipole moment) can be measured as a current, flowing only while dT/dt is non-zero. This explanation was unknown to Brewster, but he observed the 'electricity' with an electrified needle as well the attraction and repulsion of light bodies. Brewster additionally noted that all of the crystals identified as pyroelectric had a similar number and arrangement of habit planes, early recognition of the relationship between crystal symmetry and electrical properties.

The French physicist Pierre Curie also had an interest in both pyroelectricity and early crystallography, which led him to postulate that electrical effects could be induced in these crystals in other ways, such as through pressure. Together with his brother Jacques, he prepared crystals of well-known pyroelectric materials such as tourmaline, Rochelle salt ($KNaC_4H_4O_6{\cdot}4H_2O$), and quartz, with parallel flat faces as in Figure 1.1. By connecting the crystals in a circuit, they measured a current when the crystals were compressed and a current of the opposite sign when the crystals were put into tension, thus proving the effect. [5] The converse effect, a mechanical strain from an applied electric field, was predicted by Lippmann [6] in 1881 from thermodynamic principles and also demonstrated by the Curies. [7] The phenomenon would come to be known as *piezoelectricity*, from the Greek word *piezin* meaning 'to squeeze' or 'to press', and is defined as:

> ... the property presented by certain materials that exhibit an electric polarization when submitted to an applied mechanical stress such as uniaxial compression. Conversely, their shape changes when they are submitted to an external electric field; this is the converse piezoelectric effect. [8]

Both the piezoelectric and converse piezoelectric effects are described by a tensor of rank 3. Assuming ideal linear behaviour, the polarization P_k due to a stress T_{ij} is given by:

$$P_k = d_{kij} T_{ij} \tag{1.2}$$

and the strain due to an applied electric field is given by:

$$S_{ij} = d_{ijk} E_k \tag{1.3}$$

where d is the piezoelectric constant and equal in magnitude for both the direct and converse effects, but expressed in coulombs/Newton for the former and meters/Volt for the latter. A high d constant is desirable when a large motion is required, for example, the generation of vibration. In practical applications the uniaxial case is often of

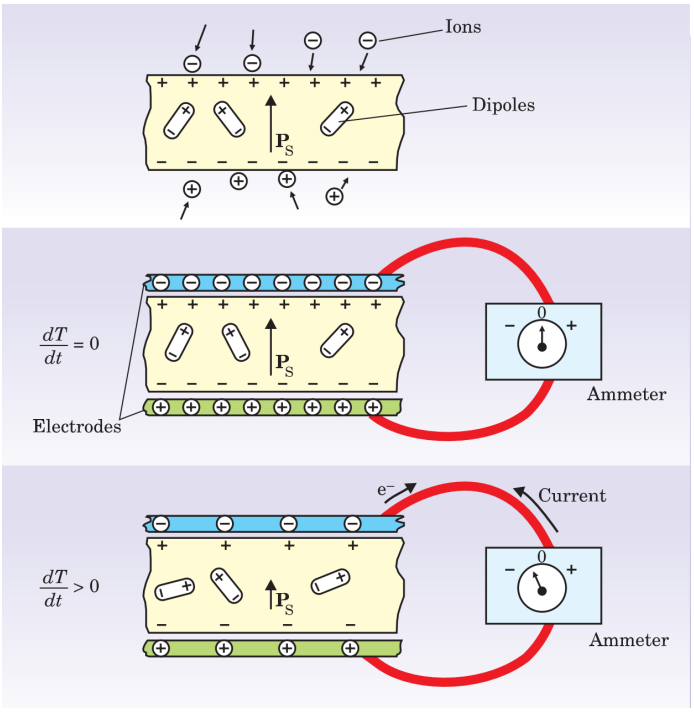

Figure 1.1: If a pyroelectric crystal with an intrinsic dipole moment (top) is fashioned into a circuit with electrodes attached on each surface (middle), an increase in temperature T prompts the spontaneous polarization $\mathbf{P}_s$ to decrease as the dipole moments, on average, diminish in magnitude. The horizontal tiling of the dipoles, pictured at the bottom, signifies the effect. A current flows to compensate for the change in the bound charge that accumulates on the crystal edges. [4]

the most interest and it is common to refer only to d_{33}, the piezoelectric constant along the direction of applied stress or electric field. A closely related non-linear phenomenon is an effect known as *electrostriction* and it is important to distinguish it from piezoelectricity. Electrostriction is exhibited by all dielectrics (non-conducting materials) and is related to the applied field quadratically (proportional to the square of the field). Thus, the sense of strain due to piezoelectricity changes sign when the sign of the applied electric field is changed, which is not the case for the quadratic electrostriction effect.

The applications of piezoceramics became more widely apparent during WWI when an improved underwater submarine detection method was needed. Paul Langevin, another French physicist, began developing a 'sandwich' transducer, a device that could convert electrical energy to mechanical energy and vice versa. The device was a mosaic of quartz crystals arranged in between two steel plates that vibrated in resonance when a voltage of the correct frequency was applied. This vibration generated ultrasonic waves in water which could then theoretically echo off any underwater structures. Operators could then listened for this echo to detect submarines. He shared his findings with British and North American colleagues at a conference in 1917, who quickly began working on their own versions of the device. Although they did manage to detect an echo from a piece of sheet metal at 200 m distance, the technology would require further development in the postwar period to be feasible, and eventually lead to sonar (originally an acronym for SOund Navigation And Ranging) [9, 10]. Today, sonar is also used in non-military applications such as fish finding and mapping of the sea bed.

The piezoelectric materials studied by Brewster, the Curies, and Langevin were single crystals, but most commercial sensors and actuators are actually polycrystalline ceramics. The birth of piezoelectric ceramics and their ubiquity in today's industries is owed to a discovery made while trying to explain some peculiarities in Rochelle salt, which by the 1920's was rather well studied. The piezoelectric response was expected to be linear but measurements indicated that it was initially more quadratic before increasing less and less and eventually reaching a saturation point. Additionally, the dielectric constant appeared to be a function of the applied field. To investigate this, Josef Valasek obtained two large crystals of Rochelle salt and began a comprehensive study of the macroscopic properties such as the linear and nonlinear dielectric responses, piezoelectric response, refractive index measurements, etc. Since he had previously worked with magnetic properties of ferromagnets, he recognized this behaviour as hysteresis, stating that the "dielectric displacement D, electric intensity E, and polarization P ... are analogous to B, H, and I in the case of magnetism" [11], where B is the flux density, H is the field strength and I is the current. He also noted that Rochelle salt has a "permanent polarization in the natural state" and published the first polarization hysteresis curves demonstrating the phenomenon that he called *ferroelectricity*, shown in Figure 1.2(a).

Another peculiarity of Rochelle salt was the presence of piezoelectric activity itself since, at the time, Rochelle salt crystals were determined to be orthorhombic. This contradicted *Neumann's principle*, which states that the symmetry elements of a property of a crystal must include the symmetry elements of the point group of a crystal,

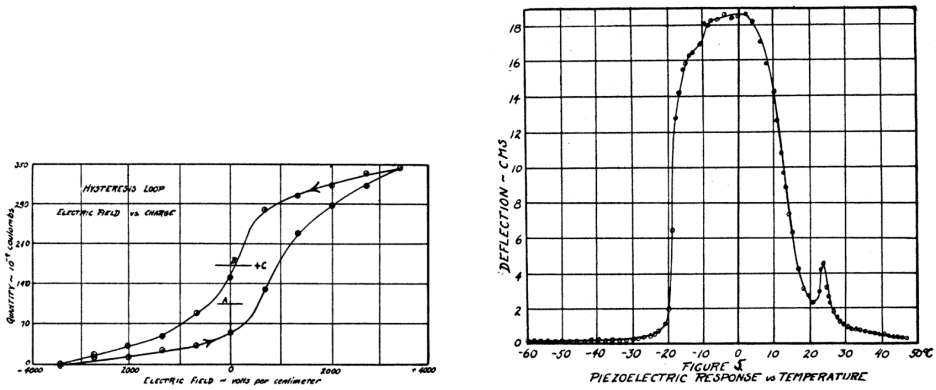

(a) (b)

Figure 1.2: (a) The first published hysteresis curve [11] and (b) the piezoelectric activity of Rochelle salt as a function of temperature, indicating the existence of two Curie points (phase transitions). [12]

and forbid piezoelectricity in the orthorhombic class. Additionally, piezoelectric activity was confined to a rather narrow temperature range with an abrupt increase at -20°C and and abrupt decrease +20°C as shown inf Figure 1.2(b). [13] Valasek called these the 'Curie points' continuing the analogy with ferromagnetism where the Curie point is the temperature at which there is a transition from paramagnetism to ferromagnetism. This was eventually explained by Hans Jaffe, who identified the monoclinic phase in between the two Curie points, a crystal symmetry that allows for piezoelectricity. [12]

Ferroelectrics are now considered to belong to a broader group of materials called *ferroics*, a term 'introduced ... to describe materials that show switchable properties under an external stimulus' [14], the switchable property being polarization in the case of ferroelectric materials and magnetism in the case of ferromagnetic materials. As mentioned earlier, pyroelectric materials also possess a spontaneous polarization, however, they differ from ferroelectrics in that the polarization is not always reversible. Piezoelectric materials are polarized by an applied stress but the polarization is not necessarily permanent. Thus, we can summarize as such: All ferroelectrics are pyroelectric, and all pyroelectrics are piezoelectric. We must also take care to reserve pyroelectricity to refer to changes in polarization resulting directly from a change in temperature, and not from any temperature associated deformation that would make it piezoelectric in origin. These relationships and properties are summarized in Figure 1.3.

Until the 1940s our knowledge of ferroelectrics was mostly limited to the famous Rochelle salt, potassium dihydrogen phosphate (KH_2PO_4, ferroelectric properties discovered in 1935 [16]) and some closely related compounds, but the next 15 years would bring about great changes by way of three key developments:

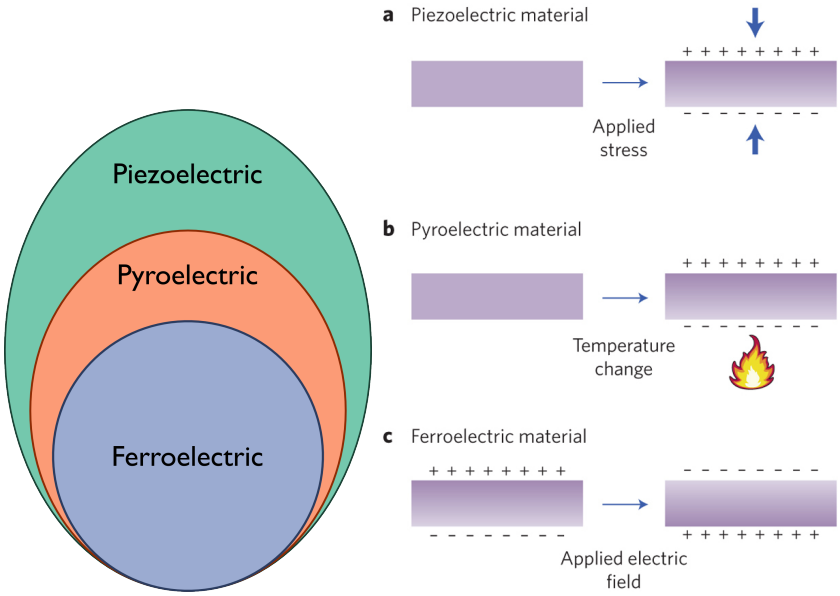

Figure 1.3: (L) Classification of dielectric materials.(R) (a) In piezoelectric materials, the coupling between mechanical and electrical energy results in an electric polarization when stress is applied. (b) The polar axis of a pyroelectric material allows a net polarization when the temperature is changed. (c) Ferroelectrics are a special subset of pyroelectrics, in that their polarization can be reversed on the application of an electric field. All ferroelectrics are both pyroelectric and piezoelectric. From: Keppens (2013). [15]

1. The discovery of the high dielectric constant in barium titanate
2. The realization that this high dielectric constant is due to ferroelectricity
3. The discovery of the poling procedure in polycrystals

Much of the work was industrially motivated and conducted within the R&D departments of engineering corporations. The high dielectric constant in oxide ceramics was first reported by researchers Hans Thernauer and James Deaderick at the American Lava Co. [17, 18] in the early 1940s, work that was followed up by Eugene Wainer and A.N. Salomon of the Titanium Alloy Manufacturing Company [19, 20]. Especially important was Wainer's discovery that the oxide ceramics could be used for electrical applications at elevated temperatures, a key limiting factor of Rochelle salt and other natural minerals. The first ceramics to be investigated included oxides such as barium titanate, magnesium titanate, titanium dioxide, and mixtures thereof. Since information sharing was limited during the Second World War, the high dielectric constant of barium titanate was actually discovered independently more than once, in the US as mentioned previously, in Japan by Ogawa [21] and in the Soviet Union by Wul and Goldman [22]. The source of this high dielectric constant was discovered to be ferroelectrcitiy by Arthur R. von Hipple, who published the work with his colleagues in 1946 [23]. In the paper, they demonstrate very clearly ferroelectric hysteresis loops for barium titanate ($BaTiO_3$, abbr. as BT) at temperatures ranging from -175°C to +125°C.

1.1 Domains and domain wall motion

The discovery of piezoelectricity in BT was surprising because it was not clear how the effect could occur in polycrystalline materials. Even though the individual crystals may be highly piezoelectric they are randomly oriented and the aggregate effects should be self-cancelling. The study of piezoelectric activity in BT actually began with single crystals, first obtained by Blattner, Matthias, Merz and Scherrer in 1947 [24]. Using a polarized light microscope, Matthias and von Hippel [25] saw a variety of shaded areas in crystals that were at room temperature. When an electric field was applied to these crystals, new shaded areas appeared. When the field was removed, some of these shaded areas remained (a remanent state) and required a reverse field for removal. An example of this effect is shown in Figure 1.4.

The explanation of these shaded regions lies in the crystal structure. BT is a perovskite crystal of the structure shown in Figure 1.5, and is a prototypical piezoceramic. As the crystal cools through the Curie temperature, around 120°C, a polar axis develops by the displacement of the central titanium atom and causes a phase transformation from cubic to tetragonal. The lattice parameters evolve according to the temperature dependence of BT unit cell dimensions in Figure 1.6. Any of the original six cubic directions can develop into the polar c-axis, resulting in the formation of regions of homogeneous polarization called *domains*. Domains are separated from adjacent regions of differing polarization by *domain walls*, which are defined by the relative

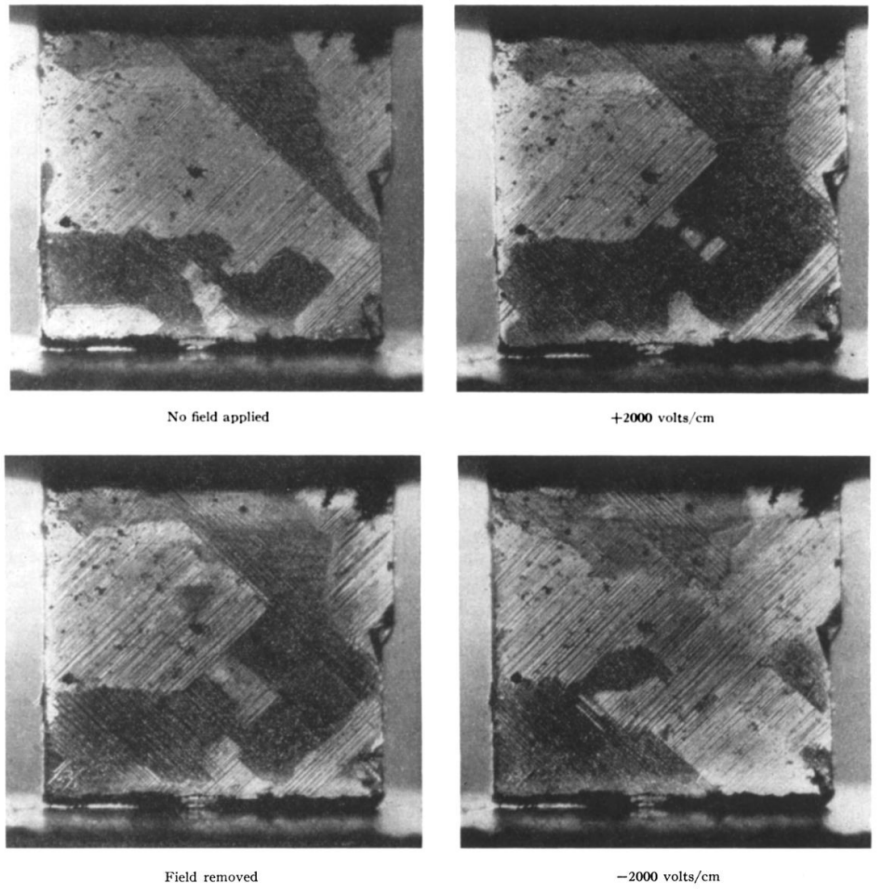

Figure 1.4: Effect of electric field on domain structure of $BaTiO_3$ crystal. [25]

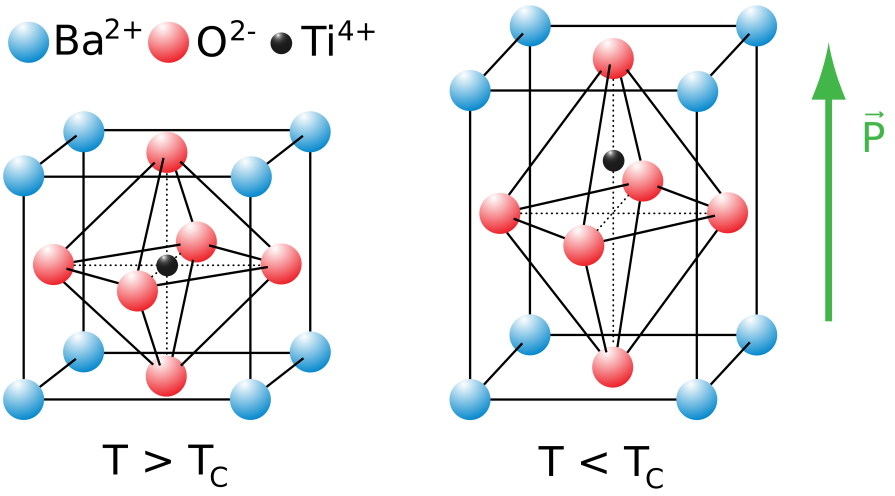

Figure 1.5: Barium titanate perovskite unit cell, cubic above T_c (left) and tetragonal below T_c (right).

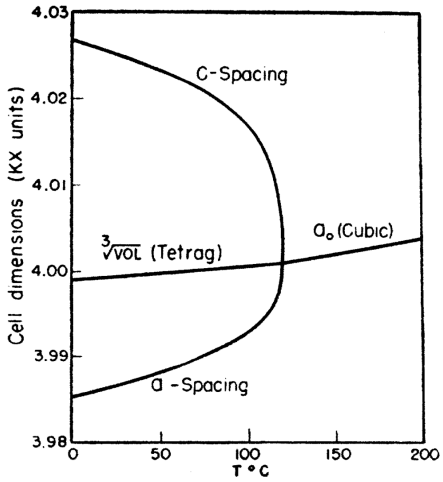

Figure 1.6: Variation of cell dimensions of barium titanate with temperature. [26]

angle between the polarization axes of the adjacent regions: 180° in the case of anti-parallel polarization and non-180° otherwise. Domain walls are coherent boundaries and this coherence is achieved by twinning, which, in the tetragonal case, means the non-180° domains are at approximately 90°. These non-180°domains are the source of the shaded regions that Matthias and von Hippel observed as a result of birefringence, which yields polarization contrast due to a difference in refractive index of differently polarized regions of the crystal.

When twinning occurs as a result of mechanical deformation, commonly in metals, the effect is a reduction of mechanical stress fields. It is thought that twinning plays a similar role in ferroelectric domain formation, in which additional energies must be considered. Arlt [27] outlined the relevant energy contributions as:

$$w_{tot} = w_M + w_E + w_W + w_S = \text{minimum} \tag{1.4}$$

where w_M is the elastic energy, w_E is the electric energy, w_W is the domain wall (or interface) energy and w_S is the surface energy, in terms of the energy density. The microstructure forms such that total energy is minimized. The situation in ceramics is necessarily more complex than in single crystals due to the presence of pores and grain boundaries, resulting in the lamellar and herringbone microstructures shown in Figure 1.7(a). The effect of clamping by neighbour grains on the domain pattern is demonstrated clearly by the same grain when the pattern is formed under free surface conditions, as in Figure 1.7(b).

The total response of the piezoceramic to an applied electric field or mechanical stress includes *intrinsic* and *extrinsic* contributions. The intrinsic contribution is from the deformation of the unit cell under an external applied field or mechanical load and the external contribution is due to domain wall motion and point defects. The motion of non-180° domain walls results in macroscopic strain since the elongated tetragonal axis of part of the crystal is reoriented, as shown schematically for two crystallites in Figure 1.8. The room-temperature contributions to piezoelectric response from extrinsic effects can be greater than 30% [28, 29], thus, the nature of domains and domain wall motion have been studied in great detail since they were first observed, both experimentally and theoretically. A comprehensive review was recently conducted by Pramanick et al. [30]. Domain switching has been found to depend on grain size, which has been attributed to the domain width and some optimal domain wall density that enhances domain wall motion [31]. Domain switching can also be affected by back stresses that oppose switching and assist back-switching. Additionally, TEM studies have revealed coupling of domains even across grain boundaries [32], with long- and short-range order, gradient organization, and radial organization. Large strain fields have been measured around domain walls of single crystal BT [33], even at the crystal surface, and competing interactions between domains of polycrystals have been shown to result in local symmetry breaking [34], which appears to enhance piezoelectric response. Such results point to the complexity of the materials but also the potential of engineering domains to produce ceramics with desired properties.

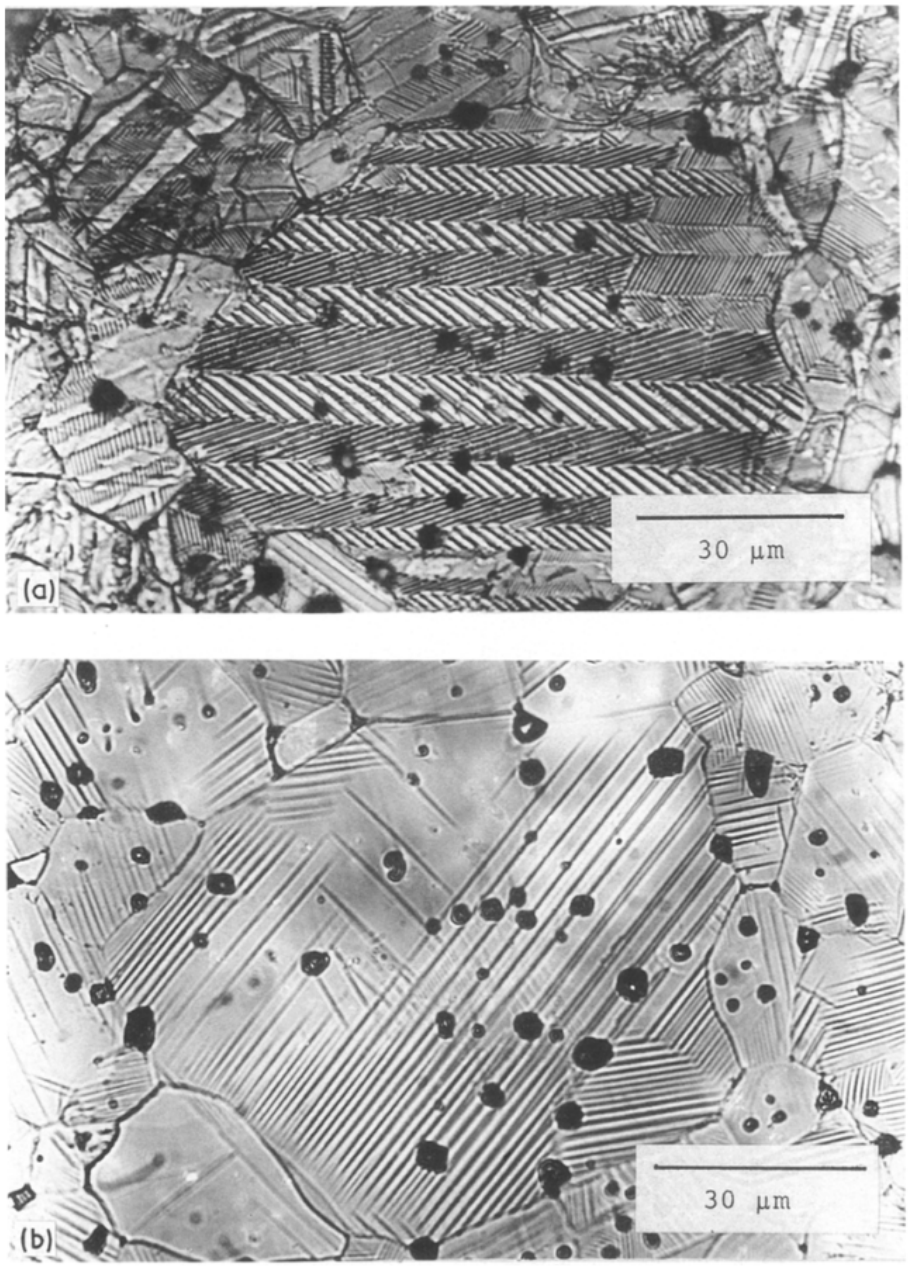

Figure 1.7: Representative BT domain patterns of a grain (a) when the pattern is formed inside the ceramic body with three-dimensional clamping, (b) the same grain when the pattern is formed under free surface conditions. [27]

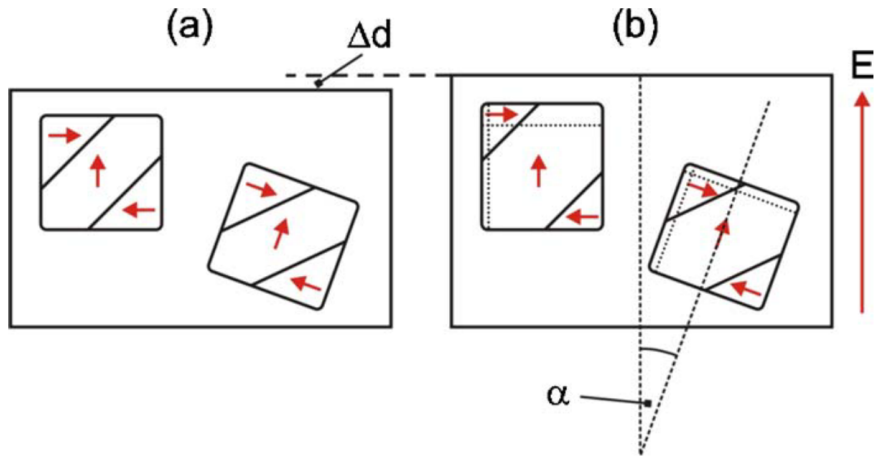

Figure 1.8: Schematic diagram of the induced macroscopic strain resulting from ferroelastic domain switching in grains of different orientations, (a) at zero applied field and (b) at an applied external field. Dashed lines within each grain indicate their changes in geometry. [35]

Let us now explore the origins of the piezoceramic hysteresis loop, referring to steps A-G in Figure 1.9(a). In the as-processed state (A), ceramic specimens of ferroelectric materials are, in fact, non-piezoelectric, since the dipoles of the various domains are self-cancelling. However, applying an external electric field will cause domains with a polarization direction highly misoriented with the electric field direction to switch to a variant that is more closely aligned. It is common to apply an electric field while the ceramic cools through the Curie point since the dipoles are most easily aligned as they form spontaneously, a process first described by Robert B. Gray in 1946 [36], the originator of the poling procedure. This results in a rapid increase in the measured charge density following the dashed line from A towards B. Once most of the domains are aligned the behaviour is roughly linear, reaching a saturation point (B). When the field is removed, some of the domains switch back but at zero field there is a remanent polarization, P_R (C). Reversing the direction of the field causes the rest of the domains to switch back and a state of zero polarization is reached (D). Increasing the magnitude of the negative field will cause the dipoles to align in the negative direction and another saturation point is reached (E). Decreasing the field to zero again results in a remanent polarization (F), this time in the negative direction. As with the negative case, a positive applied field is required to bring the polarization to zero (G). The field strength at which this occurs is called the coercive field, E_c. The effect on strain is demonstrated in Figure 1.9(b) where S_R is the remanent strain at zero field. The process of aligning domains in a polycrystal is called poling. A poled ceramic has a net dipole moment and will react similarly to a single crystal (linearly) to an electric field or mechanical pressure, as long as they are well below the magnitude

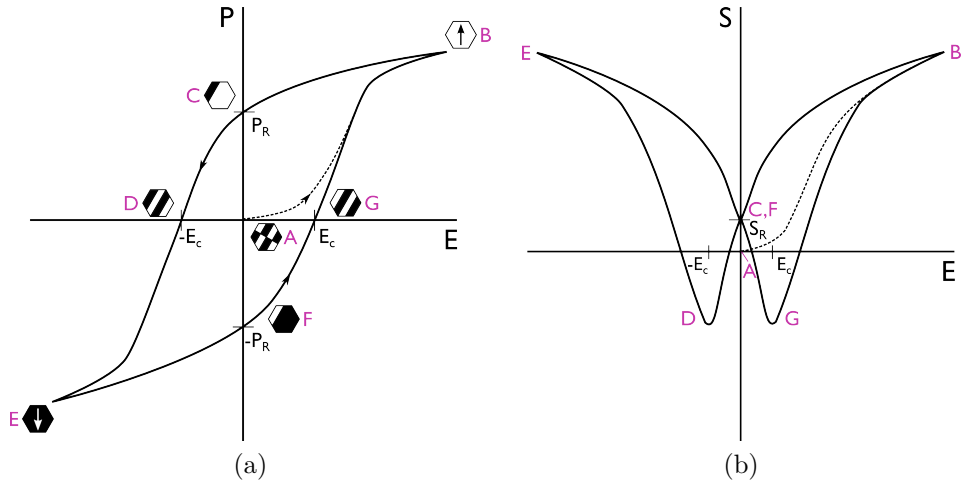

Figure 1.9: Role of domain wall motion in polarization hysteresis and strain 'butterfly' loops.

needed to switch the polar axis. Since the grains are randomly oriented and domain reorientation is limited to directions allowed by crystal symmetry a polycrystal never reaches the spontaneous polarization of a single crystal, instead reaching a saturation value as described previously.

1.2 PZT-based piezoceramics

Many more piezoceramics have been discovered since BT, of which those with the perovskite crystal structure have become the most economically important. This is mostly due to the discovery of a high dielectric constants in another class of perovskites of lead and zirconium, the lead-zirconate-titanate (PZT) system. Shirane, Suzuki, and Takeda [37, 38] identified a ferroelectric phase of solid solution (Pb-Zr)TiO_3 containing more than 10 molar % $PbTiO_3$ as well as a phase boundary between rhombohedral to tetragonal symmetries at 45 mol % $PbTiO_3$. The piezoelectric coefficients at compositions near this morphotropic phase boundary (MPB) are enhanced [39] due to increased mobility of domain walls. The first PZT-based transducer was patented by Bernard Jaffe in 1954 [40] and PZT ceramics came to dominate in industrial applications. Values of piezoelectric coefficients for PZT are in the range of 100-500 pm/V or pC/N [41], compared with only 190 pm/V or pC/N for typical BT ceramics [42]. PZT-based piezoceramics also offer a significant advantage over their BT counterparts due to a higher Curie point (between 220°C and 490°C, depending on the composition) and better temperature stability. Another advantage of the PZT system is the ability to alter the hysteresis loop through doping and substitution, making it more linear or

non-linear, with stronger or weaker hysteresis. [42]

1.3 Modeling and simulations

Many materials are developed by trial and error, through alterations of the compositions and processing parameters until the desired properties are attained. If the material is well understood, modelling and simulations can help us choose compositions and processing techniques that are more likely to yield the desired result before extensive testing is undertaken. This is, of course, not yet a reality for most materials, but some approaches to modelling will be discussed here.

The same year that Jaffe identified the monoclinic phase as the source of ferroelectricity (1937) and Curie points in Rochelle salt, Soviet physicist Lev Landau published his work "On the theory of phase transformations" [43], a symmetry-based analysis of equilibrium behaviour near a phase transition. These two discoveries were very important for driving the theoretical understanding of ferroelectrics. In general, Landau stated that a system cannot change smoothly between two phases of different symmetry and that the thermodynamic state of the two systems must be equivalent at their shared transition line. This means that the symmetry of one phase must be higher than that of the other. He then introduced the *order parameter*, a quantity that describes the degree to which a crystal state deviates from an ordered one, equal to 1 in the completely ordered state and 0 in the completely disordered state. The theory was applied to ferroelectrics by Landau's Soviet colleague Vitaly Ginzburg in 1945 [44], but it was unknown in Europe and North America because Ginzburg was publishing in Russian during the Cold War. Around the same time, similar work was being done by Devonshire, and the theory is sometimes referred to as Ginzburg-Landau-Devonshire theory.

For the paraelectric to ferroelectric transition, the order parameter is the polarization, P. In addition to P, the thermodynamic state of bulk ferroelectrics is described by the temperature, T, the electric field, E, the strain η, and the stress, σ, where the electric field and the stress are usually external variables applied to the system. The free energy, F, can be expressed as a function of three components of polarization, six components of the stress tensor, and one of temperature. In the vicinity of the phase transition the free energy is expanded in powers of the dependent variables with coefficients that can be fit to experimental data or calculated. Expanding the free energy in terms of a single component of polarization yields

$$F_P = F - EP = F_0 + \frac{\alpha}{2}P^2 + \frac{\beta}{4}P^4 + \frac{\gamma}{6}P^6 - EP \tag{1.5}$$

where F_0 is the free energy density of the paraelectric phase (when $E = 0$), and the expansion coefficients α, β, and γ are generally temperature and pressure dependent.

The continuum field approach described above can be used to simulate microstructure evolution for a variety of applications including solidification of pure liquids and alloys, other solid state transformations (eg., martensitic transformation), and coarsening and grain growth. No direct assumptions are made regarding the existence and behaviour of domain walls and grian boundaries, which result directly from the minimization of free energy. This is in contrast with conventional microstructure evolution simulations, where the domain walls and grain boundaries are sharp interfaces and the positions and velocities of these interfaces are explicitly tracked [45]. This tracking becomes computationally expensive with complex microstructures in three-dimensions. In phase-field models, the interface is diffuse with properties changing continuously in a narrow region, eliminating the need for interface tracking. This has made phase-field simulations very popular for ferroelectrics [46].

Some model are not overly concerned with the actual domain structure, but instead simply track the volume fraction of domain types within a grain. Hwang et al. were the first to employ this approach for the simple case of a polycrystal comprised of randomly oriented grains with a single domain [47]. They combined electric and mechanical loads and used a work energy criteria to determine when domain switching occured and to what extent. Simply, a domain of variant a was switched to variant b when the work per unit volume done by local electrical and mechanical fields in the switching process exceeded a critical value. In the model, Hwang et al. used the Reuss approximation which assumes that the stress and electric fields are uniform. Averaging over many grains they were able to obtain the characteristic strain butterfly and polarization hysteresis loops such as those shown in Figure 1.9.

Since this first approach, many modifications have been made to build upon this model using approaches first introduced in crystal plasticity modeling. For example, the interaction between grains results in the non-uniformity of the stress, strain, and electric field state within the grains, which can be introduced via the Eshelby stress tensor [48] and its piezoelectric equivalent derived by Dunn and Taya [49]. Partial switching of domains is modeled as an incremental process in order to maintain stability, since the sudden change in strain and polarization can actually cause a domain to switch back. This incremental switching treats the effects of domain wall motion on remanent polarization and strain is analogous to the operation of a slip system in plasticity. The active variant and rate of transformation depends on the applied loads and the present state of the material. The crystal plasticity-based model for ferroelectrics was first implemented by Huber et al. [50] using a self-consistent (SC) scheme. In self-consistent modeling, the grain is treated as an inclusion in a homogeneous medium whose properties are continuously updated as the state variables are refined. In this case, the state variables are the volume fractions of the domain variants. In contrast, finite element (FE) simulations treat the polycrystal as an aggregate, thus grain to grain interaction is preserved. Although both SC and FE models are successful at predicting macroscopic hysteresis and butterfly loops, SC models underpredict local stress concentrations, which result from, for example, forced compatibility at grain boundaries [51]. Such considerations become important when trying to predict domain switching in a reliable way. The results to be presented in Chapter 3 are especially well-suited for input and validation of SC and FE models, and similar approaches have been used to

study deformation twinning in magnesium [52] and zirconium alloys [53, 54].

1.4 Lead-free alternative piezoceramics

In recent years it has become important to consider not just the functionality but also the environmental impact of sourcing, manufacturing, and disposal of raw materials and end products. In the early to mid 2000s, the European Union adopted the Restriction of Hazardous Substances Directive(RoHS), restricting the use of ten substances including lead, mercury, and cadmium. Exceptions are made where functionality can not be matched by a lead-free materials, nonetheless, there exists legislative pressure for the development of alternatives. Although lead-free piezoceramics were amongst the first to be discovered (eg., BT), their development was largely halted after the discovery of PZT due to its larger coupling coefficient and improved temperature stability. Lead-free piezoceramics can be categorized in two groups; those that aim to compete with and replace PZT and those with properties with which PZT cannot compete. The first group is dominated by ceramics based on $(K, Na)NbO_3$ (KNN), $(Bi_{0.5}Na_{0.5})TiO_3 - BaTiO_3$ (BNT-BT), and (Ba,Ca)(Zr,Ti)O_3 (BCZT). The second group includes, for example, SiO_2, AlN, $LiNbO_3$ (single crystals), and Bi-based layered structures. These ceramics are inferior to PZT in some respects but excel in others, for example, high temperature application. The first group is of the most relevance to this work.

The KNN system was developed by Saito et al. [55], who were able to achieve a piezoelectric constant, d_{33}, of 416 picocoulombs per newton (pCN^{-1}) at a composition near the morphotropic phase boundary between orthorhombic and tetragonal with a processing route that results in highly $\langle 001 \rangle$ textured polycrystals. This is comparable to that of some actuator-grade PZT piezoceramics and appeared to stimulate the community, with a large jump in the number of publications related to lead-free materials in the following ten years. Still, Rödel et al. [56] note that the academic strides have not been matched by industrial applications. While in some cases, lead-free alternatives may offer better properties than their PZT counterparts, there are still concerns regarding reliability, and the majority of materials are 5 or more years away from replacement.

The search for lead-free piezoceramics is just an example of the challenges facing all industries and applications. It is increasingly true that a dearth of suitable materials is the limiting factor in the development of new products. It is estimated that the time from laboratory development to market for new materials is approximately 20 years, much too long for the challenges we face in energy, environment, health and wellness, and economy. It is for this reason that new approaches such as the Materials Genome Initiative [57] in the United States and those addressed by the recent International Assessment of Research and Development in Simulation-Based Engineering and Science [58] are being proposed. Improvements in processing power have reached a point where it is now feasible to use large-scale simulations as an integral part of the ma-

terials design process. Materials compositions, structures, and processing techniques could be screened for desired properties and performance before extensive testing and experiments are performed. Such a scheme would decrease both the time and resources used for performing trial and error experimental cycles, with the Materials Genome Initiative aiming for a reduction of time to market of 50%.

At the heart of such approaches is open collaboration on an inter-institutional and inter-disciplinary scale. Scientists must have ready access to each other's algorithms and experimental data, for development and validation, in formats that are user-friendly and standardized. Various measurements (ie., heat transfer coefficients, elastic moduli, etc.) must be integrated to give a comprehensive overview of the material response to a variety of stimuli. It has also become increasingly clear that macroscopic behaviour is the result of coupling across all length scales in three dimensions, with interactions between defects, domains, grains, etc. Modelling across length scales has recently been emphasized as a topic of interest by The Minerals Metals & Materials Society [59]

In-situ X-ray and neutron diffraction techniques are uniquely well-suited to study the fundamental phenomena that can be used to build up these models, as well as to provide spatially-resolved data sets for model validation. This approach has already been used on a smaller scale to study, for example, recrystallization [60], stress at a crack tip [61], and deformation twinning in hexagonal-close-packed metals [52, 53, 54] in three dimensions. In this study we use such techniques and develop new analysis methods to study the evolution of domain volume fractions at the grain scale, in the context of their three-dimensional environment.

Chapter 2

Structural characterization by high-energy X-ray diffraction

Materials properties are intimately linked with their structure, as demonstrated in Chapter 1. Only the 20 non-centrosymmetric crystals exhibit the piezoelectric effect since they must form an anisotropic polar axis and of these, only 10 classes are pyroelectric and fewer still, ferroelectric. Most engineering materials are polycrystals, so in addition to the crystal structure of the individual crystallites there exists a microstructure that describes how the crystallites are arranged relative to each other. The collective response of the crystallites to some externally imposed state is what determines that macroscopic behaviour. The aim of materials scientists is then to develop processing techniques that arrange these crystallites in a way that results in a macroscopic response within the design criteria of some component.

Understanding this interrelationship between structure, properties, performance and processing is the paradigm of materials science, and at the centre is characterization. Without materials characterization no understanding of engineering materials could be ascertained. Early crystallography was the realm of mineralogists studying natural rocks and minerals, who first used crystal habit planes and the polarized light microscopy to identify the 32 crystal classes we know of today. Although these techniques are still used, and useful, today, the field of crystallography grew monumentally with the discovery of X-ray diffraction, whose reach is not limited to the fields of mineralogy and metallurgy, but all of science.

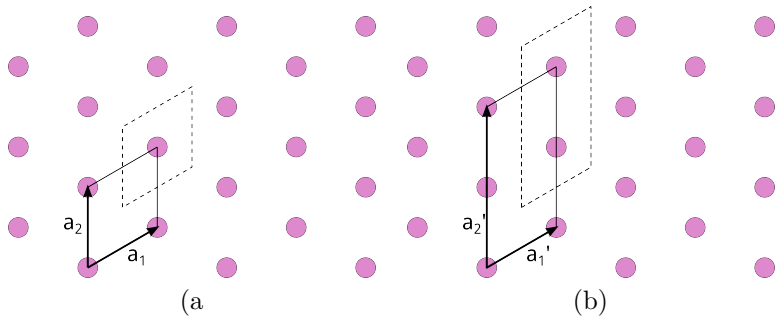

Figure 2.1: The selection of (a) a primitive cell (b) a non-primitive cell in a two-dimensional lattice.

2.1 The crystal lattice

The atoms of a crystalline material are arranged in building blocks called unit cells, and the regular repeating of unit cells creates a lattice, as shown for two dimensions in Figure 2.1. The lattice can be specified by a set of vectors $\mathbf{R_n}$ such that

$$\mathbf{R_n} = n_1\mathbf{a}_1 + n_2\mathbf{a}_2 \tag{2.1}$$

where $\mathbf{a}_1$ and $\mathbf{a}_2$ are the lattice vectors, which define the unit cell, and n_1 and n_2 are integers. The selection of a unit cell is arbitrary but the unit cell resulting in the smallest volume, called the primitive cell, is commonly chosen as in Figure 2.1(a). The non-primitive unit cell in Figure 2.1(b), however, is equally valid. Sometimes a non-primitive cell is chosen to highlight the symmetry of a particular crystal. One unit cell's worth of atoms is called the basis, consisting of one atom for the primitive cell in Figure 2.1(a) and two atoms for the non-primitive cell in (b). Translation along any of the lattice vectors yields an identical unit cell. When extended to three dimensions, the lattice is given by

$$\mathbf{R_n} = n_1\mathbf{a}_1 + n_2\mathbf{a}_2 + n_3\mathbf{a}_3 \tag{2.2}$$

A crystal is then a result of the convolution ($\star$) of a lattice with a basis as shown in Figure 2.2.

It is common to refer to atoms as lying on planes which are specified by *Miller indices*. The Miller indices (h, k, l) specify a plane closest to the origin with intercepts (a_1/h, a_2/k, a_3/l). As a two-dimensional example, the (10) and (21) planes are shown for a lattice in Figure 2.3. The spacing in between successive planes of a given (hkl) family is referred to simply as the d-spacing.

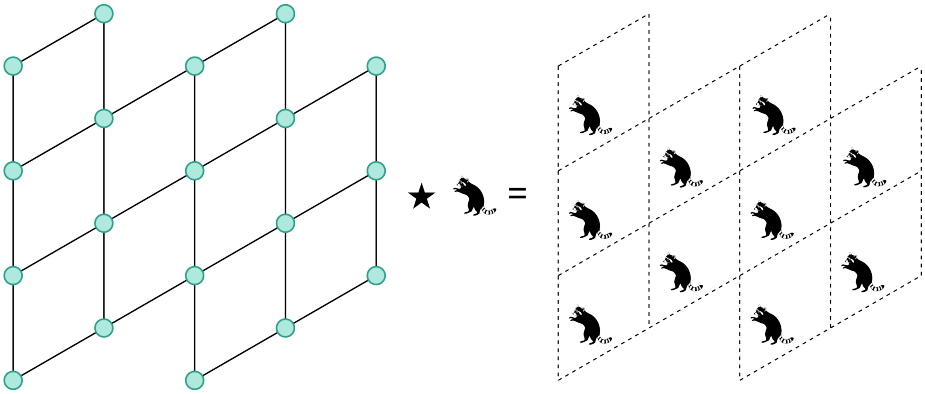

Figure 2.2: Convolution of lattice with basis to form crystal (adapted from Elements of Modern X-ray Physics, Raccoon by Christy Presler from the Noun Project)

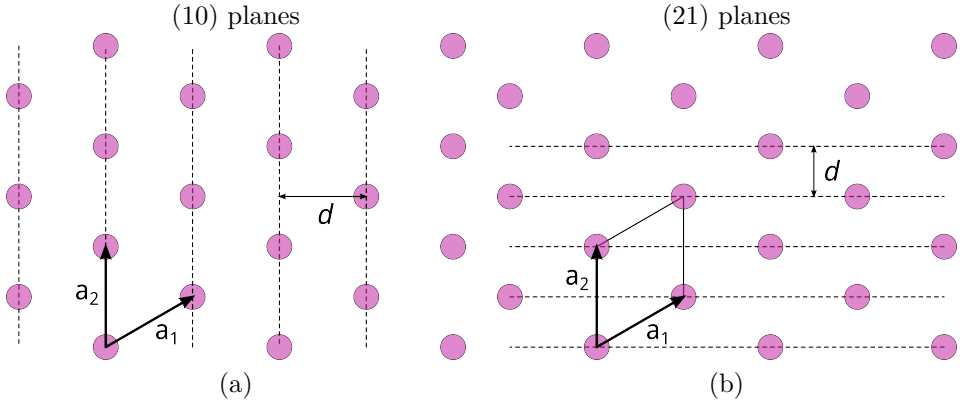

Figure 2.3: (a) (10) planes (b) (21) planes

2.2 X-ray diffraction by crystalline materials

The fundamental interaction occurring in X-ray diffraction is between incoming photons and the electron shell of the atoms upon which they impinge. The elastic scattering of X-rays by a free electron is referred to as the *Thomson scattering length*, which can be thought of as the classical radius of an electron, given by

$$r_0 = \left(\frac{e^2}{4\pi\epsilon_0 mc^2}\right) = 2.82 \times 10^{-5}\text{Å} \tag{2.3}$$

where e and m are the electric charge and mass of the electron, c is the speed of light, and ϵ_0 is the permittivity of free space. Continuing with the classical description, the electron distribution surrounding an atom is described by a number density, $\rho(\mathbf{r})$. The scattering from an atom is the superposition of the contributions from all of the electron cloud. Taking into account the phase shift from scattering at different positions in the volume and integrating the contributions of all volume elements yields

$$-r_0 f^0(\mathbf{Q}) = -r_0 \int \rho(\mathbf{r}) \mathrm{e}^{i\mathbf{Q}\cdot\mathbf{r}} d\mathbf{r} \tag{2.4}$$

where $f^0(\mathbf{Q})$ is the *atomic form factor*. Scattering from a molecule is then a sum over the atoms of that molecule

$$F^{\text{mol}}(\mathbf{Q}) = \sum_j f_j(\mathbf{Q}) \mathrm{e}^{i\mathbf{Q}\cdot\mathbf{r}_j} \tag{2.5}$$

and scattering from a crystal is then calculated by summing over all of the atoms of the unit cell and then all of the unit cells in the lattice.

$$F^{\text{crystal}}(\mathbf{Q}) = \overbrace{\sum_j f_j(\mathbf{Q}) \mathrm{e}^{i\mathbf{Q}\cdot\mathbf{r}_j}}^{\text{Unit cell structure factor}} \overbrace{\sum_{\mathrm{n}} \mathrm{e}^{i\mathbf{Q}\cdot\mathbf{R_n}}}^{\text{Lattice sum}} \tag{2.6}$$

The sum over the basis of atoms in the unit cell is called the unit cell structure factor.

The diffracting condition for a set of lattice planes can be derived by considering a plane wave impinging on atoms arranged in a square lattice as shown in Figure 2.4, each row spaced by d. The directions of the incident wave vector is $\mathbf{K}'$ and that of the scattered wave vector is $\mathbf{K}$. The path traveled by the incident wave to an atom in the bottom row of atoms is longer than that traveled to the top row by $\mathbf{K}' \cdot \mathbf{d}$, shown in heavy-line, and the phase of the wave impinging on the bottom row advances relative to the wave impinging on the top row. The path traveled by a wave scattered by an atom in the bottom row is also longer than that scattered by an atom in the top row by $\mathbf{K} \cdot \mathbf{d}$, and the phase lags. The total difference in path length is given by $(\mathbf{K} - \mathbf{K}') \cdot \mathbf{d}$ where $\mathbf{Q} = \mathbf{K} - \mathbf{K}'$ is referred to as the scattering vector. When the scattering is elastic, $|\mathbf{K}'| = |\mathbf{K}|$ and $|\mathbf{Q}| = 2d \sin\theta$. For constructive interference, the difference in path length must be an integer multiple of the wavelength, λ, yielding the diffraction condition

$$n\lambda = 2d \sin\theta \tag{2.7}$$

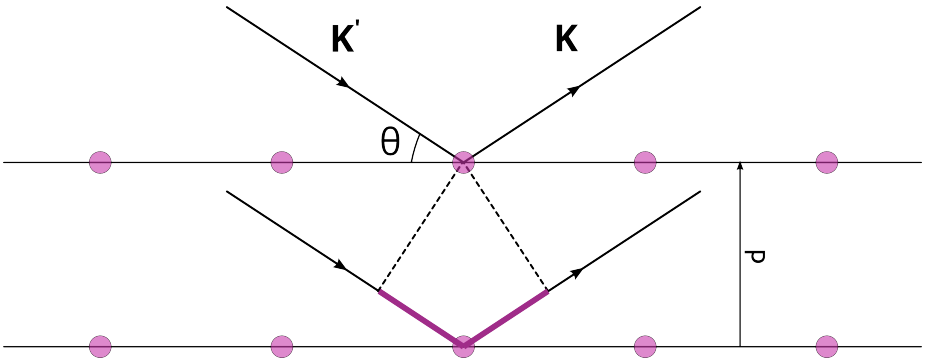

Figure 2.4: The diffraction condition for lattice planes with a spacing d.

where n is a positive integer, commonly known as Bragg's law. The lattice described above exists in real space. However, it is often convenient to use the concept of a *reciprocal lattice* when considering diffraction. Vectors and properties of the reciprocal lattice are commonly denoted using * notation. The reciprocal lattice spacing, d^* of a given family of planes is simply $1/d$, the inverse of the direct lattice spacing. In the three-dimensional case, the reciprocal lattice basis vectors are

$$\mathbf{a}_1^* = \frac{2\pi}{v_c}\mathbf{a}_2 \times \mathbf{a}_3 \qquad \mathbf{a}_2^* = \frac{2\pi}{v_c}\mathbf{a}_3 \times \mathbf{a}_1 \qquad \mathbf{a}_3^* = \frac{2\pi}{v_c}\mathbf{a}_1 \times \mathbf{a}_2 \tag{2.8}$$

where $v_c = \mathbf{a}_1 \cdot (\mathbf{a}_2 \times \mathbf{a}_2)$ is the volume of the unit cell.

In reciprocal space, the diffraction condition is given by three Laue equations:

$$\begin{aligned} \mathbf{Q} \cdot \mathbf{a}_1^* &= h\lambda \\ \mathbf{Q} \cdot \mathbf{a}_2^* &= k\lambda \\ \mathbf{Q} \cdot \mathbf{a}_3^* &= l\lambda \end{aligned} \tag{2.9}$$

where $\mathbf{a}$, $\mathbf{b}$, and $\mathbf{c}$ are the basis vectors of a three-dimensional lattice and (h, k, l) are integers. When these conditions are satisfied simultaneously, the incoming wave is diffracted on the lattice planes of Miller indices (h, k, l).

2.2.1 Diffraction by a rotated crystal

The diffraction conditions above are for an unrotated crystal, but one can also consider an arbitrarily oriented crystal, for example, in a polycrystalline sample. Consider two coordinate systems: laboratory, l and sample, s. The laboratory system is fixed with x_l along the beam direction, z_l vertical positive upwards, and y_l normal. The sample coordinate system is fixed with z_s along the z_l rotation axis, and x_s and y_s

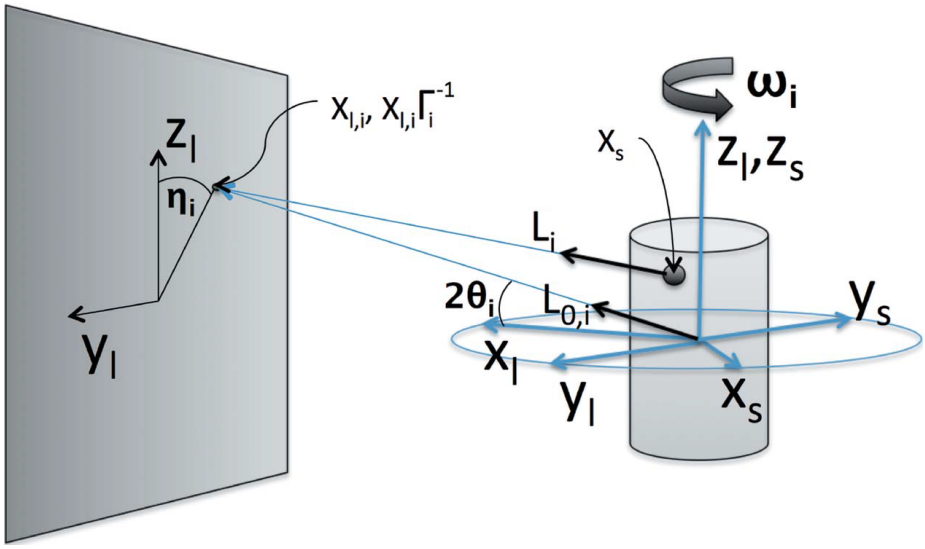

Figure 2.5: Definition of geometry used to derive the diffraction condition for a rotated crystal in a polycrystalline sample. The laboratory and and sample coordinate systems are denoted by (x_l, y_l, z_l) and (x_z, y_s, z_s), respectively. The two coordinate systems are related through a rotation about the z_l.

aligned with x_l and y_l at rotation $\omega = 0$. The origin of of the sample system is at the transmitted beam centre. The sample coordinate system is then related to the laboratory coordinate system by a rotation around z_l. In polycrystalline diffraction, the crystal and sample are also separate objects and an additional coordinate system is needed, the Cartesian grain coordinate system, c. For the case of the tetragonal system, x_c, y_c and z_c are fixed along the crystal lattice a, b, and c directions, respectively. The crystal coordinate system is then related to the sample coordinate system by the orientation matrix, U.

The scattering vector in the laboratory coordinate system, $\mathbf{G}_i$, is given by

$$\mathbf{G}_i = \frac{d_i}{2\pi}\Omega_i U B \mathbf{G}_{hkl,i} \tag{2.10}$$

where $\mathbf{G}_i$ of magnitude 1, d_i is the lattice spacing for the ith reflection, Ω_i is a right-hand rotation, ω_i, around the z axis:

$$\Omega_i = \begin{pmatrix} \cos\omega_i & -\sin\omega_i & 0 \\ \sin\omega_i & \cos\omega_i & 0 \\ 0 & 0 & 1 \end{pmatrix} \tag{2.11}$$

B is the correspondence between the Cartesian hkl lattice

$$\mathbf{G}_{hkl} = \begin{pmatrix} h \\ k \\ l \end{pmatrix} \tag{2.12}$$

and reciprocal space,

$$B = \begin{pmatrix} a^* & b^*\cos\gamma^* & c^*\cos\beta^* \\ 0 & b^*\sin\gamma^* & -c^*\sin\beta^*\cos\alpha \\ 0 & 0 & c^*\sin\beta^*\sin\alpha^* \end{pmatrix} \tag{2.13}$$

where

$$\cos\alpha = \frac{\cos\beta^*\cos\gamma^* - \cos\alpha^*}{\sin\beta^*\sin\gamma^*} \tag{2.14}$$

Since a piezoceramic is a polycrystalline material, we will use this formulation to index and refine the grain and domain-scale parameters of bulk grains in the polycrystal as it is rotated, bringing different grains into the diffracting conditions.

2.3 X-ray sources

There are three main sources of X-rays: (i) the standard X-ray tube, (ii) the rotation anode, and (iii) synchrotron radiation. The standard tube was developed by W.D. Coolidge in 1912 and was developed as an improvement to the Crookes tube on which Rontgen originally discovered X-rays. In a Crookes tube, a DC voltage was applied between two platinum anodes and the aluminum cathode, creating and accelerating a small number of ions from the gas in the partially evacuated tube. These ions struck other gas atoms creating more ions in a chain reaction. The positive ions were then attracted to the anode, creating X-rays as they struck the platinum atoms. Crookes tubes were very unreliable, leading William Coolidge to improve on them in 1913 with the Coolidge tube. In a Coolidge tube, electrons are produced from a tungsten filament by thermal electron emission then accelerated by a high voltage potential toward the anode, which was cooled by flowing water. The maximum power of the Coolidge tube was approximately 1 kW, limited by the cooling efficiency of the device. This was the standard X-ray tube until the 1960s when a reliable rotating anode generators were developed. A rotating anode allows for heat dissipation over a much larger volume and thus, an increase in power. Rotating anode type sources are now the most commonly used.

The intensity spectrum of X-rays generated by a rotating anode is has two components: continuous bremsstrahlung radiation from electrons that are decelerated and stopped in the metal, and fluorescent radiation peaks. X-ray fluorescence results when an electron is knocked out of the inner shell of an atom. An electron from one of the outer shells relaxes to take its place and an X-ray is emitted with energy of the difference between the outer and inner shell. Many advanced characterization techniques require an X-ray beam of higher energy and flux than can be provided by typical laboratory sources, especially once monochromated. These techniques have taken advantage of synchrotron radiation from particle accelerators called synchrotron light sources, in which electromagnetic radiation is emitted by charged particles moving at relativistic speeds in a circular orbit. Such particles are are always accelerating, thus, radiation is emitted tangential to the orbit in a narrow cone with an opening angle $1/\gamma$, where $\gamma = \epsilon_e/mc^2$, typically around 0.1 milli-radian.

2.3.1 High energy X-rays for materials science

The basic operation of a synchrotron is shown schematically in Figure 2.6. The electrons are first emitted from a heated filament in a so-called electron gun and then accelerated in a linear accelerator (LINAC). They enter a booster synchrotron for further acceleration before entering the storage ring. In the storage ring the electrons are kept in orbit by large bending magnets (BM) at arced sections of the track, typically with magnetic field strengths of around 1 Tesla. The radiation from a bending magnet is emitted in a flattened cone with a fan angle equal to the angular change of the electrons. One or more beamlines can be positioned to make use of radiation directly

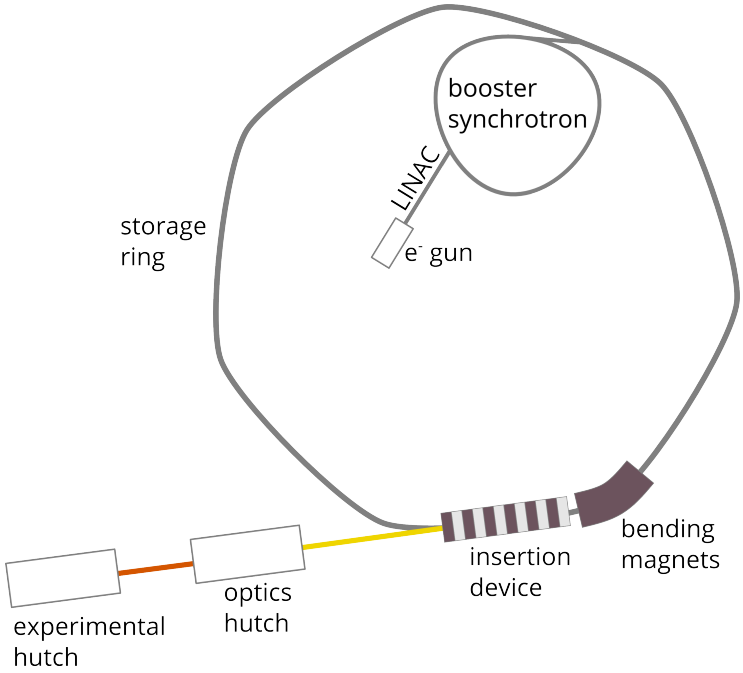

Figure 2.6: Schematic of a third generation synchrotron. Electrons are emitted from a heated filament and accelerated in a linear accelerator (LINAC). The electrons are further accelerated in a booster synchrotron before entering the storage ring where they are kept in a racetrack-like orbit by bending magnets placed at curved sections. Beamlines extend from the axis of emission, using radiation emitted at bending magnets or insertion devices placed in the straight sections. The polychromatic beam enters an optics hutch housing the monochromators and lenses for energy selection and focussing. The tuned beam then enters the experimental hutch where the profile can be further defined, with e.g., slits, before reaching the sample.

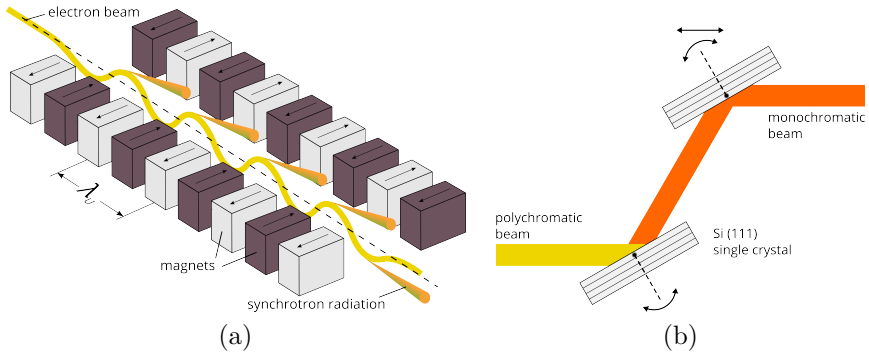

Figure 2.7: Key components affecting the flux and energy of the beam (a) monochromator and (b) undulator

from a BM.

Since the radiation from a BM is spread over a wide angle the flux may be too low for some experiments. For example, in studies of embedded grains such as the one presented here the data collection time is significantly reduced by a higher fluc. Studies of dynamic processes such as grain growth also require sufficient diffracted intensity counts in a shorter amount of time. Third generation synchrotrons achieve a much higher flux using insertion devices (ID) that are placed in the straight sections of the storage ring from which ID beamlines extend. At ID11, the materials science beamline of the ESRF, the insertion device is an undulator, shown schematically in Figure 2.7(a). The undulator consists of a series of magnets that produce alternating up and down magnetic fields, forcing the electrons into an undulating, sinusoidal trajectory in the plane of the storage ring. The radiation emitted at each bend in the oscillation overlaps and, given the correct frequency, constructively interferes, producing a narrow beam of high flux. The radiation cone is compressed by a factor of approximately $1/\sqrt{N}$ relative to the natural synchrotron opening angle of $1/\gamma$, where N is the number of periods, typically around 50. The gap between the two sets of magnets can also be adjusted to fine-tube the beam. From the ID, the beam enters the optics hutch of the beamline, where the monochromators and lenses are housed.

Elastic strains are of great interest at the materials science beamline and they are given by a change in d-spacing of lattice planes. From Bragg's law, the diffraction condition for a set of lattice planes with a given d-spacing depends on the wavelength of the incoming beam, thus the change in lattice spacing can be measured by a change in the position of the measured diffracted intensity. To precisely measure the position of diffraction peaks we require a monochromatic beam with a narrow bandwidth. At ID11, the monochromator consists of two Si (111) single crystals, shown schematically in Figure 2.7(b), which can tune the energy in a range of 18-140 keV by diffracting only certain wavelength, based on Bragg's law. Energy is then selected by rotating the crystals and changing the diffracting condition. The first crystal selects the energy and

takes most of the heat load, thus it must be significantly cooled. The second crystal redirects the beam in the direction of the original incoming beam. Additionally, the crystals can be slightly bent for focusing, which allows for the selection of a very narrow bandwidth while maintaining higher flux [62]. The beam can then be focused by a series of lenses, if necessary, before entering the experimental hutch, which houses additional components for beam monitoring and definition, the sample and sample environment, and the detectors. The beam can be defined to the profile required with slits, usually done as near to the sample as possible to minimize beam scattering in air.

2.4 Three-dimensional X-ray diffraction

For the experiments to be presented in this thesis, the diffracted signal is measured on a two-dimensional detector. When a polycrystal is illuminated, the diffraction condition may be satisfied for multiple crystals simultaneously. In the case of a powder-like sample where many orientations are present simultaneously, the diffraction occurs in cones for each (hkl) plane and is measured on the two-dimensional detector as rings, for example as in Figure 2.8. This is a common method for determining the average lattice parameters and strains of a sample. In a coarse-grained polycrystal, many fewer crystallites fulfill the Bragg condition simultaneously, and the diffraction is measured as spots along the Debye-Scherrer rings, as in Figure 2.8(b).

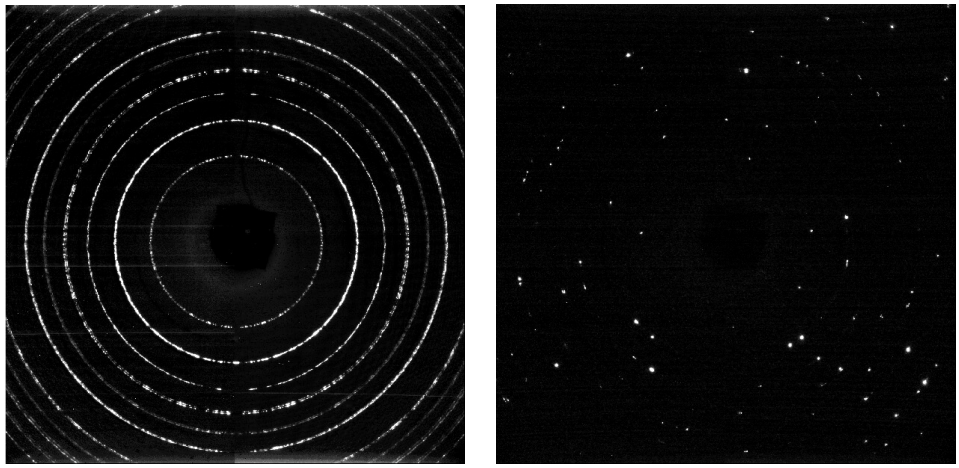

a) powder diffraction (b) polycrystal diffraction

Figure 2.8: Typical diffraction images obtained from (a) powder-like samples and (b) polycrystalline samples of much fewer crystallites. The pattern in (a) was generated by summing images from a nearly 360° scan of (b), capturing the diffracted intensity from all crystallites simultaneously.

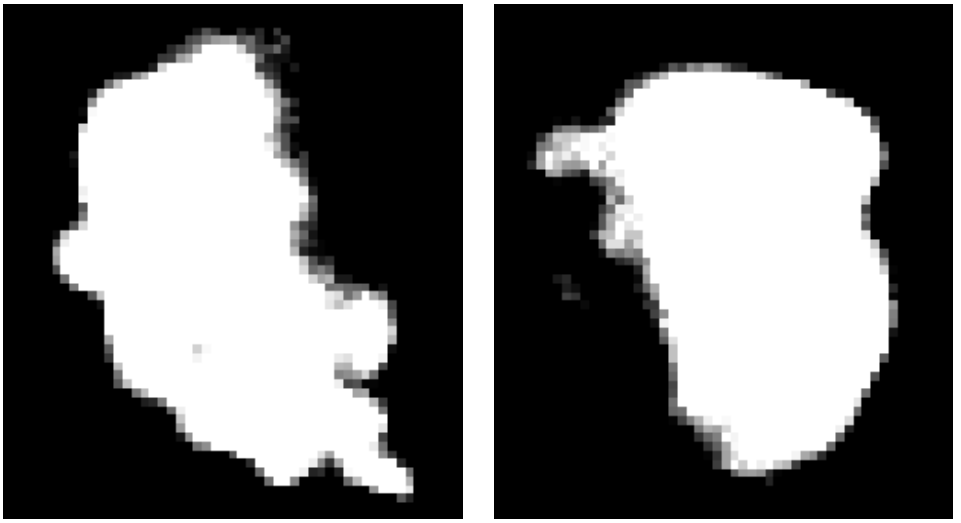

Figure 2.9: Diffraction spots obtained from nearfield mapping with the detector very close to the sample.

The farfield three-dimensional X-ray diffraction (3DXRD) technique makes use of diffraction patterns like that in Figure 2.8(b) and the equations 2.10-2.14. By rotating the polycrystalline sample different grains are brought into the diffracting condition and all orientations are probed. The diffraction spots are then identified by their position on the detector $(\mathrm{det}_y, \mathrm{det}_z)$ and the angle, ω, at which they were recorded. The indexing algorithm GrainSpotter [63] then searches through orientation space to associate the measured diffraction spots with grains within the sample and refines their centre-of-mass position and orientation. Further refinement can additionally yield the relative grain volumes and lattice strains.

A related technique is nearfied 3DXRD, where the detector is placed very close to the sample, yielding diffraction spots that still appear on the Debye-Scherrer rings, but more broad as in Figure 2.9. These spots carry information about the morphology of the grains, and this technique provides the spatial resolution to reconstruct the three-dimensional sample microstructure. A combination of farfield and nearfield 3DXRD can then yield a three-dimensional view of structural changes occurring in the bulk of a polycrystalline sample. The work presented in the rest of this thesis will demonstrate how such a data set can be created and analysed.

Chapter 3

Evolution of non-180° domain volume fractions on the grain scale

Powder diffraction studies have clearly demonstrated that domain switching strongly depends on the orientation of the crystal relative to the direction of the external applied electric field. Generally, the polar axis switches to the direction most closely aligned with the field direction, as far as allowed by crystal symmetry. This can be observed on a two-dimensional diffraction pattern by the changes in the intensity ratios of rings split in 2θ, for example the (200)/(002) ring for tetragonal symmetry and the (111) rings for rhombohedral symmetry, at various azimuthal angles, which represent the crystallite c-axis misorientation from the electric field direction. However, in a powder-like sample, the response is averaged over for all crystallites, making the effects of local heterogeneity such as the grain neighbourhood and strain gradients unobservable. Thus, in order to study the response of individual grains of a ceramic in the context of their neighbourhood environment, the experimental technique must be a bulk, three-dimensional measurement with the direct space resolution to identify individual grains, their positions, neighbourhoods, shapes and orientation, as well as the reciprocal space resolution to capture the peak splitting that results from the domain structure. The followings present a combination of nearfield (NF) and farfield (FF) 3DXRD, whereby the nearfield setup is used to create a three-dimensional space-filling map of grains and their orientations, and the farfield setup is used to measure the grain-scale domain volume fraction evolution of three domain types.

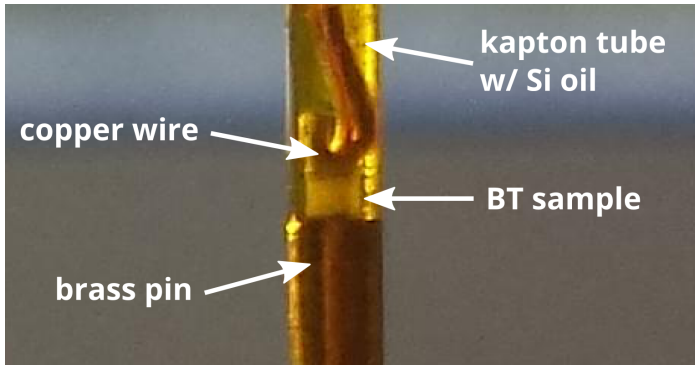

Figure 3.1: The BT sample prepared for 3DXRD. Gold was sputtered on the top and bottom of the sample and it was mounted on a brass pin with the top surface connected to a copper wire. Silver paint was used to ensure a good connection on both surfaces. The mount was immersed in a kapton tube filled with Si oil, which helps prevent dielectric breakdown of the sample surface when a large electric field is applied.

3.1 Mapping the grain structure

A barium titanate ceramic was prepared with a grain size of approximately 50-70 μm and cut and polished into a cuboid sample of dimensions $300\times300\times400$ μm^3. Following the setup described in Daniels et al. [35], gold was sputtered on opposite faces of the sample for the purpose of electrical connection, and the sample was mounted on a brass pin as shown in Figure 3.1. The sample was immersed in a kapton tube containing silicon oil and a copper wire was attached to the top of the sample. Silver paint was used to ensure a good electrical connection between the sample and the wire and the sample and the pin. The Si oil was used to help prevent dielectric breakdown of the sample surface under a high externally applied electric field.

The general setup of all experiments performed is shown in Figure 3.2. Near-field mapping employs the two detectors at L_1 and L_2 simultaneously. When the detector is very close to the sample the diffraction spots are broad and can be used to reconstruct the three-dimensional microstructure, while the intermediate detector is used to collect data for indexing. The L_1 detector was the the first screen of the Risø3D detector [64], with 2048×2048 pixels of size 1.4×1.4 μm^2, placed 8 mm away from the sample and the L_2 detector was a Frelon4M detector [65] with 2048×2048 pixels of size 50×50 μm^2. To minimize spatial distortion that originates from absorption through the detector thickness the detector screen is made very thin. This means that the beam energy must be low, chosen here to be 37.010 keV. This is just below the Ba K-edge of 37.450 keV to avoid absorption through the sample. The beam profile was focussed and cut to a box beam geometry of width 500 μm and height 100 μm with lenses and slits. Three layers of the sample were mapped through 360° in steps of 0.1° for layer 0 and

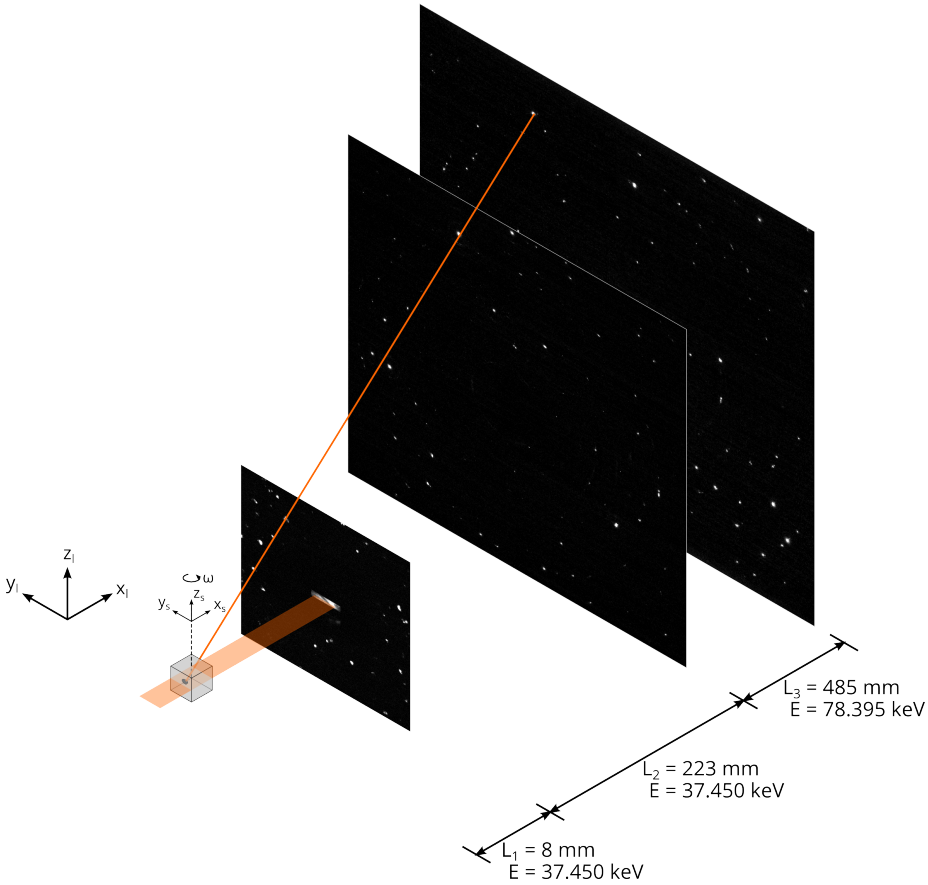

Figure 3.2: Experimental setup showing all three detectors. Near-field data was collected simultaneously on detectors 1 and 2, and farfield data was collected on detector 3 with beam energy, E, as indicated. The laboratory coordinate system is fixed with x_l along the beam direction, z_l positive upwards, and y_l normal. The sample is rotated about the axis z_s. The sample coordinate system is fixed such that the origin in y and z is at the beam center and the origin in x is at axis of rotation.

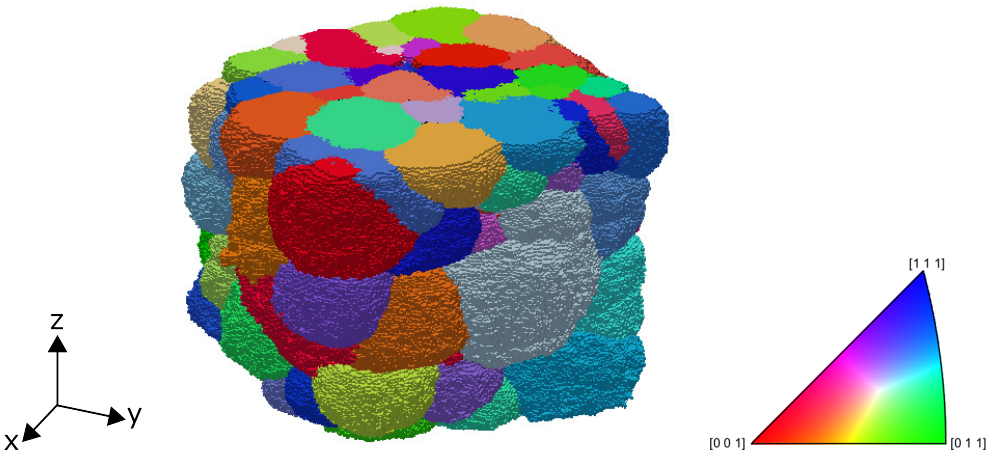

Figure 3.3: Grain map of reconstructed volume coloured by orientation according to the inverse pole figure.

0.2° for layers 1 and 2 due to time constraints. With an exposure time of 5 seconds per image, the mapping of a single layer took approximately 5 hours for layer 0, and 2.5 hours each for layers 1 and 2.

The collected diffraction image stacks were analysed using the Fable software suite (2014), described in detail in [66]. The peak identification on the diffraction images from detector L_2 was performed with a low threshold, chosen so that the split peaks were grown together and the centre-of-mass of the total diffracted intensity originating from the grain was identified. The resulting patterns were indexed using GrainSpotter [63], which searches through orientation space to assign the diffraction spots to individual grains. GrainSpotter subsequently refined the grain orientation and position, outputting a list of grains, their orientation and 3D position, and the list of diffraction spots assigned to each grain. Since the peaks were grown together, the orientation information obtained from GrainSpotter is a nominal orientation for the entire grain, and not a single domain. These indexed grain orientations were then used as seeds to reconstruct a grain map from the L_1 detector data, which again captures spatially-resolved information about the grain morphology.

The algorithm used for reconstruction was a 3D generalization of the GrainSweeper [67] algorithm. Briefly, for each $2\times2\times2$ μm^3 voxel in the $0.5\times0.5\times0.2$ mm^3 reconstruction, centred around the $0.3 \times 0.3 \times 0.1$ mm^3 illuminated layer, the grain seed orientation with the highest completeness ratio of expected to observed number of reflections was assigned. The three adjacent, partly overlapping 200 μm reconstructed layers with a 100 μm inter-layer spacing were then stacked along the z-axis – the common poling and rotation axis – in order to obtain the 3D orientation map. For each voxel in the overlapping regions, the orientation with highest completeness was assigned, and voxels with completeness less than 60% were eliminated from the map. Individual

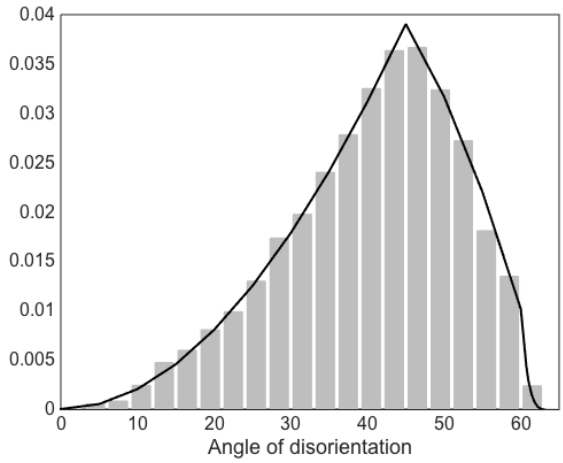

Figure 3.4: Mackenzie plot of the distribution of pairwise misorientations between all grains of the mapped BT sample. The line shows the expected distribution for a randomly-oriented sample. [68]

grains within the orientation map are then identified by assigning adjacent pixels with pseudocubic misorientations less than 1° to the same grain, thereby revealing the morphology and microstructure.

The analysis of data from the L_1 and L_2 detectors yielded a 3D space-filling map consisting of 165 grains, shown in Figure 3.3 coloured by orientation as indicated by the inverse pole figure. The pairwise misorientation between all grains was calculated and plotted as a relative frequency in a Mackenzie-type analysis, as shown in Figure 3.4. The distribution is that of a randomly textured polycrystal, shown as a solid line, which is expected for the ceramic processing route used to manufacture the sample.

3.2 Mapping the grain-scale non-180° switching strain

The true aim of this study is to examine the effect of the 3D microstructure on the grain-scale response of polycrystal, for example, neighbourhood orientations favourable or unfavourable for domain switching. Data for this purpose was collected on the L_3 far-field detector, which is the same as the intermediate L_2 detector, but this time placed 485 mm away from the sample. For this part of the experiment only one detector was used and the energy was tuned to 78.395 keV and the beam size to 100 μm high and 500 μm wide, illuminating the entire width of the sample. Diffraction

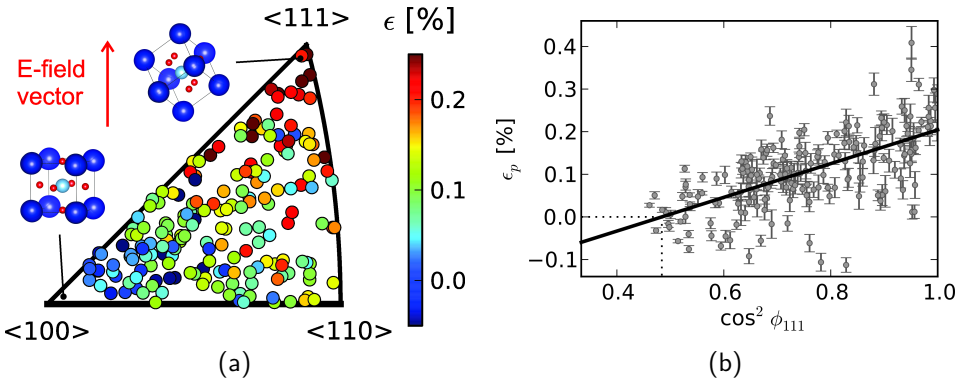

Figure 3.5: Results obtained for the experiment on BNKT: (a) an inverse pole figure of indexed BNKT grain orientations where each marker represents a grain. The marker colour represents calculated non-180° ferroelectric switching strain along the field direction. (b) domain switching strains along the poling direction as a function of $\cos^2 \phi_{111}$, where ϕ_{111} is the misorientation between the electric field vector and the closest <111> direction in the grain.

data was collected in the angular range of 345° about the vertical z-axis in steps of 0.1°. The missing angular range is due to interference of the support used to hold up the poling apparatus, which entailed connecting a power supply to the copper wire on the sample surface. The sample was first mapped in the as processed state (F0), then at an intermediate field strength near the cohesive field (F1), and at high field (F2). The applied voltage was recorded, however, due to an unknown connection problem it is an unreliable measure of the true internal electric field, as the response measured from the sample is much lower than would be expected for the recorded field strength. In addition to the voltage reading, the field steps were chosen by monitoring the diffraction pattern for signs of non-180° domain switching.

Generally, the intensity of diffraction measured from some diffracting structure is proportional to its volume. In these ferroelastic materials, the non-180° domains result in peak splitting, thus, we can use the intensity ratios of these split peaks as a measured of the volume fractions of diffracting structures. We developed this technique to extract grain-scale domain volume fractions and calculate the non-180° switching strain for two piezoceramics: tetragonal BCZT and rhombohedral BNKT ($0.82Bi_{0.5}Na_{0.5}TiO_3$–$18Bi_{0.5}K_0.5TiO_3$) [69] (also found in Included Papers, Paper III). We subsequently used the technique to conduct an in-depth study of BNKT [70](also found in Included Papers, Paper IV), which exhibits an electric-field induced phase transformation from pseudo-cubic in the as-processed state to rhombohedral symmetry. The non-180° switching strains were successfully resolved for 191 grains from the bulk of the sample. The results indicate that $< 111 >$-oriented grains are favourable for a larger response as shown in Figure 3.5(a), where the inverse pole figure is coloured by the magnitude

of the response. However, there exist large deviations from the expected linear trend, as shown in Figure 3.5(b). The data in the BNKT experiment described above were collected in the farfield setup, which does not give spatial resolution. We expand on the work here by examining the grain-scale domain volume fraction evolution of BT in the context of grain neighbourhood and position in the sample by combining this information with the space-filling map described previously.

The (200)/(002) reflections for each grain in the reconstructed volume were extracted from the farfield data measured on L_3, using the orientation information to identify the peaks belonging to each grain. Each reflection was integrated along the rotation, ω, and the azimuth, η, directions, yielding a radial profile along 2θ, as shown in Figure 3.6. For tetragonal symmetry the (200)/(002) peak carry information about the volume fractions, v_{200}, v_{020}, and v_{002}, of the three unique non-180° domain ferroelastic domain variants, d_{200}, d_{020}, and d_{002}. Although there are six unique polarization domain variants in tetragonal BT, only the three non-180° variants can be distinguished with the present method since 180° domain variants have the same (002) peak positions. Since the d-spacing along the c-axis is larger than along the a-axis, the peaks with scattering vector along c show up at a lower 2θ angle than those with scattering vector along a. For every (200)/(002) set of reflections, then, two a-type domains contribute intensity at $2\theta_{\max}$ and one c-type domain contributes intensity at $2\theta_{\min}$, as shown in Figure 3.6, where q is the scattering vector and the colour above each peak corresponds to the contributing domain-types to the right. The volume fraction v_{002} of domain d_{002} must equal the ratio of $I^{002}(2\theta_{\min})$ to the total intensity $I^{002}_{tot} = I^{002}(2\theta_{\min}) + I^{002}(2\theta_{max})$ for each of the 002 and $00\bar{2}$ reflections. This same concept can be applied to the {111} family of reflections in the case of a rhombohedral ferroelastic, in which there are four unique non-180° domains. Since 3DXRD data is typically collected in an angular range near 360° (as allowed by the experimental setup and mounts), most peaks show up twice (Friedel pairs), yielding 4 observations for each domain volume fraction. The domain volume fractions are determined by least-squares fitting, minimizing the residual χ^2:

$$\chi^2_{\text{tetr}} = \sum_{t=(200,020,002)} \sum_{i=1}^{n(t)} \frac{1}{w_{t,i}} \left[v_t - \frac{I^{t,i}(2\theta_{\min})}{T^{t,i}_{\text{tot}}} \right]^2 \tag{3.1}$$

where i is the number of observations for each reflection type, t. The total volume fraction is constrained to 1 by setting v_{002} to $1 - v_{200} - v_{020}$. The weights $w_{t,i}$ can be set to weigh all observed reflections equally, to compensate for a different number of observations, or to down-weight outlier intensities caused, for example, by overlapping peaks from different grains. The changes observed in the split (200)/(002) diffraction peak intensities upon application of an electric field are demonstrated for a single grain in Figure 3.7 at F0 through F2.

It should be noted that if a portion of the grain falls outside of the illuminated volume the measured peak intensities may no longer be representative of the true domain volume fractions (for example, if the unilluminated part of the grain contains many

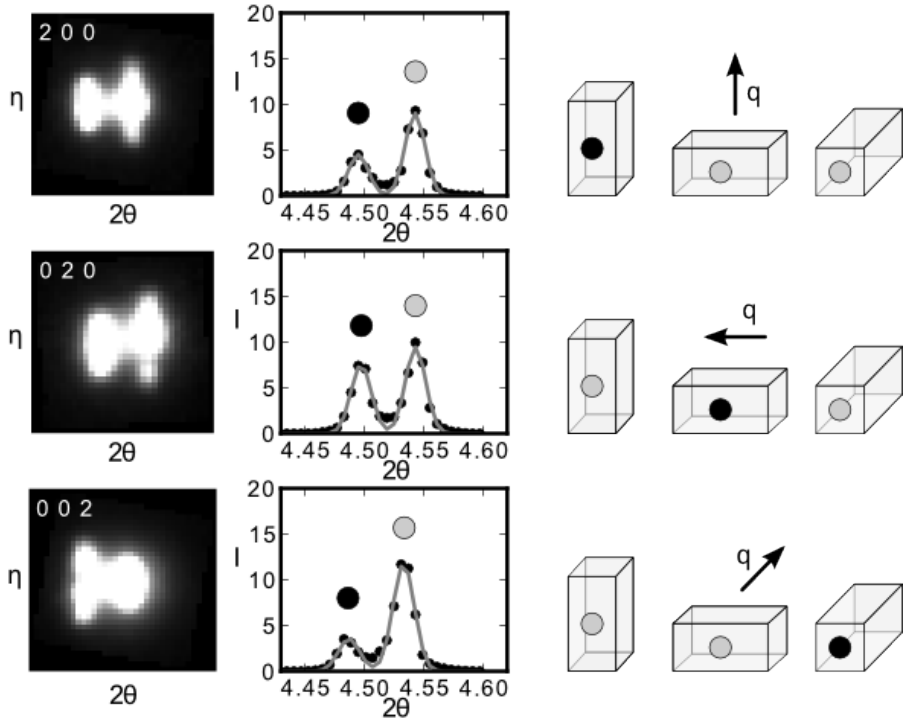

Figure 3.6: Schematic diagram demonstrating the relationship between integrated split 2θ intensity and volume fraction of the three non-180° domain types. The colour label indicates the domain type contribution to the peak intensity, q is the scattering vector. Splitting in 2θ is due to the difference in lattice parameter in the a and c directions.

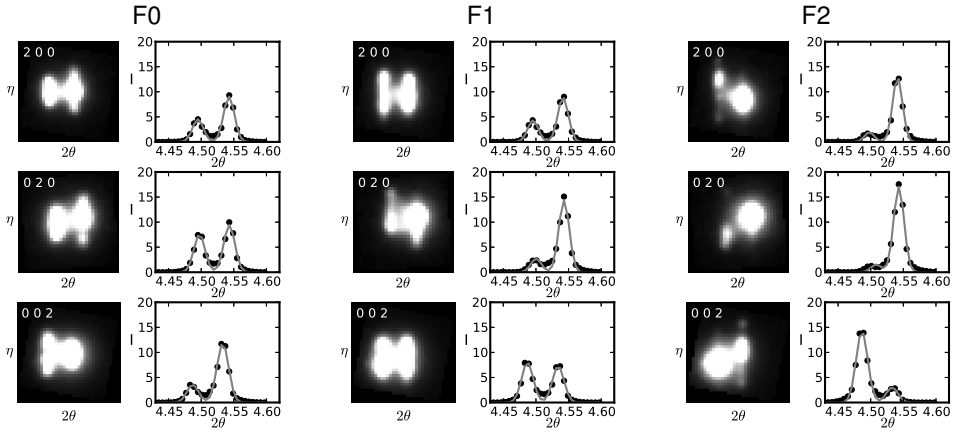

Figure 3.7: (200)/(002) peak intensities for a single grain of BT at F0 through F2. The change in intensity ratio in 2θ represents the change in non-180° domain volume fractions following Figure 3.6.

domains of the d_{002} variant). To check for embedded grains, a partial scan (60° range) was measured with the beam opened to a height of 120 μm centred at the top and bottom layers. The ratio of the peak intensity measured with the small beam to that measured with the larger beam for the reflections found in the angular range of both scans were compared on a grain-by-grain basis. If the median of this intensity ratio for all reflections belonging to a particular grain was found to be less than 0.80, the grain was excluded from further analysis. An example of the intensity ratios of an embedded grain and an excluded grain is shown in Figure 3.8.

In Chapter 1, domain switching was identified as the source of extrinsic strain in piezoceramics and a large contributor to the overall strain response. Assuming the non-180° domain c-axis misorientation to be 90° the domain switching strain is resolved along the poling direction, ϵ_p, was calculated from the extracted domain volume fractions along the unit vector l as

$$\epsilon_p = \frac{(c-a)}{a_0}\left(v_{200}l_1^2 + v_{020}l_2^2 + v_{002}l_3^2\right) - \frac{1}{3} \tag{3.2}$$

where c and a are the tetragonal lattice parameters and, without an independent measure of the cubic lattice parameter, $a_0 = (ca^2)^(1/3)$, which assumes that there is no volume change at T_C. For $l =< 111 >$ or $v_{200} = v_{020} = v_{002} = 1/3$ the strain $\epsilon_p = 0$ because $v_{200} + v_{020} + v_{002} = 1$ and $l_1^2 + l_2^2 + l_3^2 = 1$. The maximum poling strain of $(2(c-a))/(3a_0)$ is obtained for a single domain with $< 100 >$ aligned along the electric field direction, while the minimum is $(a-c)/(3a_0)$. The error estimate on the

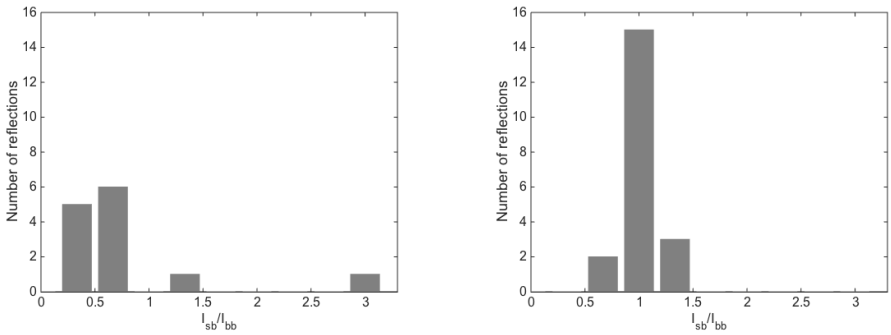

Figure 3.8: Distribution of the ratio of peak intensities measured with a 100 μm beam, $I_s b$, to those measured with a 120 μm beam, $I_b b$. In (a) the median value of 0.62 for 13 reflections indicates that part of the grain likely falls outside the illuminated volume while in (b) the median value of 1.04 for 20 reflections indicates that the grain is fully embedded. Grains such as (a) were excluded from further analysis since the relationship between the peak intensity and domain volume fraction is not reliable.

poling strain is propagated as

$$\sigma(\epsilon_p) = |\frac{c-a}{a_0}| \left[(l_1^2, l_2^2, l_3^2) \sum_{\text{tetr}} (l_1^2, l_2^2, l_2^2)^{\text{T}} \right]^{1/2} \tag{3.3}$$

The relationship between the domain volume fractions and ϵ_p is demonstrated in Figure 3.9, where the bars are divided into three parts representing the volume fraction of each of the three non-180° ferroelastic domains, labelled with the domain c-axis misorientation with the poling direction, and the line is ϵ_p. The applied electric field results in the expected increase of ϵ_p, from $-0.126 \pm 0.003\%$ at F0 to $0.492 \pm 0.014\%$ at F2, a direct result of the growth of d_{002} at the expense of d_{200} and d_{020}. This change is again clearly evident in the shifting of intensity from relatively even ratios at F0 to a very strong peak at F2 in Figure 3.7. The dominant growth of d_{002} is expected since it is by far the most favourably aligned with respect to the electric field vector at a misorientation of 10.5°.

The non-180° switching strain was successfully extracted for 139 of the 165 grains in the reconstructed volume. To combine the microstructural information extracted from nearfield data with the domain volume fractions extracted from farfield data, the volume was input into DREAM.3D [71]. DREAM.3D associates the point by point data containing each voxel's grain ID and the list of associated orientations in a single file using the Hierarchical Data Format (HDF5), which is readily viewed in software such as

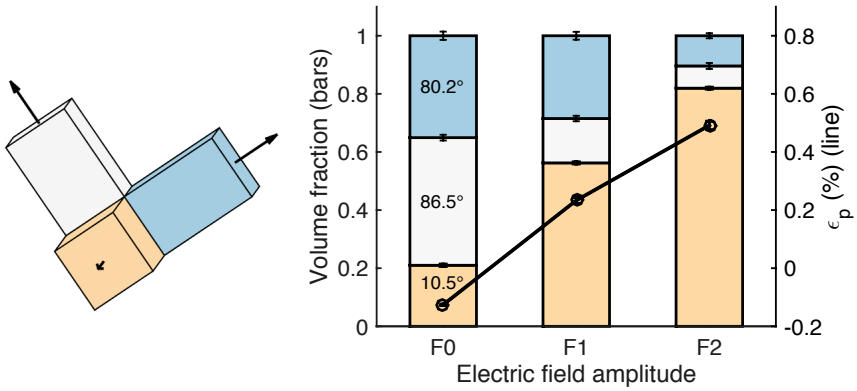

Figure 3.9: The change in volume fraction of domains (bars) with poling and the corresponding non-180° domain switching strain along the poling direction (line) for a [001]-oriented grain. Each segment of the bar represents a domain within the grain of interest and is labeled with the misorientation between the domain c-axis and the applied field direction. The domain *c*-axis orientations are as depicted to the left and the field direction is out of page.

ParaView [72]. Figure 3.3 was generated in the same way. The microstructural grain neighbour information was then extracted using built-in DREAM.3D functionality. The HDF5 format is designed to contain multiple sets of data, and the extrinsic strain information was combined with the volume for visualization, as shown in Figure 3.10 for F0 and F2, now coloured by the extrinsic strain.

3.3 Strain response heterogeneity

The distributions of extrinsic strain for all grains is shown in Figure 3.11 at all steps. It is interesting to note that even in the as-processed state individual grains do not contain equal volume fractions of the three possible ferroelastic domain variants (which would yield ϵ_p=0 from Equation 3.2). This implies that upon cooling from the high temperature cubic phase through T_C, BT grains have a resultant anisotropic ferroelastic strain. Since the grains are coherent at the boundary, there must be elastic compliance strains at the grain scale to compensate for this. It is hypothesized that domain interactions at grain boundaries are the likely cause of such heterogeneity. The electrostatic energy associated with these interactions must outweigh the increased elastic energy caused by the strain heterogeneity. Even so, the strains within the polycrystal as a whole balance and the mean volume weighted strain of the sample as a whole is $\epsilon_{p,F0} = -0.002 \pm 0.001\%$, as expected. The broadening of the distribution at field steps F1 and F2 is expected even without consideration of grain neighbour-

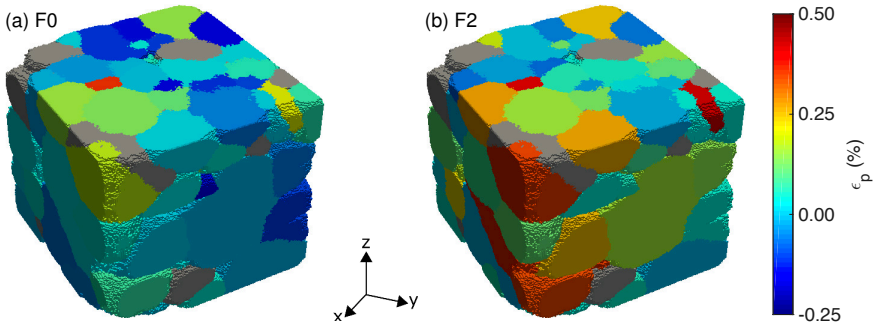

Figure 3.10: Grain maps of the entire sample color coded according to (a) $\epsilon_{p,F0}$ and (b) $\epsilon_{p,F2}$. The poling direction is along the vertical z-axis. The grey grains are the ones where the fit of domain volume fractions failed, primarily grains on the top and bottom surfaces that were removed from the analysis because they extend beyond the illuminated volume.

hood since the grains are randomly oriented and the polarization switching response is orientation-dependent, to a first degree, as demonstrated in the following section.

3.4 Ferroelastic strain response as a function of grain orientation

The inverse pole figure in Figure 3.12(a) shows the orientation of all grains, coloured by the difference in non-180° domain switching strain between the F0 and F2 states, from hereon termed the ferroelastic strain response. The pole figure indicates that the grains are randomly oriented, in agreement with the Mackenzie plot in Figure 3.4. From Figure 3.12(a), there is a general trend towards maximum and minimum ferroelastic strain response occurring at grain orientations with a $< 100 >$ and $< 111 >$ direction lying close to the electric field vector, respectively, as expected from the definition of ϵ_p in Eq. 3.2 as well as from previous powder diffraction results [73, 74, 33, 75]. However, in addition to the observed first order correlation between grain orientation and ferroelastic strain response there are significant variations, or second order perturbations, within groups of grains with similar orientations. This can be seen in the spread arount the linear fit in Figure 3.12(b), showing the ferroelastic strain response as a function of $\cos^2 \phi_{100}$, where ϕ_{100} is the misorientation between the electric field vector and the closest $< 100 >$ direction in the given grain. Although it would be reasonable to think that grains with an initially negative strain would have more potential for domain switching and thus a larger ferroelastic strain response, the magnitude of initial ferroelastic strain, $\epsilon_{p,F0}$, in a grain did not show any correlation with the response under high electric field. The average volume-weighted extrinsic strain for the grain as a whole is as expected, again zero at the initial state ($\epsilon_{p,F0} = -0.002 \pm 0.001$

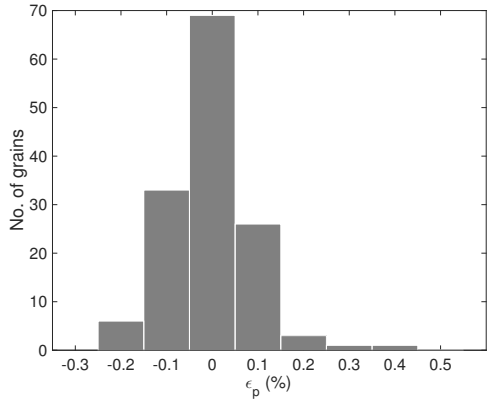

(a) F0

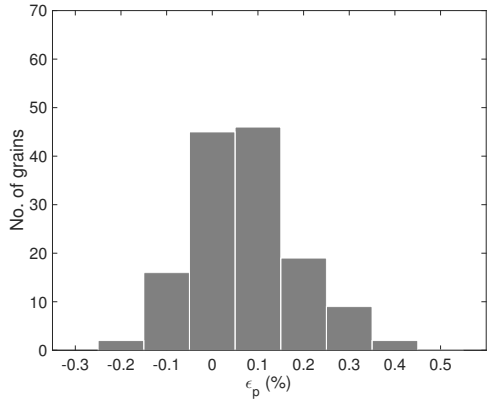

(b) F1

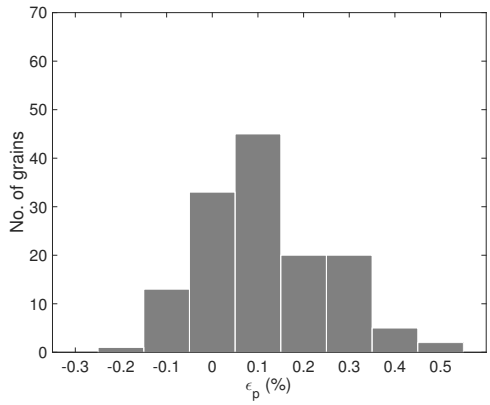

(c) F2

Figure 3.11: Distribution of extrinsic strains obtained from farfield diffractin data at all field steps.

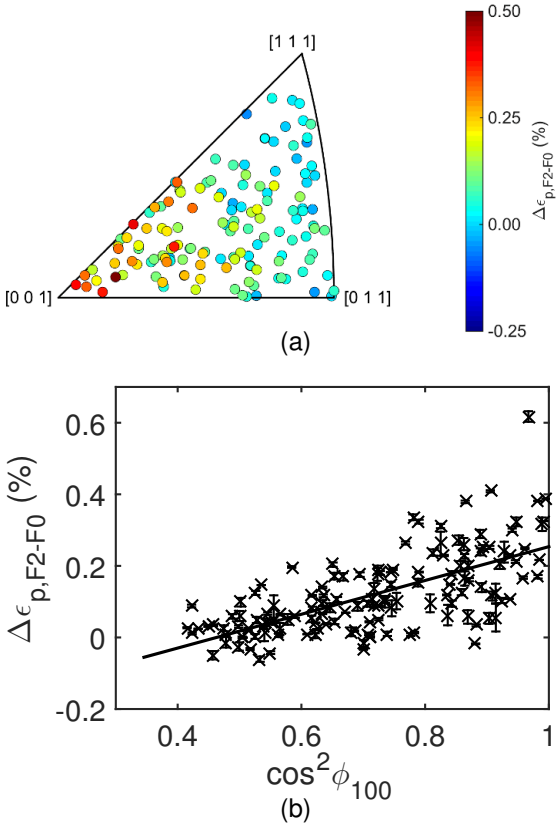

Figure 3.12: (a) The orientation of the 139 indexed grains colour-coded according to the ferroelastic strain response from step F0 to F2, and (b) as a function of $\cos^2\phi_{100}$, where ϕ_{100} is the misorientation between the electric field vector and the closest $< 100 >$ direction in the given grain. The trend line in (b) corresponds to the average behaviour expected for a given grain orientation.

%) before increasing upon application of an electric field ($\epsilon_{p,F1} = 0.088 \pm 0.001$ % and $\epsilon_{p,F2} = 0.135 \pm 0.001$ %).

To study the effect of grain response averaging, the RMS distance to the trend line in Figure 3.12(b) was calculated for a rolling average of grains of similar orientation at a variety of group sizes. It was found that the RMS distance was halved for groups of 10 similarly oriented grains as compared to individual grains, which agrees well with a previous investigation on BNKT utilizing the same far-field 3D-XRD technique [70], as discussed previously. The reconstructed grain map will now be used to examine some potential causes of this second-order deviation.

3.5 Effect of grain size and bulk location

The effect of grain size on ferroelastic response is shown in Figure 3.13(a) relative to the trend line in Figure 3.12(b). The grain diameter here and where follows is calculated from the volumes derived from the grain map by assuming that the grains are perfect spheres. The correlation coefficient of 0.1 indicates that there is no significant correlation between grain diameter and ferroelastic strain response. Although previous experiments [74] and simulations [76] have demonstrated the effect of average sample grain size on domain switching behaviour and material response, this effect does not appear to be present at the single grain level.

So far it has become clear the the three-dimensional constraint on a grain in a polycrystal has a significant effect on the structure and therefore, the ferroelastic strain response. Within a single sample the surface grains experience constraint due to the relaxed elastic and electrostatic boundary conditions at the sample surface [77]. Thus one would expect a clear difference in response (refer again to Figure 1.7). The distribution of ferroelastic strain response deviation from the trend line is shown in Figure 3.13(b) for the 50 bulk grains in the sampled volume and in Figure 3.13(c) for the 89 surface grains. The average of the bulk distribution is -0.01% with a spread of 0.11%, while the average and spread for the surface grains are 0.01% and 0.07%, respectively. This implies that there is no significant difference between bulk and surface grains in terms of their mean deviation from the linear trend, however, the spread of response magnitude in the surface grains is significantly lower than for bulk grains, with the probability of equal spread in the two distributions calculated as 0.06% for all data points and 3% for data points within the range of ± 0.2% from the trend line. While the mean difference is insignificant, the larger variation in the bulk grains does support the effect of reduced constraint at the sample surface.

Another characteristic of a grain neighbourhood is the number of contact neighbours that a grain has. This is, of course, related to both the grain diameter and location, i.e. small/surface grains generally have fewer neighbours than large/bulk grains. However, the correlation coefficient between the ferroelastic strain response deviation from the trend line and the number of neighbours is again just 0.2. It is generally concluded that

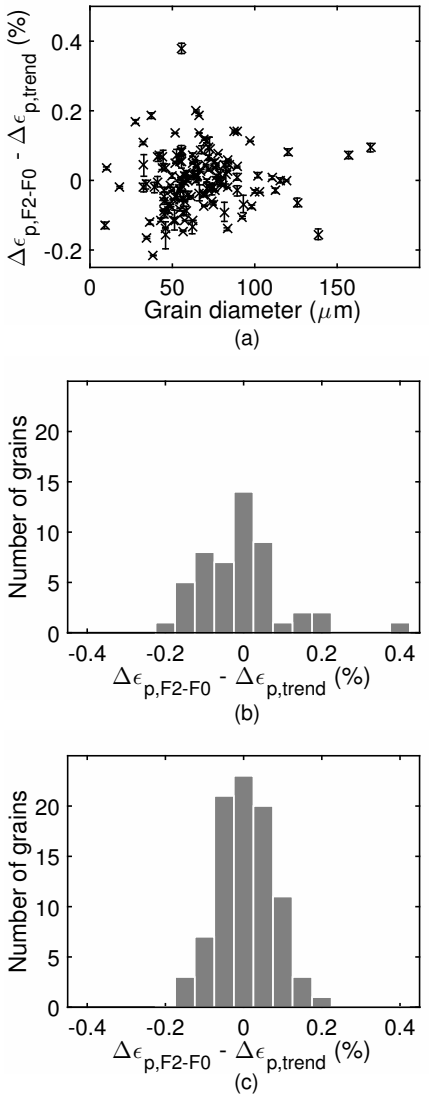

Figure 3.13: Ferroelastic strain response difference from average behaviour as a function of grain diameter (a), and distribution of ferroelastic strain responses away from average behaviour for the 50 bulk grains (b) and 89 surface grains (c).

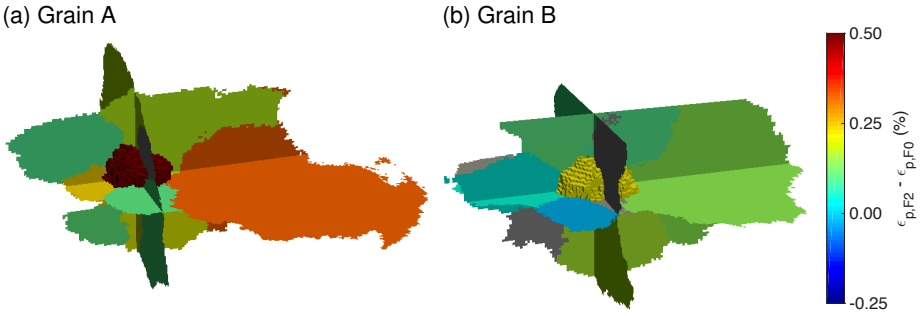

Figure 3.14: Cutouts of the grain map showing grain A and B and their respective neighbours colour-coded according to the ferroelastic strain response of each grain. No strain information was fit for the grey neighbour grains, but their sizes and orientations are known.

neither the grain diameter nor number of neighbours or the location of grains within the sample have any significant effect on the ferroelastic strain response of individual bulk grains within the polycrystalline BT sample.

3.6 Effect of grain neighbour relations

Our results have demonstrated that the average ferroelastic strain response of a polycrystalline BT piezoceramic depends on grain orientation, with heterogeneities at the scale of individual grains that cannot be explained by grain size or location. We can now extract two grains for comparison, to better inspect the effects of grain interactions. The properties of two bulk grains, A and B, and their neighbours are summarized in Table 3.1. The grains are of similar orientation relative to the electric field vector ($5^\circ < \phi_{100} < 15^\circ$ for both) and have similar grain diameters, slightly smaller than the sample average of 64 μm with a spread of 25 μm, yet they exhibit significantly different non-180° ferroelectric domain switching strain responses. Grain A, which was used as an example in Figures 3.6 and 3.7, corresponds to the point in the upper right corner of Figure 3.12 and exhibits the largest response of all grains, while grain B lies very close to the trend line.

Both grains have a similar number of neighbours, 10 for A and 14 for B, which is comparable to the sample average of 11 with a spread of 5. On average, the neighbours of grain B are larger than those of grain A, but the neighbourhood of grain A contains two very large grains with diameters 78 and 85 μm, while the largest neighbour of grain B has a diameter of only 63 μm. The neighbourhood cut-out in Figure 3.14, coloured by the strain response, also indicates that it is not only grain A that has a larger strain response than B, but so does its immediate neighbourhood as a whole. Such a collective response of grain neighbourhoods could indicate the clustering of grains of similar

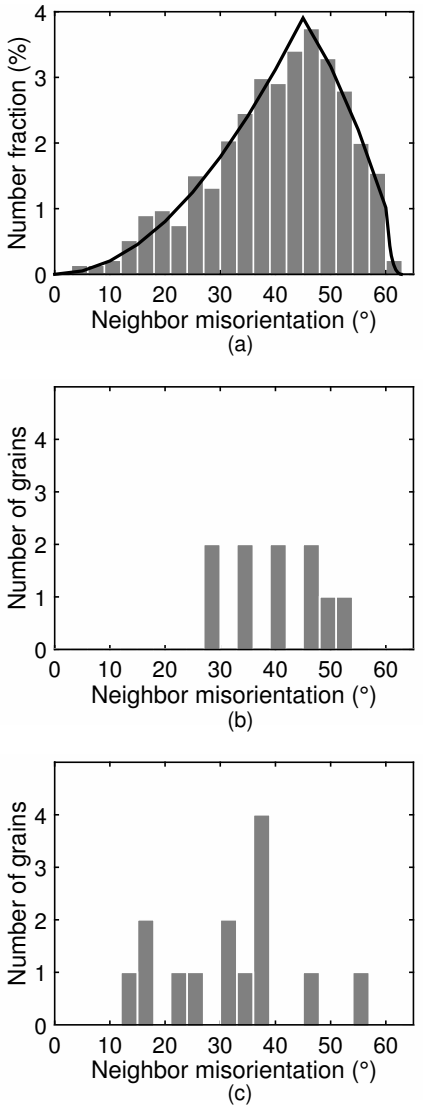

Figure 3.15: Mackenzie type plot for all misorientations of neighbouring grains within the sample volume and the theoretical distribution of random orientations (a), neighbour misorientation distribution for grain A (b) and grain B (c).

Table 3.1: Properties of the two selected grains A and B. For the neighbour diameters, neighbour orientation relative the poling direction (ϕ_{100}) and neighbour misorientation relative to the grains in question, both the average and spread of the distribution over all neighbours for grains A and B are given

		Grain A	Grain B
ϕ_{100} (°)		10.5	7.17
Grain diameter (μm)		56	55
$\epsilon_{p,F2} - \epsilon_{p,F0}$ (%)		0.617±0.015	0.217±0.002
Volume fraction switched from F0 to F2		0.61	0.21
Number of neighbours		10	14
Neighbour diameter (μm)	average	36	43
	spread	44	28
Neighbour ϕ_{100} (°)	average	36	43
	spread	15	25
Neighbour misorientation (°)	average	40	32
	spread	8	12

orientation, however, the Mackenzie type plot in Figure 3.15(a), which takes into account only misorientations between neighbouring grains, again follows the theoretical distribution expected for random orientations (shown as a line). This indicates a random texture, even among neighbours. For comparison, the distributions of neighbour misorientations for grains A and B are shown in Figure 3.15(b) and (c), respectively. Here we observe a difference in the misorientation distributions of the two grains, also indicated by the mean and spread of the two distributions given in Table 3.1. It has been suggested that so-called $\Sigma 3$ boundaries may play a role in connection with continuity of ferroelectric domain structures across grain boundaries [78, 79]. These types of boundaries have a misorientations close to 60°, however neither grain A nor B have neighbour misorientations of this type. In general, Figure 3.15(a) suggests that a random grain in the polycrystalline BT sample is statistically likely to be surrounded by neighbours that come very close to the average structure of the entire sample, while Figure 3.15(b) and (c) clearly demonstrate that in reality an individual grain sees a local neighbourhood that is significantly different from the statistical average.

3.7 Quantification of grain interactions by experiments and modelling

In general, the results presented here show that while the bulk macroscopic properties and response are predictable, at the grain-scale the material behaviour is far more localized in nature due to the grain-to-grain interactions. This effect is also quite evident when comparing self-consistent (SC) models, which considers the polycrystal to be a homogenized matrix in which the grain is embedded, to multi-grain finite element (FE) models, which preserve the individual grain-to-grain interactions. Haug et al. [51] reported that while both SC and FE models capture the polarization hysteresis and strain butterfly loops (such as shose in Figure 1.9), SC models consistently underpredict the maximum stresses and strains that can develop at grain boundaries. These arise due to the forced compatibility between grains, as the sample is poled and differently oriented grains respond to varying degrees. In fact, recent simulations have shown a large spread in intergranular residual stresses even when no field is applied and the average internal stress is zero [80], as has been demonstrated experimentally here.

While the macroscopic response is important for design, it is these maximum stresses and strains that can limit the performance and lifetime of piezoceramics and are in fact quite important for the reproducibility and reliability of the ferroelectric response. Regions of high stress concentration tend to serve as crack initiation sites which can lead to failure of the material. There is also evidence of large *intrinsic* strain heterogeneities in the raw diffraction data in Figure 3.7, where the intensity in between the peaks at $2\theta_{\min}$ and $2\theta_{\max}$ is greater than just the sum of the tails of the peaks. This indicates a lattice strain distribution within the grains that tends towards the common pseudocubic orientation. From the information currently available, we infer that this effect serves to aid compatibility at the domain boundaries [81], but in the future techniques such as dark field X-ray microscopy [82] will enable direct measurements of the spatial distributions of intrinsic strains within individual domains.

The results presented here can also be used to inform current modelling approaches, the majority of which do not match the complexity observed in the experimental data presented here. Typically, only the effect of grain orientation is considered, assuming that all grains are of equal size with all domains of equal volume fraction [51, 83, 84], while we clearly demonstrated here that this is not the case. As an example of the effect of domain volume fractions, FEM simulations by Kamlah et al. [83] show that when there is limited potential for domain switching the amount of strain "available" to the grain is greatly reduced. Thus, two neighbouring grains, even though they are of similar orientation and size, may develop high intergranular stresses if one of them has more availability for domain switching than the other. Figure 3.12 clearly indicates that this is the case even in the as-processed state and should be an important consideration for modelling of real materials. Models such as those based on crystal-plasticity finite element, where the incremental transformation by domain wall motion is equivalent to incremental slip on a slip system, could in turn aid in the interpretation of these results, as they can reveal information on length scales that are not accessible

to the current experiment. Such combined experimental and modelling approaches have previously been used to study deformation twinning in hexagonal close packed metals such as magnesium [52, 85] and zirconium [53, 54].

3.8 Conclusions and perspectives

The combination of nearfield and farfield 3DXRD presented here has yielded a novel set of data from which the grain-scale non-180° switching strains can be correlated to microsctructural parameters in three dimensions. The results indicate a large degree of heterogeneity on the grain scale in both the as-processed state and after applying an electric field. To some extent, this was expected since such results have been obtained for processes in many polycrystalline materials undergoing processes such as deformation twinning [52, 53, 54]. Effort has been made to combine the two data sets from different measurements in a way that makes them accessible for visualization as well as modelling, where all the information is stored in a single file that can be easily shared and accessed. This is one of the key goals of computational materials science approaches and is of great importance for its success.

Statistical analysis of the volume fraction evolution relative to microstructural features did not reveal any immediate effects of grain neighbourhood or grain position in the sample. The effects may be on an even more localized scale and extracting the domain-scale full elastic strain tensor would be of great value to this work. As it turns out, we have not yet extracted all the information available in the diffraction signal. In the following Chapter we will present a newly developed methods towards this goal.

Chapter 4

Indexing and refinement of domain-scale parameters

In the previous chapter, the domain volume fraction evolution was considered with respect to three domains, where the c-axis of each domain variant was oriented along one of the three original cubic a-axis directions. These domains were resolved from splitting of the diffraction peaks in 2θ and, for extrinsic strain calculations, assumed to be at 90°. However, for a tetragonal crystal, an exact 90° reorientation of the c-axis does not create a coherent boundary and the domains are actually twins on the {011} family of planes, as shown in Figure 4.1. The angle between the c-axes of a parent and a twin is a function of the crystal aspect ratio given by

$$(90 - \psi) = 2\tan^{-1}\left(\frac{a}{c}\right) \tag{4.1}$$

where $(90 - \psi) = 89.39°$ for the polycrystalline sample considered here with lattice parameters $a = 4.0042$ Åand $c = 4.0472$ Å. The misorientation between the a and c axes is therefore 0.61°. This slight obliquity results in splitting of intensity in η and ω, which therefore carries additional information about the orientation and structure of these domains and domain walls. Recent studies suggest that, in reality, domains of polycrystalline ferroelectrics are not perfect twins [86], experience strain fields around domain walls that are larger than previously thought, and can locally break symmetry [87]. All of this is thought to be due to the three-dimensional constraint under which grains are found in a ceramic.

First we will make some qualitative observations about the diffracted signal and what it can tell us about the domains structure. Consider a grain oriented as indicated by point

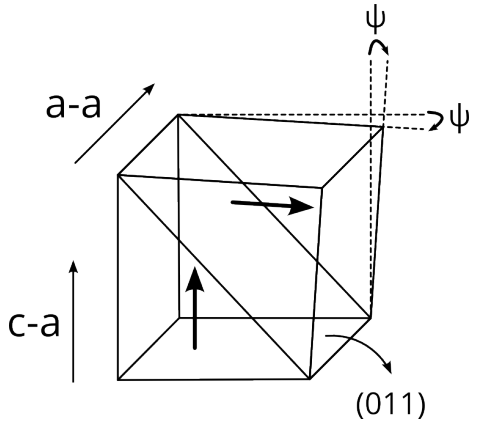

Figure 4.1: A schematic representation of the tetragonal twinned lattice showing the obliquity angle, which depends on the lattice c/a ratio. This slight misorientation between domains gives rise to additional peak splitting in the diffraction pattern. The twins are a-a type or c-a type depending on the viewing direction, as indicated.

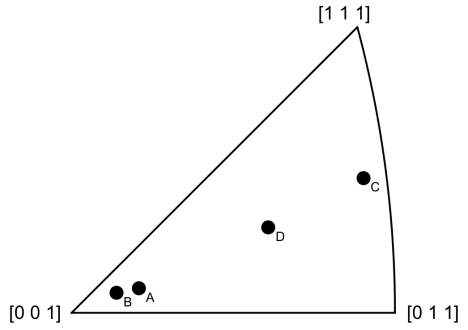

Figure 4.2: Orientation of some grains of interest. Grain A and grain B are the same as for the previous analysis.

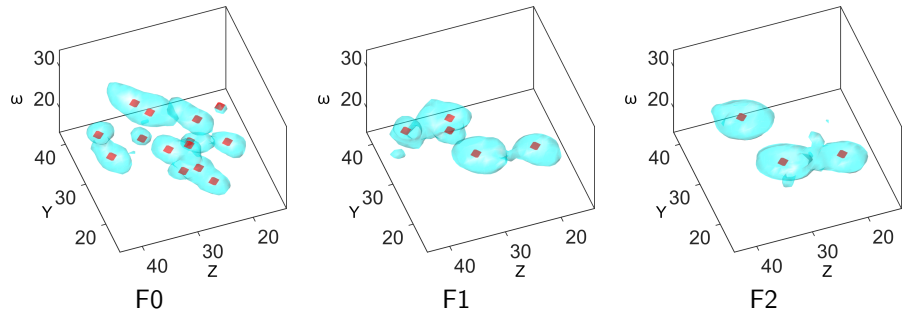

Figure 4.3: The evolution of the same cluster of (200)/(002) peaks from F0 to F2 for a single grain. Cyan is the cloud of intensity above the threshold, $t = 300$ and red spots are the local maxima. The large number of maxima present at F0 suggest multiple diffracting structures with varying lattice parameters or orientations, or both. With an applied field the structures are consolidated as evidenced by the decrease in local maxima at F1 and F2.

C on the inverse pole figure in Figure 4.2. A cluster of (200)/(002) peaks originating from this grain is shown in Figure 4.3 where the red dots are the local maxima and the cyan is the cloud of intensity above the threshold, $t = 300$. The large number of local maxima observed at F0 suggest that the grain consists of many coherently diffracting structures rather than just the main tetragonal twin variants. When a field is applied, the many small peaks are consolidated into three broad peaks with a more twin-like angular relationship, as will be discussed further in the chapter. The broadness of the peaks suggests a strain or orientation through the grain which may be due to a lamellar or herringbone pattern in which small misorientations between layers accumulate through the structure.

While there is a significant reduction in the number of domains, the change in the domain volume fraction of the three non-180° domains, shown in Figure 4.4, is insignificant, and the reorganization of these domains does not result in an extrinsic strain in the grain. Many-domained structures such as these suggest that the grain experiences a very localized environment upon the transition from cubic to tetragonal, which could be due to heterogeneous electric fields or intergranular stresses. In Chapter 3, there was no correlation found between the extrinsic strain in the as-processed state and the total response of the grain, however, this did not take into consideration the arrangement of these domains, which can vary significantly while yielding the same nominal domain volume fractions. The interaction of strain fields around these many structures may contribute to heterogeneity observed in the response of grains with similar orientations, perhaps delaying the response in some grains as the many domains are first consolidated into a more favourable arrangement for large-scale switching.

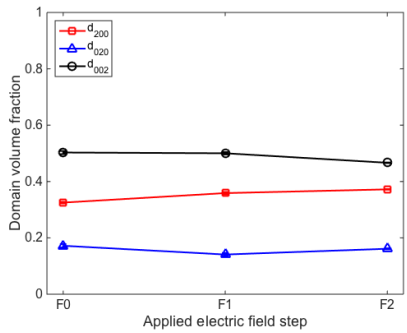

Figure 4.4: Domain volume fraction evolution of the three non-180° domains of grain C. Although significant reorganization of domains is observed in Figure 4.3, the volume change of the domain types is not significant.

While such observations support an understanding of the material, it is impractical to study the diffraction spots for each grain in a large data set. Additionally, realistic modelling and domain engineering efforts require quantitative information with statistical value. The goal of this work is ultimately to index and refine the domain-scale parameters, which 3DXRD has been used to do on the grain-scale in many materials. The basic premise of 3DXRD is to (i) identify the location of scattered X-rays and (ii) associate the scattered intensity with a "diffracting structure", be it a grain or a domain. This task is more complicated in the multi-domain case because of the mosaicity and high-density of peaks, which make peak segmentation by traditional methods more difficult, and increases the likelihood of peak overlap. 3DXRD was first successfully applied to ferroelectrics by Varlioglu et al. [86] to determine the orientation of domains for a single grain of BT embedded in a polycrystalline sample. Varlioglu et al. combated the problem of peak assignment by heating the specimen above the Curie point where BT is cubic and tracking the peak splitting as the sample cooled and transformed to tetragonal. This helped ensure that the diffraction spots were associated with the correct grain and assigned to the correct domain. Additionally, the beam was focussed in a small region on the sample, centred on the grain of interest. In the study presented here, the cubic state was not measured and all grains were illuminated simultaneously with a box beam. Initial analysis of the data again indicated that the usual peak identification (eg. thresholding) and indexing methods (GrainSpotter) were not adequate to resolve the domain structure. Instead, an alternative structural refinement procedure will be presented whereby the diffraction peak location of multiple domains is forward projected and then associated with a measured peak in the data volume, if it exists. As the deviation between the measured and projected pattern is minimised the grain and domain-scale orientation and lattice parameters are refined. The procedure will be demonstrated for one grain, and suggestions for further automating and extending the algorithm will be discussed.

4.1 Forward projection

We start with the list of grain orientations and positions obtained from the nearfield analysis in Chapter 3. The orientation is a nominal grain orientation rather than that for any distinct domain. The orientation matrix for a twinning operation on a plane specified by (hkl), m_{hkl}, is calculated as a 180° rotation about the plane normal, most conveniently using the axis-angle rotation representation. Now we can calculate the orientation matrices of each twin variant in the sample system $U_{t,hkl}$, as:

$$U_{t,hkl} = U m_{hkl} \tag{4.2}$$

where for the tetragonal system there exist four unique twins on the (011), $(0\bar{1}1)$, (101), and $(\bar{1}01)$ planes. Double twin orientations can be generated by repeating the calculation for any or all of the twins, yielding up to 17 unique orientations for a single parent orientation. To locate the diffracted intensity originating from these domains, the scattering vector is calculated in the laboratory system, x along the beam direction, z along the sample rotation axis, and y normal, based on the the experimental geometry described in Figure 2.5 and Equations 2.10-2.14. Since the grain position and the sample to the detector distance are known, the position of the diffracted intensity as it hits the detector can be calculated. This position is converted to a pixel index on a detector with origin at the bottom right as

$$\begin{aligned} y_{\text{det}} &= y_l/\text{px}_y + y_{\text{det},0} \\ z_{\text{det}} &= z_l/\text{px}_z + z_{\text{det},0} \end{aligned} \tag{4.3}$$

where (px_y,px_z) is the detector pixel size and $(y_{\text{det},0}, z_{\text{det},0})$ is the trasmitted beam centre centre position on the detector, in pixels.

Each projected (hkl) yields two projected maxima (Friedel pairs), which are theoretically both be measured when the sample is rotated through 360°. In this experiment the interference and shielding from the poling apparatus makes roughly 15° of the image stack unusable. Still, there are many observations for each grain. The diffraction spots of the different domains form split peaks, or clusters of peaks, such as those shown schematically in Figure 4.5. Each peak cluster contains a contribution from each of the domains, shown for a parent orientation and the four twins in Figure 4.5(a). Some of the peaks may overlap as in Figure 4.5(b) where domains 1, 2, and 3 yield one peak position and domains 4 and 5 the other two. The projected peaks are clustered based on their position on the detector (y_{det}, z_{det}) and their corresponding ω, which identifies the diffraction image on which the peak should be measured. The region of interest (ROI) is then extracted as a volume where the 1 and 2 dimensions are the detector plane and the 3 dimension is the image stack. A voxel in this volume is then 1 pixel × 1 pixel × 1 image ω. The ROI size is chosen as the range of the projected peaks with some padding in the row, column, and ω directions to make sure that all of the grain intensity is captured.

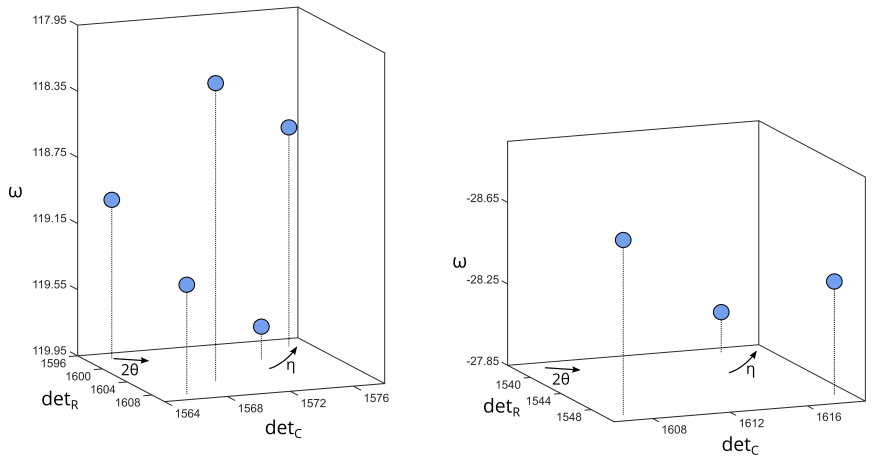

Figure 4.5: Projected (200)/(002) peak clusters for a parent grain and the four unique twin domain variants. In (a) all peaks are visible whereas in (b) domains 1, 2, and 3 overlap at $2\theta_{\text{max}}$. The region of interest is extracted from the corresponding detector image (ω) and the row (det_R) and column (det_C) index of the detector pixels. The 2θ and η directions of the diffraction ring are as indicated.

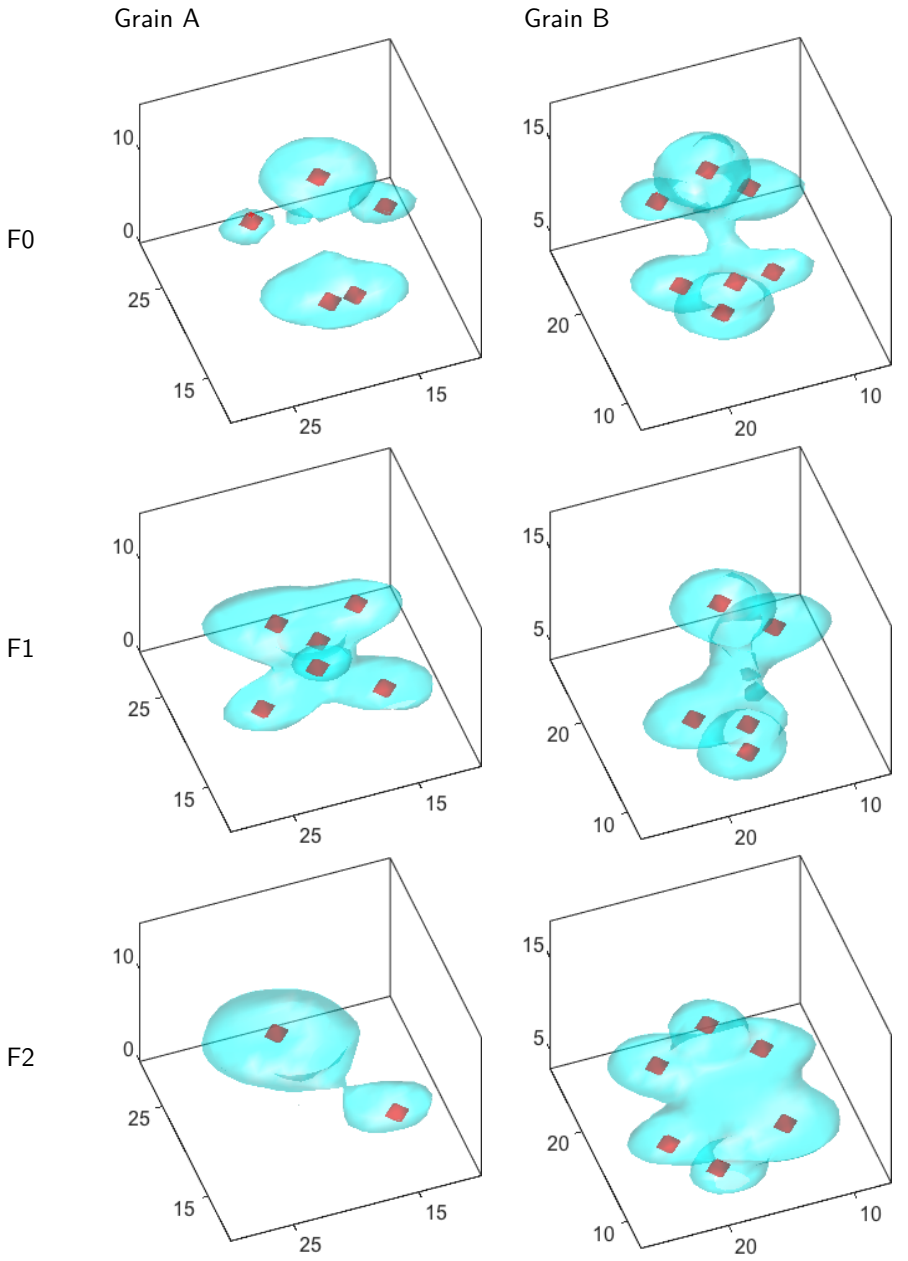

Figure 4.6: Intensity of a cluster of (200)/(002) peaks at F0, F1, and F2 for a grain with a large non-180° switching strain response (A) and a grain with a small response (B). Cyan is the cloud of intensity above the threshold, $t = 750$ and red dots are the local maxima. The grains are of similar size and orientation.

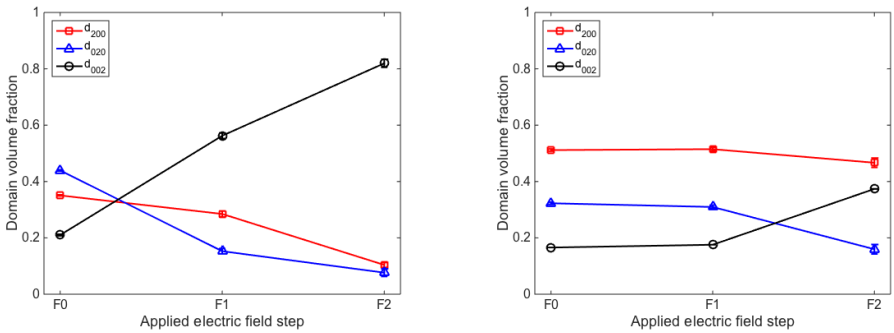

Figure 4.7: Domain volume fraction evolution of (a) Grain A, a high response grain and (b) Grain B, a low response grain. The grains are of similar size, orientation, and position within the sample (bulk).

To examine the twinning model in the context of real data, consider again grains A and B from the previous analysis. They are of similar size and orientation, yet grain A exhibits a much larger strain response than does grain B. A (200)/(002) diffraction peak clusters belonging to each of the grains is shown as a three-dimensional volume in Figure 4.6, both with a threshold $t = 750$ at all poling steps. Here the peak arrangement in the as-processed state much more closely resembles that expected for twinning, as in Figure 4.5. Note that peak splitting is observed at both 2θ angles. This may be consistent with the spontaneous, simultaneous formation of all possible twins upon the transformation from cubic to tetragonal, where each of the a-axis directions is equally likely to form the polar c-axis and maintain coherence by twinning. However, it could be double twinning. It is difficult to tell the difference, as expected since the reorientation is roughly 90°. The mechanism behind this type of twin domain formation is different from the case of deformation twinning, where the parent grain is typically of a single domain which forms a twin and subsequently a twin within the twin. Examining the evolution of domain volume fractions for the two grains, shown in Figure 4.7, it is clear that that the response of grain B lags relative to grain A, where we see the significant growth of d_{002} in grain A right at F1 and a change is only observed for grain B at F2. From the diffraction signal, however, it is clear that some domain switching is occuring in grain B even at F1. It is interesting to note that there is initially a reduction in local maxima for grain B at F1 and an increase at F2. For both grains, the peaks in the field step at which a change in domain volume fractions is first observed are very broad and interconnected compared to F0, with significant intensity in between the two 2θ angles, as was noted in Chapter 3. This suggests that some portion of the grain tends towards a pseudocubic orientation, perhaps to accomodate the domain switching that is occuring. Aside from the initial domain structure, another explanation for the delayed response of grain B could be a back-stress from the transformation or constraint of a neighbour grain or perhaps pinning by some structural defect. We would like to further elaborate on this point,

and for this we require indexing and refinement the domain-scale orientations and lattice parameters of this grain and of its neighbours.

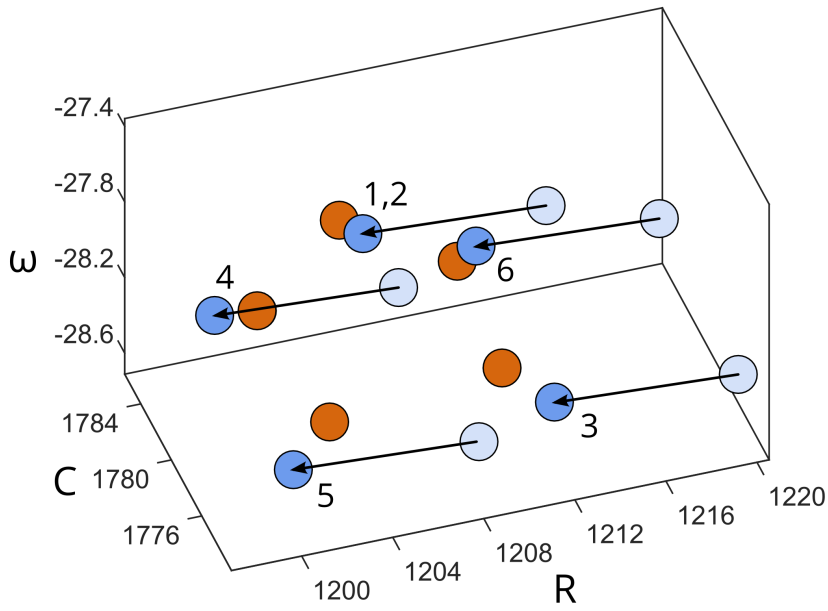

Figure 4.8: Assignment of projected (blue) to measured (red) (200)/(002) peaks for a single grain. In light blue are the peaks as initially projected and in dark blue after a rigid body translation bringing the centroid onto that of the measured peaks. Domains 1 and 2 are overlapping and assigned to the same local maxima. Domains 5 and 6 are double twins.

To proceed with the refinement, the measured local maxima are assigned to a projected domain variant and corresponding (hkl) index. This is done using a two-step process:

1. A rigid body translation of the entire projected cluster to place the centroid of the projected peaks onto the centroid of the measured peaks
2. Assignment of measured peaks to projected peaks such that the total deviation is minimized

as shown in Figure 4.8. When two projected peaks are coincident, as those belonging to domains 1 and 2 in Figure 4.8, they are assigned to the same local maxima. The total deviation between the projected diffraction pattern and the measured diffraction

pattern for N assigned peaks is

$$D = \sum_{i=1}^{N} [(P_{y,i} - M_{y,i})^2 + (P_{z,i} - M_{z,i})^2 + [(P_{\omega,i} - M_{\omega,i})/\Delta\omega]^2]^{\frac{1}{2}} \tag{4.4}$$

where $(P_{y,i}, P_{z,i}, P_{\omega,i})$ and $(M_{y,i}, M_{z,i}, M_{\omega,i})$ are the projected and measured peak positions, respectively, and $\Delta\omega$ is the angular step size between consecutive images, in this case 0.1°. In this way, an image has the same weight as a pixel in the deviation calculation. The general procedure is summarized in the flow chart in Figure 4.9 and will be demonstrated for a single grain in the section to follow. The code has been implemented in MATLAB with the following features:

- forward projection
- image reading and extraction of ROI
- identification of local maxima
- peak assignment
- deviation calculation

The total deviation for all peaks that have been assigned is minimized using the built-in MATLAB function `fminsearch`. At the grain scale, the parameters refined are the parent orientation and the position of the grain as a whole. At the domain-scale, the parameters are the orientation as well as the lattice parameters a, b, c, α, β, and γ. All orientations are fit as Rodrigues vectors.

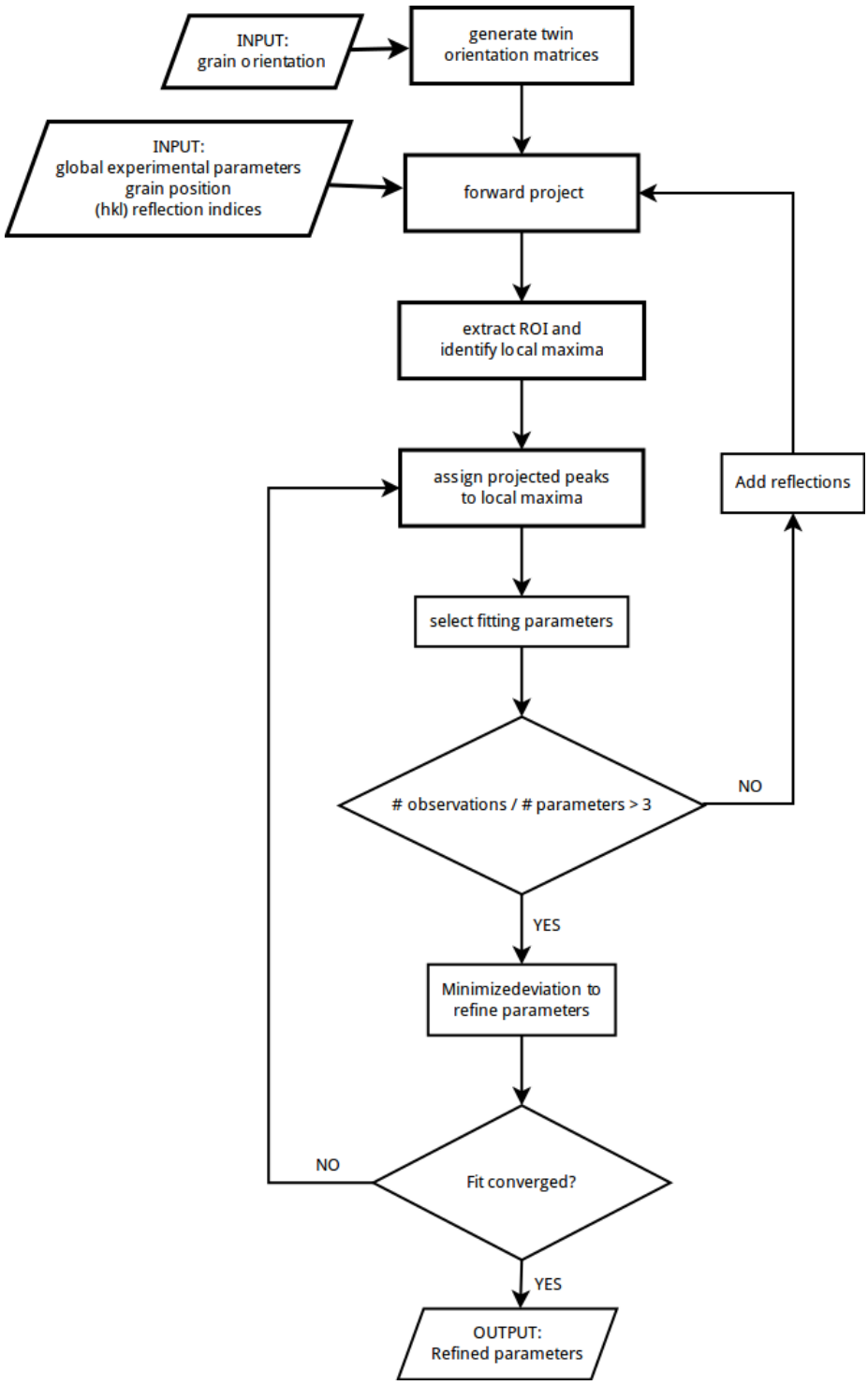

Figure 4.9: Schematic diagram describing the iterative forward projection and refinement procedure.

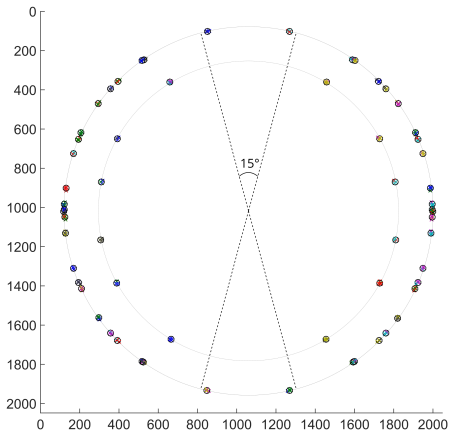

Figure 4.10: Clusters of projected peaks shown in their position on the detector face. Peaks falling on the same pixel positions at different ω values are overlapping. The inner and outer rings contain the (200)/(002) and (211)/(112) reflections, respectively. Reflections falling within 15° of the poles were excluded from the analysis.

4.2 Feasibility study for a single grain

The grain selected to demonstrate the fitting procedure is oriented as labelled D on the inverse pole figure in Figure 4.2. The [0 0 1]-oriented grains such as A and B pose a challenge for indexing because many of the (200)/(002) peak clusters fall at the poles of the diffraction image, where they remain in the diffracting condition through a large ω range. This makes it very difficult to identify the local maxima, and as will be demonstrated, a first refinement of grain orientation and position on the (200)/(002) rings is important for a successful refinement. The projected peak positions for the (200)/(002) and (112)(211) reflections of grain D are shown on the detector face are shown in Figure 4.10, where peaks at the same position on the detector but a different ω are overlapping. Reflections within 15° of the poles were excluded. The results of the refinement at each step are summarized in Table 4.1 where the completeness is reported as the ratio of assigned to projected peaks and the average misorientation between the projected and measured g-vectors is the mean internal angle (IA). The discussion below refers to fitting of domains at field step F0.

The first step in the fitting procedure was to identify existent domains. Observation of the diffraction spots indicated double twins, so the twin and double twin peak positions were projected. One of the characteristics of diffraction from twinned crystals is peak overlap for some but not all reflections. In the context of the analysis presented here, this means that some domains overlap in some peak clusters but not in others. For example, in Figure 4.11 are projected 7 domains in blue, which appear to be

Table 4.1: Fitting statistics for all domains of grain D at each converged fitting step.

	N_{proj}	N_{meas}	N_{asgn}	N_{pars}	$N_{\mathrm{obs}}/N_{\mathrm{pars}}$	D/N_{asgn}	$\frac{N_{\mathrm{asgn}}}{N_{\mathrm{proj}}}$	mean IA °
F0	72	72	72	6	12	0.288	1.00	0.0119
	360	478	264	6	44	0.127	0.73	0.0107
	360	478	224	21	10.7	0.109	0.62	0.0086
	360	478	224	54	4.1	0.107	0.62	0.0084
F2	36	38	36	6	6.0	0.415	1.00	0.0128
	180	294	146	6	24.3	0.168	0.81	0.0108
	180	294	125	12	21.3	0.169	0.69	0.0098
	180	294	125	27	4.3	0.166	0.69	0.0097

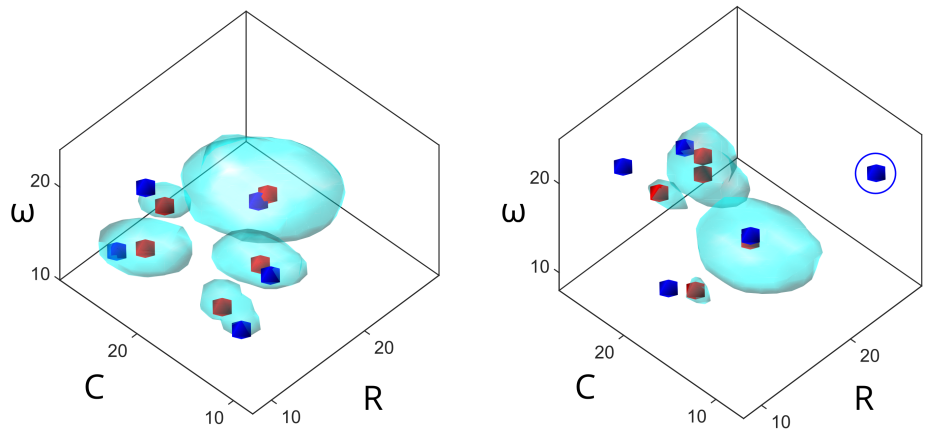

Figure 4.11: (200)/(002) peak clusters of domain D. Blue spots are the result of projecting 7 domain orientations, red spots are the local maxima and cyan is the cloud of intensity above threshold $t = 300$. In (a) the projected domains overlap in a manner consistent with the observed local maxime, while in (b) one of the domains yields a peak that is not measured, circled in blue.

consistent with the measured diffraction pattern. But in (b), a peak cluster in the same grain, one of the domains generates a peak that is not measured, circled in blue. For the grain presented here, the local maxima were assigned to projected peaks as described previously, with a tolerance of 5 voxels. The projection-assignment-refinement procedure was then performed iteratively and at each step domains with completeness below 50% were removed until only those domains for which there existed measured maxima in all peak clusters remained. This yielded six unique domain orientations with a completeness of 100% on the (200)/(002) reflections. Relative to the parent orientation, the domain variants are the primary twins on the $(\bar{1}01)$, (011), and $(0\bar{1}1)$ planes, and secondary twins on the (011) and $(0\bar{1}1)$ planes of the (101) primary twin, which itself is not observed.

As can be seen in Figure 4.11(b), there remain maxima within the region of interest that are unaccounted for by these six domains, the origin of which is unknown. It could be, for example, a strained portion of the same twin variant present in another region of the grain or another variant that does not overlap perfectly.

From this inital projection and assignment, the overall grain position and the so-called parent orientation were refined, with the additional domains fixed to perfect twinning orientations. We can see from Figure 4.11 that this is a reasonable starting guess with a deviation of roughly 0.3 voxels per reflection and an internal angle of 0.012°, as noted in Table 4.1. It is this small deviation that we would like to minimize in order to gain information about the individual domain orientations and lattice parameters. Typically we require 3 observations per refined parameter, a total of 27 per domain to refine the 3 Rodrigues orientation parameters and the 6 lattice parameters. The (200)/(002) reflections yield only 12 oberservations so we now include the (211)/(112) family of reflections, which also exhibit significant splitting. Including Friedel pairs, there are 48 (211)/(112) reflections which provide the required observations, but also lie on a diffraction ring that is much more densely populated. In the analysis presented here, regions of interest with more than 20 maxima were excluded due to the high probability of incorrect assignment. Additionally, 4 clusters were excluded at the poles of the diffraction image and 1 cluster was in an angular range shielded by the poling apparatus. In the following steps, convergence means that no peaks were assigned/unassigned and the deviation of the projected peaks from the local maxima was unchanged.

Again asssuming perfect twinning, 264 peaks were assigned for a completeness of 73% over the entire grain and between 60% and 85% for individual domains. In the first step, the grain position and orientation were refined to a deviation of 0.127 voxels per reflection and a mean IA of 0.0107°. After projection of peaks with these refined parameters, 40 peaks were unassigned for deviating by more than 5 voxels and 224 peaks remained assigned. The individual domain orientations were then freed from the perfect twinning relationship, with the twin orientation taken as the starting guess for refinement, and together with the grain position, 21 parameters were refined. This resulted in a significant reduction in the deviation from the measured pattern to 0.109 voxels per reflection and a mean IA of 0.0086°. This can be seen in the shift of the blue peaks for a (200)/(002) peak cluster from Figure 4.12(a) to (c), and for a (211)/(112)

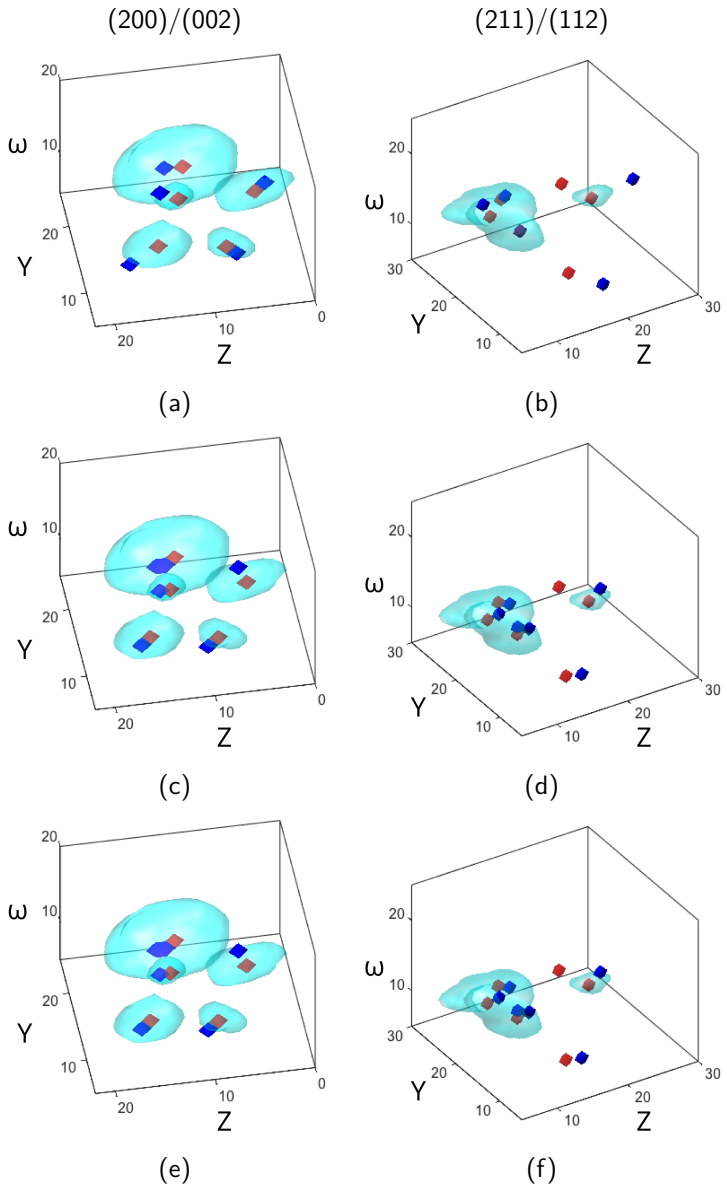

Figure 4.12: Example peak clusters for grain C containing the (200)/(002) and (211)/(112) reflections for grain D after (a)-(b) refinement of grain position and parent orientation, (c)-(d) refinement of grain position and individual domain orientations, and (e)-(f) refinement of orientations and lattice parameters.

Table 4.2: Summary of fitting statistics for the individual domains in Table 4.3

	ID	N_{obs}	$N_{\text{obs}}/N_{\text{pars}}$	$N_{\text{asgn}}/N_{\text{proj}}$	mean IA
F0	1	39	4.3	0.65	0.0082
	2	38	4.2	0.63	0.0087
	3	35	3.9	0.58	0.0081
	4	43	4.8	0.72	0.0086
	5	37	4.1	0.62	0.0093
	6	32	3.6	0.53	0.0076
F2	1	46	5.1	0.77	0.0096
	2	41	4.6	0.68	0.0101
	3	44	4.9	0.73	0.0096

peak cluster from Figure from Figure 4.12(b) to (d).

In the next refinement step, the grain position was fixed and the lattice parameters were refined for a total of 9 observations per domain. From Table 4.2, all domains have at least 3 observations per parameter but we are nearing the limit. This reduced the deviation to 0.107 voxels per reflection and a mean IA of 0.0084°. However, the improvement is small relative to the threefold increase in refined parameters. In Figure 4.12 (c) and (e) the difference is unobservable because it is below the resolution of a single voxel. For this reason, it may not be appropriate to refine all lattice parameters at this stage.

The procedure was repeated in the same way for the grain at poling step F2, where only three domains remained, the $(0\bar{1}1)$ twin and the secondary twins having switched to one or more of the remaining domain orientations. The fit was found to be worse for the F2 data, with both the deviation per reflection and internal angle being larger, and a minimal reduction in the deviation with an increase in the parameters, from 0.168 voxels per reflection and 0.108° for a perfect twinning assumption to 0.166 voxels per reflection and 0.0097° with a full parameter refinement. Although there are fewer domains at F2, the domains are much more broad, suggesting large orientation or strain gradients, or both.

Generally, the mean IA is much lower than that typically observed for refinement of undeformed polycrystals, where 0.1° is acceptable. However, these are obtained with a $\Delta\omega$ increment of 0.25° whereas in this experiment we use a fine $\Delta\omega$ of 0.1°. Additionally, the local maxima were very precisely determined in all dimensions as compared with that obtained for a threshold-based peak segmentation procedure. This precise identification of domains was important here since the misorientations are much smaller than those required to segment entirely independent grains.

The initial identification of existent domains was found to be a key step in the assignment procedure. While all the domains reported here are well-determined, it is difficult to know whether all of the diffracted intensity originating in from the grain

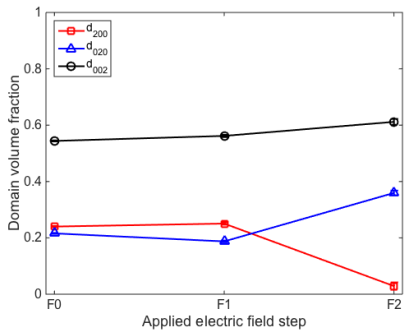

Figure 4.13: Domain volume fraction evolution of grain D.

is accounted for. Additional local maxima such as that in Figure 4.11(b) were observed in other peak clusters. These domains could generate additional peaks in the (211)/(112) regions of interest, in which many local maxima remained unassigned. It is unclear whether these originate from grains nearby in orientation space. In the next implementation of the algorithm a more robust assignment scheme is planned, including shape analysis that takes into account the relative arrangement of projected and measured spots. This should minimize the likelihood of incorrect assignment that will, of course, prevent an accurate refinement of the orientations and lattice parameters. The current implementation of the forward projection algorithm does not take into account detector tilt, and although the images were corrected for spatial distortion, small local distortions may also exist, which will be corrected to obtain a better fit in the future. Finally, grains that are close together in orientation space may be projected simultaneously to help segment the diffraction spots.

4.3 Domain-scale orientations and lattice parameters

The results of the domain orientation and lattice parameter refinement are summarized in Table 4.3. The orientation results are reported simply as the misorientation from perfect twinning, taking the refined domain 1 orientation as the parent. For domains 5 and 6 at F0 the parent is reported as the domain 1 twinning plane from which the second-order twins were generated. The parent orientation was also taken to be a perfect twin of domain 1 since that twin itself was not observed. The deviations from perfect twinning orientations range from approximately 0.1 to 0.3°, in agreement with results reported by Varlioglu et al.[86] This misorientation may be caused by strain at the domain walls, or local breaking of the symmetry from the ideal tetragonal structure [34].

Table 4.3: Domain-scale parameters for grain D in the as-processed state (F0) and at high field (F2). Misorientation from perfect twinning is calculated relative to orientations generated taking domain 1 parameters as the parent. Starting lattice parameters: $a = b = 4.0042$Å, $c = 4.0472$ Å, $\alpha = \beta = \gamma = 90°$. Cell volume = 64.8905 Å^3.

	ID	parent	ϕ_{100} (°)	twin plane	mis. from perfect twin (°)	a (Å)	b (Å)	c (Å)	α (°)	β (°)	γ (°)	volume (Å^3)
F0	1	parent	31.26	-	-	4.0039	4.0040	4.0469	90.0401	89.9918	89.9989	64.878
	2	1	61.71	$(\bar{1}01)$	0.1534	4.0049	4.0052	4.0462	89.9789	89.9986	90.0201	64.901
	3	1	78.43	(011)	0.1100	4.0034	4.0046	4.0469	89.9947	90.0063	90.0356	64.880
	4	1	79.20	$(0\bar{1}1)$	0.2846	4.0025	4.0052	4.0479	90.0001	90.0241	89.9617	64.892
	5	(101)	79.01	(011)	0.2606	4.0046	4.0045	4.0461	89.9759	89.9797	90.0259	64.885
	6	(101)	78.63	$(0\bar{1}1)$	0.2602	4.0022	4.0055	4.0476	90.0345	89.9754	90.0035	64.886
F2	1	parent	31.17	-	-	4.0033	4.0021	4.0482	90.0109	89.9911	90.0351	64.859
	2	1	61.80	$(\bar{1}01)$	0.1941	4.0051	4.0029	4.0472	89.9928	90.0459	90.0450	64.883
	3	1	78.25	(011)	0.1158	4.0042	4.0044	4.0470	90.0282	89.9769	90.0017	64.891

The evolution of domain volume fractions in grain D is shown in Figure 4.13 where the c-axis misorientations are 62.1°, 78.3°, and 30.7° for domain variants d_{200}, d_{020}, and $d_0 02$, respectively. At F0, d_{020} is the result of contributions from domains 3 to 6 in Table 4.3. At F2, it consists of a single domain, domain 3. Since the volume fraction of d_{002} is nearly constant and the volume fraction of d_{200} is decreased, it makes sense that domains 4 to 6 are consolidated with domain 3 into a single variant. At field step F2, the refined parameters for domain 3, the domain which has grown, are much closer to those of the starting crystal parameters ($a = b = 4.0042$ Å, $c = 4.0472$ Å, $\alpha = \beta = \gamma = 90°$. Cell volume = 64.8905 Å^3). This may indicate that domain switching has the effect of stress relief, however, we require an estimate of error to determine whether this is significant and results from many grains for a statistical analysis.

4.4 Conclusions and Perspectives

The work presented here has demonstrated that diffraction peaks originating from individual ferroelastic domains can be identified and indexed by comparison with a forward projection model assuming crystallographic twins. The examination of diffraction spots from bulk grains has revealed a complex and heterogeneous domain structure at the grain scale with some grains exhibiting typical twinning structure and others appearing to be under high strain, composed of several coherently diffracting domains that do not fit a twinning model. Such structures must be the result of a heterogeneous local environment at the cubic to tetragonal transition point. When subjected to an externally applied electric field, there is a reduction in the number of domain walls and the domains tend to consolidate into broad regions more reminiscent of the lamellar and herringbone twinning patterns observed optically. The domains do not, however, exhibit a perfect twinning orientation, as was noted in a previous study by Varlioglu et al[86]. The results presented here agree with the finding that the domains are misoriented by 0.1 to 0.3° as compared with the misorientation expected for perfect twins. In this study, additional double twin variants were identified, again suggesting a highly complex microstructure in the as-processed state. These variants mostly disappear with the applied electric field due to domain wall motion and polarization switching. However, the domains are still found to be misoriented relative to a perfect twinning crystallography.

With the implementation of an improved assignment scheme and additional detector corrections, the domain-scale parameters can be extracted for a statistically significant number of grains embedded in the bulk of the sample. Combining this with the grain-scale information obtained from the analysis in Chapter 3 will enable us to examine the extent to which the inhomogeneous ferroelastic switching strains observed in Chapter 3 are accomodated by elastic compliance strains in neighbour grains. Additionally, a full refinement of lattice parameters will reveal local effects such as back stresses and strain accommodation at the intergranular level and the role that intergranular effects play in the grain-scale response.

Chapter 5

Conclusions

The work presented in this thesis has been undertaken with two main goals: (i) contribution to the body of knowledge of piezoceramics and (ii) development new experimental techniques for studying multi-domain materials. The study of polycrystalline materials must consider the totality of processes occuring at all length scales that give rise to the macroscopic response. It is important to study these processes in the context of real contraint and boundary conditions. In the case of coarse-grained materials, this means studying grains embedded in the bulk of the sample, in their three-dimensional environments and surrounded by their real grain neighbourhoods. Such studies are difficult to undertake by traditional techniques such as microscopy, which is destructive and two-dimensional, and powder diffraction, in which the grain-to-grain effects are averaged out. We have presented a comprehensive study of a prototypical ferroelectric using a combination of 3DXRD techniques, applying novel data analysis techniques to extract grain and domain-scale information.

In the first method, the domains are grouped into three variants based on their c-axis orientation, one c-axis along each of the original cubic axes. From the intensity ratios of (202)/(002) diffraction peaks split in 2θ, the domain volume fractions and resulting non-180° switching strains were calculated for 139 grains in the as-processed state, at an applied electric field near the coercive field, and at a high field strength. The results were combined with a three-dimensional space-filling grain map reconstructed from nearfield 3DXRD, generating a multi-dimensional data set from which the grain response could be examined in the context of its local neighbourhood. The results indicate that the as-processed state of the material is highly heterogeneous, with unequal volume fractions of each of the three domain types. The extrinsic strain response

shows a first-order dependence on grain orientation, as expected, however, there are large second order deviations from the trend. Grains of similar size and orientation were found to exhibit significantly different responses to an applied field. We attribute both of these effects to a heterogeneous grain neighbourhood, both at the phase transition and within the resulting microstructure. Initial results also indicate that the effect may be more localized than the grain-to-grain scale, as there was no immediate correlation of the response with microstructural features such as individual grain size, neighbour grain misorientation, or number of neighbours.

On a more localized level, we examined the intensity originating from individually diffracting structures. From simple observation, it is clear that the domain structure in the as-processed state can extremely complex, consisting of many domains that do not fit the expected twinning orientation relationship. This suggests that each grain experiences a unique localized state at the transition from cubic to tetragonal that cannot be accounted for by the domain volume fraction alone. To study this quantitatively, we developed a novel technique whereby the diffracted intensity originating from individual domain variants was located by forward projection of the diffraction pattern. By precise determination of local maxima within the data set, we were able to resolve the individually diffracting domain structures. The parameters were refined by minimising the deviation between the projected and measured diffraction pattern. The results suggest a strained microsctructure where the domains are misorientated from perfect twins by roughly 0.1-0.3°, which agrees with previous results obtained by 3DXRD. Upon implementation of some additional features, such as assignment of domains by shape matching rather than simple distance criteria, the domain-scale parameters can be refined for a statistically significant number of grains in an automated fashion. This will provide opportunities to study the extent to which the grain neighbourhood must accommodate heterogeneous ferroelastic strains by elastic compliance, and the effect of such localized strains on, for example, the local symmetry of the material.

Overall, this work presents a concerted effort to obtain a comprehensive, three-dimensional data set for a statistically relevant sample. With continued development of the indexing algorithm, we hope to reveal the coupling of processes at multiple length scales and their impact on the overall mechanical response of the sample. Such information will help guide the development of processing techniques, suitable lead-free materials compositions, and domain engineering efforts. We would also like to stress the suitability of such a data set for model input and validation. Modelling and simulations can provide great insight into processes occuring at length scales that are not accessible to these techniques and difficult to study with statistical significance. Such integrated experimental and modelling efforts represent a modern materials science approach that can help us develop new materials, faster and more efficiently, providing benefits to our health, the environment, and the economy.

Bibliography

[1] S.B. Lang. *Sourcebook of Pyroelectricity*. Ferroelectrics and related phenomena. Gordon and Breach Science Publishers, 1974.

[2] Sir David Brewster. *Observations on the pyro-electricity of minerals*. William Blackwood, 1824.

[3] pyroelectricity. IUCr Online Dictionary of Crystallography. `http://reference.iucr.org/dictionary/Pyroelectricity`. [Online; accessed 03.01.2016].

[4] Sidney B Lang. Pyroelectricity: From ancient curiosity to modern imaging tool. *Physics Today*, 58(August):31–36, 2005.

[5] Jacques Curie and Pierre Curie. Développement, par pression, de l'électricité polaire dans les cristaux hémièdres à faces inclinées. *Comptes-Rendus de l'Académie des Sciences*, 91(2):294–295, 1880.

[6] G Lippmann. Principe de la conservation de l'electricitea ou second principe de la theorie des phenoménes electriques. *J. de Phys.*, 10:381–394, 1881.

[7] Pierre Curie and Jacques Curie. Contractions et dilatations produites par des tensions électriques dans les cristaux hémièdres à faces inclinées. *Comptes-Rendus de l'Académie des Sciences*, 93:1137–1140, 1881.

[8] piezoelectricity. IUCr Online Dictionary of Crystallography. `http://reference.iucr.org/dictionary/Pyroelectricity`. [Online; accessed 03.01.2016].

[9] Walter G. Cady. Piezoelectricity and Ultrasonics. *Sound: Its Uses and Control*, 2(1):46, 1963.

[10] L E Cross and R E Newnham. History of Ferroelectrics. *Ceramics and Civilization*, III:289–305, 1987.

[11] J. Valasek. Piezo-electric and allied phenomena in Rochelle salt. *Physical Review*, 17(4):475–481, 1921.

[12] Hans von R. Jaffe. Polymorphism of Rochelle Salt. *Physical Review*, 51(1):43–47, 1937.

[13] Joseph Valasek. Piezo-Electric Activity of Rochelle Salt under Various Conditions. *Physical Review*, 19(5):478–491, 1922.

[14] ferroics. IUCr Online Dictionary of Crystallography. `http://reference.iucr.org/dictionary/Pyroelectricity`. [Online; accessed 03.01.2016].

[15] Veerle Keppens. 'Ferroelectricity' in a metal. *Nature Materials*, 12(November):952–3, 2013.

[16] G Busch and P Scherrer. Eine neue seignette-elektrische Substanz. *Naturwissenschaften*, 23:737, 1935.

[17] H. Thurnauer. Ceramic material made of magnesium titanate and method of preparing the same, December 15 1942. US Patent 2,305,327.

[18] H. Thurnauer and J. Deaderick. Insulating material, October 21 1947. US Patent 2,429,588.

[19] E Wainer and Aa N Salomon. Titanium alloy manufacturing co. *Electr. Rep*, 8(9):1943, 1942.

[20] Eugene Wainer. High Titania Dielectrics. *Transactions of The Electrochemical Society*, 89(1):331–356, 1946.

[21] S Ogawa. On polymorphic change of barium titanate. *J Phys Soc Jpn*, 1:32–33, 1946.

[22] BM Wul and IM Goldman. Dielectric constants of titanates of metals of the second group. *Compt. rend. Acad. sci. URSS*, 46:139–42, 1945.

[23] A Von Hippel, R G Breckenridge, F G Chesley, and Laszlo Tisza. High dielectric constant ceramics. *Industrial Engineering Chemistry*, 38(11):1097–1109, 1946.

[24] H. BLATTNER, B. MATTHIAS, and Al Et. Untersuchungen an Bariumtitanat-Einkristallen. *Experientia*, 3(4):148, 1947.

[25] B T Matthias and A Von Hippel. Domain Structure and Dielectric Response of Barium Titanate Single Crystals*. *Physical Review*, 73(11), 1948.

[26] A. Von Hippel. Ferroelectricity, domain structure, and phase transitions of barium titanate. *Reviews of Modern Physics*, 22(3):221–237, 1950.

[27] G. Arlt. Twinning in ferroelectric and ferroelastic ceramics: stress relief. *Journal of Materials Science*, 25:2655–2666, 1990.

[28] Q. M. Zhang, H. Wang, N. Kim, and L. E. Cross. Direct evaluation of domain-wall and intrinsic contributions to the dielectric and piezoelectric response and their temperature dependence on lead zirconate-titanate ceramics. *Journal of Applied Physics*, 75(1):454–459, 1994.

[29] Dragan Damjanovic and Marlyse Demartin. Contribution of the irreversible displacement of domain walls to the piezoelectric effect in barium titanate and lead zirconate titanate ceramics. *Journal of Physics: Condensed Matter*, 9(23):4943–4953, 1999.

[30] Abhijit Pramanick, Anderson D. Prewitt, Jennifer S. Forrester, and Jacob L. Jones. Domains, Domain Walls and Defects in Perovskite Ferroelectric Oxides: A Review of Present Understanding and Recent Contributions. *Critical Reviews in Solid State and Materials Sciences*, 37(4):243–275, dec 2012.

[31] Yongqiang Tan, Jialiang Zhang, Yanqing Wu, Chunlei Wang, Vladimir Koval, Baogui Shi, Haitao Ye, Ruth McKinnon, Giuseppe Viola, and Haixue Yan. Unfolding grain size effects in barium titanate ferroelectric ceramics. *Scientific Reports*, 5:9953, 2015.

[32] Yachin Ivry, Daping Chu, James F. Scott, and Colm Durkan. Domains Beyond the Grain Boundary. *Advanced Functional Materials*, 21(10):1827–1832, may 2011.

[33] Robert C. Rogan, Ersan Üstündag, Bjørn Clausen, and Mark R. Daymond. Texture and strain analysis of the ferroelastic behavior of Pb(Zr,Ti)O3 by in situ neutron diffraction. *Journal of Applied Physics*, 93(7):4104, 2003.

[34] Alberto Biancoli, Chris M. Fancher, Jacob L. Jones, and Dragan Damjanovic. Breaking of macroscopic centric symmetry in paraelectric phases of ferroelectric materials and implications for flexoelectricity. *Nature Materials*, 14(2):224–229, 2014.

[35] John E. Daniels, Trevor R. Finlayson, Andrew J. Studer, Mark Hoffman, and Jacob L. Jones. Time-resolved diffraction measurements of electric-field-induced strain in tetragonal lead zirconate titanate. *Journal of Applied Physics*, 101(9):094104, 2007.

[36] Robert B. Gray. Transducer and method of making the same, November 1 1949. US Patent 2,486,560.

[37] Gen Shirane, Kazuo Suzuki, and Akitsu Takeda. Phase transitions in solid solutions of pbzro3 and pbtio3 (ii) x-ray study. *Journal of the Physical Society of Japan*, 7(1):12–18, 1952.

[38] Gen Shirane and Kazuo Suzuki. Crystal structure of pb(zr-ti)o3. *Journal of the Physical Society of Japan*, 7(3):333–333, 1952.

[39] B. Jaffe, R. S. Roth, and S. Marzullo. Piezoelectric properties of Lead zirconate-Lead titanate solid-solution ceramics [8], 1954.

[40] B. Jaffe. Piezoelectric transducers using lead titanate and lead zirconate, May 10 1955. US Patent 2,708,244.

[41] Dragan Damjanovic. *Hysteresis in piezoelectric and ferroelectric materials*, volume 3. 2006.

[42] William R. Cook Bernard Jaffe and Jans Jaffe. *Piezoelectric Ceramics*. Academic Press Inc., New York, 1971.

[43] L. D. Landau. On the theory of phase transitions. *Zh. Eks. Teor. Fiz.*, 7(1937):19–32, 1937.

[44] V L Ginzburg. Phase Transitions in Ferroelectrics. In *Ferroelectricity: The Fundamentals Collection*, pages 130–136. 2005.

[45] Robert W. Cahn. *Concise encyclopedia of materials characterization*, pages 489–491. Elsevier, 2005.

[46] Nele Moelans, Bart Blanpain, and Patrick Wollants. An introduction to phase-field modeling of microstructure evolution. 32:268–294, 2008.

[47] S.C. Hwang, C.S. Lynch, and R.M. McMeeking. Ferroelectric/ferroelastic interactions and a polarization switching model. *Acta Metallurgica et Materialia*, 43(5):2073–2084, 1995.

[48] J. D. Eshelby. The Determination of the Elastic Field of an Ellipsoidal Inclusion, and Related Problems. *Proceedings of the Royal Society A: Mathematical, Physical and Engineering Sciences*, 241(1226):376–396, 1957.

[49] M.L. Dunn and M. Taya. Micromechanics predictions of the effective electroelastic moduli of piezoelectric composites. *International Journal of Solids and Structures*, 30(2):161–175, 1993.

[50] J. E. Huber, N. a. Fleck, C. M. Landis, and R. M. McMeeking. Constitutive model for ferroelectric polycrystals. *Journal of the Mechanics and Physics of Solids*, 47(8):1663–1697, 1999.

[51] Anja Haug, John E. Huber, Patrick R. Onck, and Erik Van der Giessen. Multigrain analysis versus self-consistent estimates of ferroelectric polycrystals. *Journal of the Mechanics and Physics of Solids*, 55(3):648–665, 2007.

[52] Hamidreza Abdolvand, Marta Majkut, Jette Oddershede, Søren Schmidt, Ulrich Lienert, Bradley J. Diak, Philip J. Withers, and Mark R. Daymond. On the deformation twinning of Mg AZ31B: A three-dimensional synchrotron X-ray diffraction experiment and crystal plasticity finite element model. *International Journal of Plasticity*, 70:77–97, 2015.

[53] Hamidreza Abdolvand, Marta Majkut, Jette Oddershede, Jonathan P. Wright, and Mark R. Daymond. Study of 3-D stress development in parent and twin pairs of a hexagonal close-packed polycrystal: Part II – crystal plasticity finite element modeling. *Acta Materialia*, 93:235–245, 2015.

[54] Hamidreza Abdolvand, Marta Majkut, Jette Oddershede, Jonathan P. Wright, and Mark R. Daymond. Study of 3-D stress development in parent and twin pairs of a hexagonal close-packed polycrystal: Part I – in-situ three-dimensional synchrotron X-ray diffraction measurement. *Acta Materialia*, 93:246–255, 2015.

[55] Yasuyoshi Saito, Hisaaki Takao, Toshihiko Tani, Tatsuhiko Nonoyama, Kazumasa Takatori, Takahiko Homma, Toshiatsu Nagaya, and Masaya Nakamura. Lead-free piezoceramics. *Nature*, 432(November):1–4, 2004.

[56] Jürgen Rödel, Kyle G. Webber, Robert Dittmer, Wook Jo, Masahiko Kimura, and Dragan Damjanovic. Transferring lead-free piezoelectric ceramics into application. *Journal of the European Ceramic Society*, 35(6):1659–1681, 2015.

[57] Tom Kalil and Cyrus Wadia. Materials Genome Initiative for Global Competitiveness. Technical Report June, 2011.

[58] SC Glotzer, S Kim, and PT Cummings. International assessment of research and development in simulation-based engineering and science. *Zitiert auf*, 2010.

[59] The Minerals Metals & Materials Society (TMS). *Modeling Across Scales: A Roadmapping Study for Connecting Materials Models and Simulations Across Length and Time Scales*. 2015.

[60] D. Juul Jensen and H.F. Poulsen. The three dimensional X-ray diffraction technique. *Materials Characterization*, 72:1–7, oct 2012.

[61] Jette Oddershede, Bettina Camin, Søren Schmidt, Lars P. Mikkelsen, Henning Osholm Sørensen, Ulrich Lienert, Henning Friis Poulsen, and Walter Reimers. Measuring the stress field around an evolving crack in tensile deformed Mg AZ31 using three-dimensional X-ray diffraction. *Acta Materialia*, 60(8):3570–3580, may 2012.

[62] R Baruzzo and A Stevanato. Laue–Laue monochromator for ID11 beamline at ESRF. ... *Physics Research A*, pages 2–4.

[63] Søren Schmidt. GrainSpotter: A fast and robust polycrystalline indexing algorithm. *Journal of Applied Crystallography*, 47(1):276–284, 2014.

[64] U. L. Olsen, S. Schmidt, and H. F. Poulsen. A high-spatial-resolution three-dimensional detector array for 30-200 keV X-rays based on structured scintillators. *Journal of Synchrotron Radiation*, 15(4):363–370, 2008.

[65] Jean Claude Labiche, Olivier Mathon, Sakura Pascarelli, Mark A. Newton, Gemma Guilera Ferre, Caroline Curfs, Gavin Vaughan, Alejandro Homs, and David Fernandez Carreiras. Invited article: The fast readout low noise camera as a versatile x-ray detector for time resolved dispersive extended x-ray absorption fine structure and diffraction studies of dynamic problems in materials science, chemistry, and catalysis. *Review of Scientific Instruments*, 78(9), 2007.

[66] Henning O. Sørensen, Søren Schmidt, Jonathan P. Wright, Gavin B. M. Vaughan, Simone Techert, Elspeth F. Garman, Jette Oddershede, Jav Davaasambuu, Karthik S. Paithankar, Carsten Gundlach, and Henning F. Poulsen. Multigrain crystallography. *Zeitschrift für Kristallographie*, 227(1):63–78, jan 2012.

[67] S. Schmidt, U. L. Olsen, H. F. Poulsen, H. O. Sørensen, E. M. Lauridsen, L. Margulies, C. Maurice, and D. Juul Jensen. Direct observation of 3-D grain growth in Al-0.1% Mn. *Scripta Materialia*, 59(5):491–494, 2008.

[68] J K Mackenzie. Second paper on statistics associated with the random distribution of cubes. *Biometrika*, 45(1-2):229–240, 1958.

[69] Jette Oddershede, Marta Majkut, Qinghua Cao, Søren Schmidt, Jonathan P. Wright, Peter Kenesei, and John E. Daniels. Quantitative grain-scale ferroic domain volume fractions and domain switching strains from three-dimensional X-ray diffraction data. *Journal of Applied Crystallography*, 48(3):882–889, 2015.

[70] John E Daniels, Marta Majkut, Qingua Cao, Søren Schmidt, Jonathan P Wright, and Jette Oddershede. Heterogeneous grain-scale response in ferroic polycrystals under electric field. *Scientific Reports, accepted*, 2016.

[71] Michael a Groeber and Michael a Jackson. DREAM.3D: A Digital Representation Environment for the Analysis of Microstructure in 3D. *Integrating Materials and Manufacturing Innovation*, 3(1):5, 2014.

[72] Utkarsh Ayachit. *The ParaView Guide: A Parallel Visualization Application*. Kitware, 2015.

[73] Abhijit Pramanick, Dragan Damjanovic, John E Daniels, Juan C Nino, and Jacob L Jones. Origins of Electro-Mechanical Coupling in Polycrystalline Ferroelectrics During Subcoercive Electrical Loading. *Journal of the American Ceramics Society*, 94(2):293–309, 2011.

[74] M. J. Hoffmann, M. Hammer, a. Endriss, and D. C. Lupascu. Correlation between microstructure, strain behavior, and acoustic emission of soft PZT ceramics. *Acta Materialia*, 49(7):1301–1310, 2001.

[75] G. Tutuncu, M. Motahari, M. R. Daymond, and E. Üstündag. A modified Rietveld method to model highly anisotropic ceramics. *Acta Materialia*, 60(4):1494–1502, 2012.

[76] S. Choudhury, Y. L. Li, C. Krill, and L. Q. Chen. Effect of grain orientation and grain size on ferroelectric domain switching and evolution: Phase field simulations. *Acta Materialia*, 55(4):1415–1426, 2007.

[77] Yulan Li, S. Y. Hu, Z. K. Liu, and L. Q. Chen. Effect of electrical boundary conditions on ferroelectric domain structures in thin films. *Applied Physics Letters*, 81(3):427–429, 2002.

[78] Frank Ernst, Maureen L Mulvihill, Oliver Kienzle, and Manfred Rühle. Preferred Grain Orientation Relationships in Sintered Perovskite Ceramics. *Journal of the American Ceramic Society*, 84(8):1885–1890, 2001.

[79] S Tsurekawa, K Ibaraki, K Kawahara, and T Watanabe. The continuity of ferroelectric domains at grain boundaries in lead zirconate titanate. *Scripta Materialia*, 56(7):577–580, 2007.

[80] L Daniel, D A Hall, and P J Withers. A multiscale model for reversible ferroelectric behaviour of polycrystalline ceramics. *Mechanics of Materials*, 71:85–100, 2014.

[81] J E Daniels, J L Jones, and T R Finlayson. Characterization of domain structures from diffraction profiles in tetragonal ferroelastic ceramics. *Journal of Physics D: Applied Physics*, 39(24):5294–5299, 2006.

[82] H Simons, A King, W Ludwig, C Detlefs, W Pantleon, S Schmidt, I Snigireva, A Snigirev, and H F Poulsen. Dark-field X-ray microscopy for multiscale structural characterization. *Nature Communications*, 6:6098–6103, 2015.

[83] Marc Kamlah, Albrecht C. Liskowsky, Robert M. McMeeking, and Herbert Balke. Finite element simulation of a polycrystalline ferroelectric based on a multidomain single crystal switching model. *International Journal of Solids and Structures*, 42(9-10):2949–2964, 2005.

[84] Anja Haug, Patrick R. Onck, and Erik Van der Giessen. Development of inter- and intragranular stresses during switching of ferroelectric polycrystals. *International Journal of Solids and Structures*, 44(6):2066–2078, 2007.

[85] A. Staroselsky and L. Anand. A constitutive model for hcp materials deforming by slip and twinning. *International Journal of Plasticity*, 19(10):1843–1864, 2003.

[86] Mesut Varlioglu, Ulrich Lienert, Jun-Sang Park, Jacob L. Jones, and Ersan Üstündag. Thermal and Electric Field-Dependent Evolution of Domain Structures in Polycrystalline BaTiO3 Using the 3D-XRD Technique. *Texture, Stress, and Microstructure*, 2010(1):1–10, 2010.

[87] Tom T. a. Lummen, Yijia Gu, Jianjun Wang, Shiming Lei, Fei Xue, Amit Kumar, Andrew T. Barnes, Eftihia Barnes, Sava Denev, Alex Belianinov, Martin Holt, Anna N. Morozovska, Sergei V. Kalinin, Long-Qing Chen, and Venkatraman Gopalan. Thermotropic phase boundaries in classic ferroelectrics. *Nature communications*, 5:3172, 2014.

Included Papers

Paper I: Grain-scale domain orientations and lattice parameters in a bulk barium titanate ceramicmeasured by three-dimensional X-ray diffraction (*Abstract*)

Marta Majkut, Jette Oddershede, John E Daniels, Jonathan P Wright, Søren Schmidt

Grain-scale domain orientations and lattice parameters in a bulk barium titanate ceramic measured by three-dimensional X-ray diffraction

Marta Majkut Jette Oddershede John E. Daniels
Jonathan Wright Søren Schmidt

March 29, 2016

Abstract

Domain wall motion is a large contributor to the total response of piezoceramics. The domain structure is formed during a spontaneous transformation at the Curie temperature from a higher symmetry phase to a lower symmetry phase, in the case of the barium titanate sample considered here, cubic to tetragonal. The resulting microstructure is complex and highly heterogeneous. These heterogeneities must be accommodated by compliance strains at the grain scale, and which may either enhance or inhibit the motion of domain walls. It is important to study such effects in grains under real three-dimensional constraint, although such information is difficult to obtain by traditional techniques. Three-dimensional X-ray diffraction provides a method for studying individual grains in a bulk sample, but so far indexing and refinement of grain-scale parameters has been limited to single domains and some twins. We present here an indexing and refinement procedure for the multi-domain case, relying on forward projection of expected domain orientations and minimization between the predicted and measured diffraction patterns. The domains are automatically assigned and indexed, and domain orientations and lattice parameters refined for a statistically significant number of grains. Results are discussed with respect to grain orientation and grain neighbourhood, in combination with a three-dimensional space-filling grain map.

Paper II: Ferroic Material Response Resolved at the Grain-Scale (*Submitted*)

Marta Majkut, John E Daniels, Jonathan P Wright, Søren Schmidt, Jette Oddershede

Elsevier Editorial System(tm) for Acta Materialia

Manuscript Draft

Manuscript Number:

Title: Ferroic Material Response Resolved at the Grain-Scale

Article Type: Full length article

Keywords: Ferroelastic; Ferroelectric; Grain interaction; High-energy X-ray diffraction; Strain distribution

Corresponding Author: Mrs. Jette Oddershede, Ph.D.

Corresponding Author's Institution: Technical University of Denmark

First Author: Marta Majkut

Order of Authors: Marta Majkut; John E Daniels, Ph.D.; Jonathan P Wright, Ph.D.; Søren Schmidt, Ph.D.; Jette Oddershede, Ph.D.

Abstract: Functional ferroics are critical components in many modern devices. Polycrystalline states of these materials dominate the market due to their cost effectiveness and ease of production. Studying the coupling of ferroic properties across grain boundaries and within clusters of grains is therefore critical for understanding bulk polycrystalline ferroic behavior. Here, three-dimensional X-ray diffraction is used to reconstruct a 3D grain map of a polycrystalline barium titanate sample and resolve the grain-scale non-180° ferroelectric domain switching strains as a function of applied electrical field. While the strain response of a grain is found to depend primarily on its crystallographic orientation relative to the field direction, there are large grain-scale deviations from the average behavior. No significant correlations are found between the response of individual grains and microstructural factors such as grain size or number of neighbors. Results suggest that each grain is located in a very unique local environment in terms of intergranular misorientations, and this affects the local strain heterogeneity even in the as-processed state of the sample. These results provide unique insight into the grain-scale interactions of ferroics, and will contribute to future design and modeling of these and related materials.

Suggested Reviewers: Satoshi Wada
University of Yamanashi
swada@yamanashi.ac.jp
Guru of ferroelectrics

Marek Faryna
Polish Academy of Sciences
m.faryna@imim.pl
Extensive experience with characterisation of 3D microstructures

Guorong Li
Shanghai Institute of Ceramics
grli@sunm.shcnc.ac.cn
Ceramicist who's done a lot of work with ferroelectrics

Laurent Daniel
Univ Paris-Sud
laurent.daniel@u-psud.fr
Works with constitutive laws for coupled phenomena

Cover Letter

DTU Physics

Editors of Acta Materialia

February 4th, 2016

Dear Editors,

Please consider the attached manuscript entitled “Ferroic Material Response at the Grain-Scale” for publication in Acta Materialia.

In a 2015 report by The Mineral, Metals and Materials Society on the future of multi-scale modelling efforts [1], experimental verification of material response at the grain-scale is consistently highlighted as a difficulty for advance. We agree this is true, and aim in the enclosed manuscript to provide experimental investigations of the grain-scale response of functional ferroic materials. As stated in the paper, the approach is by no means limited to ferroelectric systems, but can be applied to analogous materials such as superelastics and shape memory alloys (magnetic or not).

We have shown in this work that the response of the system is highly heterogeneous at the grain-scale, both in the as-processed state of the sample and after electrical loading. By applying the 3D-XRD method to obtain a 3D grain map in combination with our recently developed method for incorporating domain texture strains [2], we have quantified the grain-scale heterogeneity directly, and for the first time compared with local grain environment information. The results may serve directly as input for modelling efforts of the ferroic material response at the grain-scale, and in particular lead to an enhanced understanding of the speculated coupling of ferroic properties across grain boundaries.

All authors have read the manuscript and agree to its publication. We hope that the manuscript can be accepted for publication and kindly request that both Jette Oddershede and Søren Schmidt (ssch@fysik.dtu.dk) are listed as corresponding authors.

On behalf of the authors,

Jette Oddershede

[1] www.tms.org/multiscalestudy, Modeling Across Scales: A Roadmapping Study for Connecting Materials Models and Simulations Across Length and Time Scales, (2015).

[2] J. Oddershede, M. Majkut, Q. Cao, S. Schmidt, J.P. Wright, P. Kenesei, et al., Quantitative grain-scale ferroic domain volume fractions and domain switching strains from three-dimensional X-ray diffraction data, J. Appl. Crystallogr. 48 (2015) 882–889. doi:10.1107/S1600576715007669.

Technical University of Denmark
Department of Physics
Fysikvej
Building 307
DK-2800 Kgs. Lyngby
Denmark
Tlf. +45 23 71 23 31
Fax +45 45 93 23 99
jeto@fysik.dtu.dk
www.fysik.dtu.dk

Ferroic Material Response Resolved at the Grain-Scale

Marta Majkut,[a] John E. Daniels,[b] Jonathan P. Wright,[c] Søren Schmidt[a,*], Jette Oddershede [a,*]

[a]Department of Physics, Technical University of Denmark, Fysikvej, 2800 Kgs. Lyngby, Denmark

[b]School of Materials Science and Engineering, UNSW Australia, Sydney NSW 2052, Australia

[c]European Synchrotron Radiation Facility, Grenoble 38000, France

ssch@fysik.dtu.dk, +45 2132 9305

jeto@fysik.dtu.dk, +45 2371 2331

Keywords: Ferroelastic; Ferroelectric; Grain interaction; High-energy X-ray diffraction;

Strain distribution

Abstract

Functional ferroics are critical components in many modern devices. Polycrystalline states of these materials dominate the market due to their cost effectiveness and ease of production. Studying the coupling of ferroic properties across grain boundaries and within clusters of grains is therefore critical for understanding bulk polycrystalline ferroic behavior. Here, three-dimensional X-ray diffraction is used to reconstruct a 3D grain map of a polycrystalline barium titanate sample and resolve the grain-scale non-180° ferroelectric domain switching strains as a function of applied electrical field. While the strain response of a grain is found to depend primarily on its crystallographic orientation relative to the field direction, there are large grain-scale deviations from the average behavior. No significant correlations are found between the response of individual grains and microstructural factors such as grain size or number of neighbors. Results suggest that each grain is located in a very unique local environment in terms of intergranular misorientations, and this affects the local strain heterogeneity even in the as-processed state of the sample. These results provide unique insight into the grain-scale interactions of ferroics, and will contribute to future design and modeling of these and related materials.

1 Introduction

Many functional devices make use of the ferroic nature of their constituent materials. Ferroelctriciy, ferromagnetism, and ferroelasticity, and the coupling between them are optimized for example in advanced memory devices [1] and high strain actuation [2]. In the case of piezoelectric materials, which directly couple electrical and mechanical energies, the movement of ferroelectric domains results in a large materials response. Within this material class lead zirconate titanate (PZT)-based ceramics are prevalent in industry, primarily due to the combination of large piezoelectric coefficients and favorable temperature stability. The recent push towards lead-free materials [3,4] has not only led to the discovery of many new high performance piezoelectric ceramics, but has also invigorated studies into the fundamental nature of electro-mechanical coupling. Of particular interest in ceramic polycrystals are the micro- and meso-scale phenomena occurring at the domain and grain length-scales that drive the material response. This fundamental knowledge may be used to guide the design and development of future alternative electro-mechanical materials.

Barium titanate (BT) is a prototypical perovskite piezoelectric material. It is readily produced in ceramic form and is commonly used as an end-member component of many disordered perovskites identified as potential high-performance lead-free piezoelectrics [5–11]. On cooling BT through the Curie temperature, T_C, of roughly 130°C, the high-temperature paraelectric cubic phase transforms to a ferroelectric tetragonal phase. The transition occurs when a charged atom moves away from a center of symmetry, resulting in an electrical polarization and an elongation of the unit cell along one of the original cubic <001> axes. This results in six possible tetragonal domain variants ($\pm x$, $\pm y$, $\pm z$). These domains are regions of common ferroelectric polarization and are separated from adjacent regions with differing polarization by domain walls of either 180° for antiparallel directions or ~90° in the case of tetragonal materials. The domains form such that the total energy of the system (e.g.,

elastic, electrical, etc.) is minimized, resulting in complex microstructures across many length scales [12,13]. For example, the size of individual domains depends on the domain wall energy, thus, the nature and type of domain walls is of importance. The microstructural complexity may also affect the crystallographic orientation relationship between domains. Tetragonal domains are commonly thought of as twins on the {101} family of planes, however, the twinning model predicts a misorientation of 89.47°, which does not account for the misorientations previously measured in a bulk BT grain [14].

In the as-processed state, the net macroscopic polarization of a BT ceramic is zero, however, when an external electric field is applied, the domain walls move and the domain volume fractions within the grains evolve, resulting in a net macroscopic polarization. During this process, due to the coupling of the ferroelectric domains with the ferroelastic unit cell distortion, a remnant strain will result. Similar strain generation processes occur during actuation of the electrically poled ceramic, however, the mechanism is complicated in polycrystalline materials where neighboring grains with different orientations must deform together. This introduces inhomogeneity and intergranular stresses, as has been observed for many polycrystalline materials [15,16]. Additionally, it is regularly observed in ceramic materials that domain structures interact across grain boundaries, leading to the possibility of longer range coupling of domain responses [17].

Traditional methods such as powder diffraction [2,18–20] have revealed information on the bulk-averaged strain behavior, in particular the orientation dependence of the material response has been extensively studied for ensembles of similarly oriented grains. Optical [21] and electron [22] microscopy and scanning probe techniques [23–26] provide more local information on grain and domain morphology, but these techniques are destructive and give only two-dimensional information at a stress-relieved surface. As such, the combination of all these methods for observing strain and domain behavior have not yet sufficiently described

the effect of grain neighbor relations on the strain response at the desired length scale of the individual grains. For example, there may be neighboring grain orientations that prevent the growth of favorably oriented domains, or special misorientations between neighboring grains that enhance coupling of domain wall motion across grain boundaries [17]. These factors may affect not only the magnitude of response of the material, but also the reliability and fatigue properties as cracking and delamination generally initiate at heterogeneities such as grain boundaries where localized stresses and structural mismatches are high.

Here, the electric field induced changes in BT are presented, whereby a full 3D grain map including the individual grain orientations and domain volume fractions is extracted from three-dimensional X-ray diffraction (3DXRD) data. This technique has been previously used to study, for example, grain growth in aluminum [27,28] and deformation twinning in magnesium [29,30], titanium [31,32] and zirconium alloys [33,34], and was recently expanded to study the multiple domain case [35]. The volume fraction evolution of domains and the associated non-180° domain switching strain is tracked from the initial sintered state to an applied electric field larger than the ferroelectric coercive field, E_C. The observed variations in the domain volume fractions in individual grains, in the initial state and after the application of a electrical field, are analyzed in detail for 139 grains of BT. This includes separating out the overall orientation dependence of the electric field induced response at the grain-scale, and quantifying the second order effects that can only be explained by the differences in the local environments of the individual grains. The unique set of data presented here is explored to determine how factors such as grain size, neighborhood characteristics, and location within the sample (surface or bulk) affect the material response at the grain-scale. Finally, local microstructural features such as grain neighbor misorientations are extracted for selected bulk grains of similar orientation and size, and it is discussed how

this information may serve as input and inspiration for future modeling attempts when moving from idealized towards real polycrystalline materials.

2 Experimental

2.1 Sample preparation

Barium titanate ceramic was prepared with a grain size of approximately 50-70 μm and cut and polished into a cuboid sample of dimensions 300×300×400 μm^3. The sample was mounted in a setup that allows application of a high electrical field with minimal risk of dielectric breakdown (additional details can be found in Daniels et al. [36]).

2.2 Diffraction experiments

The 3DXRD experiments were performed at beamline ID11 of the European Synchrotron Radiation Facility. For the far-field experiment, which yields domain volume fraction and strain information, the beam was focused to a planar geometry of height 100 μm, illuminating the entire width of the specimen, with an energy of 78.395 keV (Pt edge). The sample was mounted 485 mm away from the Frelon4M detector [37] with 2048×2048 pixels of 50×50 μm^2 and diffraction images were collected while rotating the sample in the angular range of 345° about the vertical *z*-axis in steps of 0.1°. Three adjacent 100 μm layers of the sample were mapped in the as-processed state (F0), at an intermediate electric field strength close to the coercive field (F1) and at a field exceeding the coercive field (F2), with the electric field direction coincident with the rotational *z*-axis.

For the subsequent near-field experiment, which yields a grain map of the 3D microstructure, an X-ray beam energy of 37.010 keV was used. The energy was chosen to be

just below the Ba K-edge of 37.450 keV to optimize detector efficiency and minimize X-ray absorption in the sample. The beam dimensions were limited to 500 μm horizontally and 100 μm vertically with lenses and slits. Again three adjacent 100 μm layers of the sample were mapped through 360° in steps of 0.1° for the first layer and 0.2° for the remaining two due to time constraints. Near-field mapping employs two detectors simultaneously: the Frelon4M detector mentioned previously at a distance of 223 mm for indexing and the first screen of the Risø 3D-detector [38] with 2048×2048 pixels of 1.4×1.4 μm^2 at a distance of 8 mm for the grain reconstruction.

2.3 Grain map reconstruction

The collected diffraction image stacks were analyzed using the Fable software suite (2014), described in detail in Sørensen et al. [39]. Diffraction peak positions in the far-field Frelon4M detector data were extracted from the image stacks, and the patterns were indexed using GrainSpotter [40], which searches through orientation space to assign the diffraction spots to individual grains and subsequently refines the grain orientations and positions. The indexed grain orientations were then used as seeds for the reconstruction of a grain map from the near-field Risø 3D detector data, by means of a 3D generalization of the GrainSweeper [28] algorithm. For each 2×2×2 μm^3 voxel in the 0.5×0.5×0.2 mm^3 reconstruction, centered around the 0.3×0.3×0.1 mm^3 illuminated layers, the seed orientation with the highest completeness ratio of expected to observed number of reflections was assigned. The three adjacent, partly overlapping 200 μm reconstructed layers with a 100 μm inter-layer spacing were then stacked along the *z*-axis – the common poling and rotation axis – in order to obtain the 3D orientation map. For each voxel in the overlapping regions, the orientation with highest completeness was assigned, and voxels with completeness less than 60% were eliminated from the map. The orientation map was then registered to a grain map by assigning

adjacent voxels with pseudocubic misorientations less than 1° to the same grain. Finally microstructural information, such as grain neighbors, was extracted from the grain map using DREAM.3D [41].

2.4 Extraction of domain volume fractions and non-180° domain switching strains

The far-field data from the Frelon4M detector at F0, F1 and F2 was analyzed using Fable (2014) and GrainSpotter [40], resulting in a list of indexed grains, their orientations and 3D positions, as well as a list of diffraction spots assigned to each grain. 165 unique grains were indexed from the diffraction data covering a full range of orientation space. The (200)/(002) peaks of these grains were then extracted from the data since these peaks contain the information about the volume fractions, v_{200}, v_{020} and v_{002}, of the three unique ferroelastic domain variants, d_{200}, d_{020} and d_{002}. Although there are six unique polarization domain variants in tetragonal BT, only the three non-180° variants defined above can be distinguished with the present method since 180° domain variants have the same (002) peak positions. Each reflection was integrated along the rotation, ω, and the azimuth, η, yielding a radial profile along 2θ, which was then fit with Gaussian peaks centered at the split peak positions $2\theta_{min}$ and $2\theta_{max}$, as shown for a single grain at F0 and F2 in Fig. 1a. The intensities were corrected for Lorentz and polarization factors making them proportional to the volumes of each particular domain variant.

It should be noted that if a portion of the grain falls outside of the illuminated volume, the measured peak intensities may no longer be representative of the true domain volume fractions (for example, if the unilluminated part of the grain contains many domains of the d_{002} variant). To check for embedded grains, a partial scan (60° range) was measured with the beam opened to a height of 120 μm centered at the top and bottom layers. The ratio of the

peak intensity measured with the small beam to that measured with the larger beam for the reflections found in the angular range of both scans were compared on a grain-by-grain basis. If the median of this intensity ratio for all reflections belonging to a particular grain was found to be less than 0.80, the grain was excluded from further analysis. After this procedure, domain volume fractions were fit based on the intensity ratios of the (200)/(002) reflections and error bars were estimated as outlined by Oddershede et al. [35] for 139 embedded grains of 165 originally indexed. Other reasons for this reduction in grain numbers besides non-embedded grains include grains with specific reflection families falling in the 15° rotational range that was not covered in the experiment, small grains with weak reflections or grains with overlapping reflections.

The non-180° domain switching strain resolved along the poling direction, ε_p, was then calculated from the extracted domain volume fractions along the unit vector l as [42]:

$$\varepsilon_p = \left(\frac{c-a}{a_0}\right)\left(v_{200}l_1^2 + v_{020}l_2^2 + v_{002}l_3^2 - \frac{1}{3}\right) \quad (1)$$

where c and a are the tetragonal lattice parameters and, without an independent measure of the cubic lattice parameter, $a_0 = \sqrt[3]{ca^2}$, which assumes that there is no volume change at T_C. For l = <111> or $v_{200} = v_{020} = v_{002} = 1/3$ the strain $\varepsilon_p = 0$ because $v_{200} + v_{020} + v_{002} = 1$ and $l_1^2 + l_2^2 + l_3^2 = 1$. The maximum poling strain of $2(c-a)/3a_0$ is obtained for a single domain with <100> aligned along the electric field direction, while the minimum is $(a-c)/3a_0$. The propagation of error bars on v_{200}, v_{020} and v_{002} to an error bar on ε_p was performed as outlined by Oddershede et al. [35]

3 Results and discussion

3.1 Domain volume fractions and non-180° domain switching strains

Of the 165 grains initially indexed in the BT sample from the far-field 3DXRD data, non-180° domain switching strains, ε_p, were successfully extracted for 139 grains in the as-processed state (F0), at an intermediate electric field strength close to the coercive field (F1), and at a field exceeding the coercive field (F2). The relationship between the domain volume fractions and ε_p is demonstrated in Fig. 1b, where the bars are divided into three parts representing the volume fraction of each of the three non-180° ferroelastic domains, labeled with the domain *c*-axis misorientation with the poling direction, and the line is ε_p. The applied electric field results in the expected increase of ε_p, from −0.126±0.003% at F0 to 0.492±0.014% at F2, a direct result of the growth of d_{002} at the expense of d_{200} and d_{020}. This change is again clearly evident in the shifting of intensity from relatively even ratios at F0 to a very strong peak at F2 (Fig. 1a). The dominant growth of d_{002} is expected since it is by far the most favorably aligned with respect to the electric field vector at a misorientation of 10.5° (see Fig. 1c).

3.1.1 Non-180° domain switching strains in the initial as-processed sample state

Results indicate that, even in the as-processed state, individual grains do not contain equal volume fractions of the three possible ferroelastic domain variants (which would yield $\varepsilon_p = 0$ from Eq. (1)). This implies that upon cooling from the high temperature cubic phase through T_C, BT grains have a resultant anisotropic ferroelastic strain. Such strains must inevitably result in large elastic compliance strains at the grain scale to compensate, as observed in powder diffraction studies [2]. Fig. 2 shows the distribution of non-180° domain switching strains for all grains at F0. While the distribution is centered on zero, the as-processed strain

state of the sample is heterogeneous at the grain scale. It is hypothesized that ferroelectric domain interactions at grain boundaries are the likely cause of such heterogeneity. The electrostatic energy associated with these interactions must outweigh the increased elastic energy caused by the strain heterogeneity. Even so, the strains within the polycrystal balance and the mean volume weighted strain of the sample as a whole is $\varepsilon_{p,F0} = -0.002 \pm 0.001\%$.

3.2 Electric-field-induced ferroelastic strain response as a function of grain orientation

The inverse pole figure in Fig. 3a shows that the grains are randomly oriented as expected from the ceramic processing technique used. This is also confirmed by a Mackenzie type analysis [43]. The color represents the difference in non-180° domain switching strain between the F0 and F2 states, from hereon termed the ferroelastic strain response. From Fig. 3a it is clear that there is a general trend towards maximum and minimum ferroelastic strain response occurring at grain orientations with a <100> and <111> direction lying close to the electric field vector, respectively, as expected from the definition of ε_p in Eq. (1) as well as from previous powder diffraction results [2,18–20]. However, in addition to the observed first order correlation between grain orientation and ferroelastic strain response there are significant variations, or second order perturbations, within groups of grains with similar orientations. To highlight these variations, Fig. 3b shows the ferroelastic strain response as a function of $\cos^2\phi_{100}$, where ϕ_{100} is the misorientation between the electric field vector and the closest <100> direction in the given grain. Although it would be reasonable to think that grains with an initially negative strain would have more potential for domain switching and thus a larger ferroelastic strain response, the magnitude of initial ferroelastic strain, $\varepsilon_{p,F0}$, in a grain did not show any correlation with the response under high electric field.

3.3 Strain response heterogeneity

The results presented above indicate that while, at the bulk level, the ferroelastic strain response is as expected, i.e. zero at the initial state ($\varepsilon_{p,F0} = -0.002 \pm 0.001\%$) before increasing upon application of an electric field ($\varepsilon_{p,F1} = 0.088 \pm 0.001\%$ and $\varepsilon_{p,F2} = 0.135 \pm 0.001\%$), the ferroelastic strain response is heterogeneous at the grain scale. To study the effect of grain response averaging, the RMS distance to the trend line in Fig. 3b was calculated for an average over a group of grains of similar orientation at a variety of group sizes. It was found that the RMS distance was halved for groups of 10 similarly oriented grains as compared to individual grains, which agrees well with a previous investigation on $(0.82)Bi_{0.5}Na_{0.5}TiO_3 - (0.18)Bi_{0.5}K_{0.5}TiO_3$ utilizing the same far-field 3DXRD technique [44]. The present work builds on this by combining the domain volume-fraction information with the 3D microstructure grain map, allowing the grain-scale heterogeneity in ferroelastic strain response to be correlated with microstructural features of the grains themselves as well as their local grain neighborhood.

3.3.1 Effect of grain size and location within sample

Data from the near-field 3DXRD experiment was reconstructed in order to obtain the 3D grain map shown in Fig. 4. The grain map was overlaid with domain volume fractions and non-180° domain switching strains extracted from the far-field data, for instance $\varepsilon_{p,F0}$ or $\varepsilon_{p,F2}$ as in Fig. 4a and b**,** to enable a correlative study of strain response with sample microstructure.

In Fig. 5a the effect of grain size on ferroelastic strain response relative to the trend line in Fig. 3b is considered. The grain diameter here is calculated from the volumes derived from the grain map by assuming that the grains are perfect spheres. The calculated correlation coefficient of 0.1 indicates no significant correlation between grain diameter and ferroelastic

strain response. While previous experiments [18] and simulations [45] have demonstrated the effect of average sample grain size on domain switching behavior and material response, this effect does not appear to be present at the single grain level.

Another inherent feature of the individual grains within a polycrystalline sample is their location in the bulk versus at the surface of the sample. The distribution of ferroelastic strain response deviation from the trend line is shown in Fig. 5b for the 50 bulk grains in the sampled volume and in Fig. 5c for the 89 surface grains. The average of the bulk distribution is −0.01% with an absolute spread of 0.11%, while the average and absolute spread for the surface grains are 0.01% and 0.07%, respectively. This implies that there is no significant difference between bulk and surface grains in terms of their mean deviation from the linear trend, however, the spread of response magnitude in the surface grains is significantly lower than for bulk grains, with the probability of equal spread in the two distributions calculated as 0.06% for all data points and 3% for data points within the range of ±0.2% from the trend line. A potential reason for the ferroelastic strain response of the surface grains exhibiting significantly smaller spread around the trend line in Fig. 3b than the bulk grains could be that they experience fewer constraints due to the relaxed elastic and electrostatic boundary conditions at the sample surface [46].

A third microstructural property that can be extracted from the 3D grain map is the number of contact neighbors each grain has. This parameters is intimately linked to both the grain diameter and location, i.e. small/surface grains generally have fewer neighbors than large/bulk grains. However, the correlation coefficient between the ferroelastic strain response away from the trend line and the number of neighbors is merely 0.02, hence it is concluded that neither the grain diameter nor number of neighbors nor the location of grains within the sample have any significant effect on the ferroelastic strain response of individual bulk grains within the polycrystalline BT sample.

3.3.2 Effect of grain neighbor relations

Our results have demonstrated that the average ferroelastic strain response of a polycrystalline BT piezoceramic depends on grain orientation, with heterogeneities at the scale of individual grains that cannot be explained by grain size, surface or bulk location, or number of grain neighbors. In order to investigate the possible effects of grain interactions, two bulk grains, A and B, have been selected for further analysis. Some of their properties and those of their neighbors have been summarized in Table 1. The grains are of similar orientation relative to the electric field vector ($5° < \phi_{100} < 15°$ for both) and have similar grain diameters, slightly smaller than the sample average of 64 μm, yet they exhibit significantly different ferroelastic strain responses. Grain A, which was used as an example in Fig. 1, experiences are relatively large ferroelastic strain response, while grain B experiences a ferroelastic strain response approximately equal to the average of all grains of similar orientation.

The local environments of grains A and B and their neighbors, shown in Fig. 6, have been analyzed in detail in order to quantify various aspects of the grain neighborhoods, again summarized in Table 1. Both grains have a similar number of neighbors, 10 for A and 14 for B. This is comparable to the average number of 11 neighbors per grain in the sample. The neighbors of grain A are on average larger than those of grain B, which is expected considering the similar grain diameters of A and B and the difference in number of neighbors. However, this average does not make clear that grain A has two very large neighbors (diameters 78 and 85 μm), while the largest neighbor of grain B has a diameter of only 63 μm.

Fig. 6 also indicates that it is not only grain A that has a larger strain response than B, but so does its immediate neighborhood as a whole. A possible explanation is that grains in the

neighborhood of grain A are generally more favorably aligned relative to the field vector, which could also indicate that grains of similar orientation tend to cluster together within the sample. The Mackenzie type plot [43] in Fig. 7a, generated for all neighboring grain pairs in the sample, clearly follows the theoretical distribution expected for random orientations (shown as a solid line), thus there is no clustering of similarly oriented grains. For comparison, the distributions of neighbor misorientations for grains A and B are shown in Fig. 7b and c, respectively. These are calculated as the minimum rotation angle around an arbitrary axis needed to make the crystal lattice of grain A (or B) coincide with the crystal lattice of each of their neighbors. Here we note that the misorientation distributions for A and B are quite different, as also indicated by the mean and spread of the two distributions given in Table 1. Furthermore, neither A nor B exhibit any neighbor misorientations close to 60° which would be indicative of the presence of the so-called Σ3 boundaries that have been suggested to play a special role in connection with continuity of ferroelectric domain structures across grain boundaries [47,48].

3.4 Quantification of grain interactions by experiments and modeling

In Fig. 7a it was shown that for a random grain in the polycrystalline BT sample it is statistically likely that the grain is surrounded by neighbors that come very close to the average structure of the entire sample, while Fig. 7b and c clearly demonstrated that in reality an individual grain sees a local neighborhood that is significantly different from the statistical average. So, while the bulk macroscopic properties and response are predictable, at the grain-scale the material behavior is far more localized in nature. This effect is demonstrated by Haug et al. [49] by comparing self-consistent (SC) models to multi-grain finite element (FE) models. In SC models, the stress state of each grain is calculated by assuming that the grain is embedded in a homogeneous matrix that has the properties of the average polycrystal, thus,

grain-to-grain interactions are not considered. In a FE model, the polycrystal is treated as an aggregate of discrete grains and grain-to-grain interactions are maintained. The polarization hysteresis and strain "butterfly" loops for both models agree quite well, however, the SC model underpredicts the maximum stresses and strains that can develop at grain boundaries, which arise due to forced compatibility between grains as the sample is deformed. In fact, recent simulations on related ferroelectric/ferroelastic materials have shown a large spread in intergranular residual stresses even when no field is applied and the average internal stress is zero [50], a result supported by the grain-scale strain heterogeneity in the non-180° domain switching strain measured here in the initial zero field state.

The above-mentioned local maximum stresses and strains are in fact quite important for the reproducibility and reliability of the ferroelectric response. Depending on the actuation mechanisms within a specific ceramic material, the stress concentrations may vary significantly due to the degree of strain anisotropy, and lead to the initiation of cracks, accelerated fatigue and inevitable failure of the material. Additionally, the elastic compliance anisotropy and its ability to compensate for strain heterogeneities at the grain scale is equally important. Already in the present data set there are, however, factors indicating that the intrinsic strains are even more local in nature. For instance all the raw data in Fig. 1a have more intensity between the two peaks corresponding to $2\theta_{min}$ and $2\theta_{max}$ than justified by the combined tails of the peaks, indicating a lattice strain distribution within the domains that tends towards the common pseudocubic orientation of the domains. This scattering has been speculated to result from strain compatibility at the domain boundaries [51], but in the future techniques such as dark field X-ray microscopy [52] will enable direct measurements of the spatial distributions of lattice strains within individual domains.

While there are still more advanced experimental routes to follow to quantify interactions between individual grains and domains in a polycrystalline piezoceramic, the same certainly also holds for modeling of this material class. Previous modeling attempts have mostly considered the effect of grain orientation, assuming that all grains are of equal size with all domains of equal volume fraction [49,53,54], while the present study has clearly demonstrated that this is not the case. FEM simulations by Kamlah et al. [53] show that when there is limited potential for domain switching the amount of strain "available" to the grain is greatly reduced. Thus, two neighboring grains, even though they are of similar orientation and size, may develop high intergranular stresses if one of them has more availability for domain switching than the other. Fig. 2 clearly indicates that this is the case even in the as-processed state and should be an important consideration for modeling of real materials. Interpretation of these results would be greatly aided by the implementation of, for example, crystal plasticity based models where the incremental transformation by domain wall motion is equivalent to incremental slip on a slip system. Such combined experimental and modeling approaches have previously been used to study deformation twinning in hexagonal close packed metals such as magnesium [30,55] and zirconium [56–58]. The state of the sample is described by the volume fractions of each domain type, making the modeling results directly comparable with their experimental counterparts.

4 Conclusions

Based on a 3DXRD grain mapping the grain-scale domain volume fractions in 139 grains of a BT ceramic were successfully extracted, and from this information the ferroelastic strain response of each grain was derived. In agreement with previous experiments (i.e. powder diffraction), it was found that tetragonal domains with *c*-axes more closely aligned with the

poling direction ([001] aligned grains) tend to grow with the application of an electric field, thus resulting in larger ferroelastic strain responses. Although the average ferroelastic strain response of the sample was as expected, large variations exist in the behavior of individual grains of similar orientations. An important observation is that these variations are not restricted to the ferroelastic strain response, they were in fact observed already in the initial as-processed state of the sample. It is suggested that these grain-scale variations arise from local strain and electrostatic neighborhoods being highly heterogeneous within the bulk polycrystal. The neighborhood heterogeneities were clearly demonstrated from the grain map for two selected bulk grains of similar orientation, size and number of neighbors that were found to exhibit very different ferroelastic strain responses. In addition, the diffraction data showed evidence of substantial lattice strains within domains, probably mainly in the grain boundary regions to accommodate the transition between domains and ensure stress equilibrium. All of these results suggest that the minimization of electrostatic potentials at the grain boundaries due to interacting ferroelectric domains is the cause of the observed grain-scale strain heterogeneities both in the as-processed state of the sample and when an electrical field is applied. These results are of critical importance both when building the starting conditions and considering the validity of grain-scale modeling efforts, and provide additional considerations in the design of novel electro-mechanical materials. Additionally, the combination of near-field and far-field diffraction techniques has the potential to reveal the grain-scale nature of, for example, shape memory and superelastic alloys that exhibit ferroelastic phase changes, or any other complex materials where grain-to-grain interactions are of importance.

Acknowledgements

The authors acknowledge support from the Danish Independent Research Council | Technology and Production Sciences case no. 12-127449 and Australian Research Council Discovery Project DP 120103968. MM and JO acknowledge the Danish Agency for Science, Technology and Innovation for covering expenses in relation to the synchrotron experiment (through Danscatt). JED acknowledges support from an Australian Institute of Nuclear Science and Engineering research fellowship and travel funding provided by the International Synchrotron Access Program (ISAP) managed by the Australian Synchrotron and funded by the Australian Government. The European Synchrotron Radiation Facility is acknowledged for the provision of beamtime.

References

[1] W. Eerenstein, N.D. Mathur, J.F. Scott, Multiferroic and magnetoelectric materials, Nature. 442 (2006) 759–65. doi:10.1038/nature05023.

[2] A. Pramanick, D. Damjanovic, J.E. Daniels, J.C. Nino, J.L. Jones, Origins of Electro-Mechanical Coupling in Polycrystalline Ferroelectrics During Subcoercive Electrical Loading, J. Am. Ceram. Soc. 94 (2011) 293–309. doi:10.1111/j.1551-2916.2010.04240.x.

[3] J. Rödel, W. Jo, K.T.P. Seifert, E.-M. Anton, T. Granzow, Perspective on the Development of Lead-free Piezoceramics, J. Am. Ceram. Soc. 92 (2009) 1153–1177. doi:10.1111/j.1551-2916.2009.03061.x.

[4] J. Rödel, K.G. Webber, R. Dittmer, W. Jo, M. Kimura, Transferring lead-free piezoelectric ceramics into application, J. Eur. Ceram. Soc. 35 (2015) 1659–1681. doi:10.1016/j.jeurceramsoc.2014.12.013.

[5] T. Takenaka, K. Maruyama, K. Sakata, (Bi1/2Na1/2)TiO3-BaTiO3 System for Lead-Free Piezoeletric Ceramics, Jpn. J. Appl. Phys. 30 (1991) 2236–2239.

[6] Y. Makiuchi, R. Aoyagi, Y. Hiruma, H. Nagata, T. Takenaka, (Bi1/2Na1/2)TiO3-(Bi1/2K1/2)TiO3-BaTiO3-Based Lead-Free Piezoelectric Ceramics, Jpn. J. Appl. Phys. 44 (2005) 4350–4353. doi:10.1143/JJAP.44.4350.

[7] H. Nagata, M. Yoshida, Y. Makiuchi, T. Takenaka, Large Piezoelectric Constant and High Curie Temperature of Lead-Free Piezoelectric Ceramic Ternary System Based on Bismuth Sodium Titanate-Bismuth Potassium Titanate- Barium Titanate near the

Morphotropic Phase Boundary, Jpn. J. Appl. Phys. 42 (2003) 7401–7403. doi:10.1143/JJAP.42.7401.

[8] J. Shieh, K.C. Wu, C.S. Chen, Switching characteristics of MPB compositions of (Bi0.5Na0.5)TiO3-BaTiO3-(Bi0.5K0.5)TiO3 lead-free ferroelectric ceramics, Acta Mater. 55 (2007) 3081–3087. doi:10.1016/j.actamat.2007.01.012.

[9] K.T.P. Seifert, W. Jo, J. Rödel, Temperature-Insensitive Large Strain of (Bi0.5Na0.5)TiO3-(Bi0.5K0.5)TiO3-(K0.5Na0.5)NbO3 Lead-Free Piezoceramics, J. Am. Ceram. Soc. 93 (2010) 1392–1396. doi:10.1111/j.1551-2916.2009.03573.x.

[10] T.R. Shrout, S.J. Zhang, Lead-free piezoelectric ceramics: Alternatives for PZT ?, J. Electroceramics. 19 (2007) 111–124. doi:10.1007/s10832-007-9047-0.

[11] S.-T. Zhang, A.B. Kounga, E. Aulbach, H. Ehrenberg, J. Rödel, Giant strain in lead-free piezoceramics Bi 0.5 Na 0.5 Ti O 3 - Ba Ti O 3 - K 0.5 Na 0.5 Nb O 3 system, Appl. Phys. Lett. 91 (2007) 112906. doi:10.1063/1.2783200.

[12] G. Arlt, P. Sasko, Domain configuration and equilibrium size of domains in BaTiO3 ceramics, J. Appl. Phys. 51 (1980) 4956. doi:10.1063/1.328372.

[13] G. Arlt, Twinning in ferroelectric and ferroelastic ceramics: stress relief, J. Mater. Sci. 25 (1990) 2655–2666. doi:10.1007/BF00584864.

[14] M. Varlioglu, U. Lienert, J.-S. Park, J.L. Jones, E. Üstündag, Thermal and Electric Field-Dependent Evolution of Domain Structures in Polycrystalline BaTiO 3 Using the 3D-XRD Technique, Texture, Stress. Microstruct. 2010 (2010) 910793. doi:10.1155/2010/910793.

[15] S.R. Agnew, C.N. Tomé, D.W. Brown, T.M. Holden, S.C. Vogel, Study of slip mechanisms in a magnesium alloy by neutron diffraction and modeling, Scr. Mater. 48 (2003) 1003–1008. doi:10.1016/S1359-6462(02)00591-2.

[16] B. Clausen, T. Lorentzen, M. a. M. Bourke, M.R. Daymond, Lattice strain evolution during uniaxial tensile loading of stainless steel, Mater. Sci. Eng. A. 259 (1999) 17–24. doi:10.1016/S0921-5093(98)00878-8.

[17] Y. Ivry, D. Chu, J.F. Scott, C. Durkan, Domains Beyond the Grain Boundary, Adv. Funct. Mater. 21 (2011) 1827–1832. doi:10.1002/adfm.201002142.

[18] M.J. Hoffmann, M. Hammer, a. Endriss, D.C. Lupascu, Correlation between microstructure, strain behavior, and acoustic emission of soft PZT ceramics, Acta Mater. 49 (2001) 1301–1310. doi:10.1016/S1359-6454(01)00025-8.

[19] G. Tutuncu, M. Motahari, M.R. Daymond, E. Ustundag, A modified Rietveld method to model highly anisotropic ceramics, Acta Mater. 60 (2012) 1494–1502. doi:10.1016/j.actamat.2011.11.050.

[20] R.C. Rogan, E. Üstündag, B. Clausen, M.R. Daymond, Texture and strain analysis of the ferroelastic behavior of Pb(Zr,Ti)O3 by in situ neutron diffraction, J. Appl. Phys. 93 (2003) 4104. doi:10.1063/1.1558229.

[21] J.A. Hooton, W.J. Merz, Etch patterns and ferroelectric domains in BaTiO3 single crystals, Phys. Rev. 98 (1955) 409–413. doi:10.1103/PhysRev.98.409.

[22] Y. Hu, H. Chan, Scanning electron microscopy and transmission electron microscopy study of ferroelectric domains in doped BaTiO3, J. Am. Ceram. Soc. 69 (1986) 594–602. doi:10.1111/j.1151-2916.1986.tb04814.x.

[23] F. Saurenbach, B.D. Terris, Imaging of ferroelectric domain walls by force microscopy, Appl. Phys. Lett. 56 (1990) 1703. doi:10.1063/1.103122.

[24] A. Roelofs, U. Böttger, R. Waser, F. Schlaphof, S. Trogisch, L.M. Eng, Differentiating 180° and 90° switching of ferroelectric domains with three-dimensional piezoresponse force microscopy, Appl. Phys. Lett. 77 (2000) 3444–3446. doi:10.1063/1.1328049.

[25] S. Hong, J. Woo, H. Shin, J.U. Jeon, Y.E. Pak, E.L. Colla, et al., Principle of ferroelectric domain imaging using atomic force microscope, J. Appl. Phys. 89 (2001) 1377–1386. doi:10.1063/1.1331654.

[26] H. Park, J. Jung, D.-K. Min, S. Kim, S. Hong, H. Shin, Scanning resistive probe microscopy: Imaging ferroelectric domains, Appl. Phys. Lett. 84 (2004) 1734. doi:10.1063/1.1667266.

[27] S. Schmidt, S.F. Nielsen, C. Gundlach, L. Margulies, X. Huang, D. Juul Jensen, Watching the Growth of Bulk Grains During Recrystallization of Deformed Metals, Science (80-.). 305 (2004) 229–232. doi:10.1126/science.1098627.

[28] S. Schmidt, U.L. Olsen, H.F. Poulsen, H.O. Sørensen, E.M. Lauridsen, L. Margulies, et al., Direct observation of 3-D grain growth in Al-0.1% Mn, Scr. Mater. 59 (2008) 491–494. doi:10.1016/j.scriptamat.2008.04.049.

[29] C.C. Aydiner, J. V. Bernier, B. Clausen, U. Lienert, C.N. Tomé, D.W. Brown, Evolution of stress in individual grains and twins in a magnesium alloy aggregate, Phys. Rev. B - Condens. Matter Mater. Phys. 80 (2009) 1–6. doi:10.1103/PhysRevB.80.024113.

[30] H. Abdolvand, M. Majkut, J. Oddershede, S. Schmidt, U. Lienert, B.J. Diak, et al., On the deformation twinning of Mg AZ31B: A three-dimensional synchrotron X-ray diffraction experiment and crystal plasticity finite element model, Int. J. Plast. 70 (2015) 77–97. doi:10.1016/j.ijplas.2015.03.001.

[31] T.R. Bieler, L. Wang, A.J. Beaudoin, P. Kenesei, U. Lienert, In Situ Characterization of Twin Nucleation in Pure Ti Using 3D-XRD, Metall. Mater. Trans. A. 45A (2014) 109–122. doi:10.1007/s11661-013-2082-3.

[32] L. Wang, J. Lind, H. Phukan, P. Kenesei, J.-S. Park, R.M. Suter, et al., Mechanical twinning and detwinning in pure Ti during loading and unloading – An in situ high-energy X-ray diffraction microscopy study, Scr. Mater. 92 (2014) 35–38. doi:10.1016/j.scriptamat.2014.08.008.

[33] J. Lind, S.F. Li, R. Pokharel, U. Lienert, A.D. Rollett, R.M. Suter, Tensile twin nucleation events coupled to neighboring slip observed in three dimensions, Acta Mater. 76 (2014) 213–220. doi:10.1016/j.actamat.2014.04.050.

[34] H. Abdolvand, M. Majkut, J. Oddershede, J.P. Wright, M.R. Daymond, Study of 3-D stress development in parent and twin pairs of a hexagonal close-packed polycrystal: Part I – in-situ three-dimensional synchrotron X-ray diffraction measurement, Acta Mater. 93 (2015) 246–255. doi:10.1016/j.actamat.2015.04.020.

[35] J. Oddershede, M. Majkut, Q. Cao, S. Schmidt, P. Wright, P. Kenesei, et al., Quantitative grain-scale ferroic domain volume fractions and domain switching strains from three-dimensional X-ray diffraction data, J. Appl. Crystallogr. 48 (2015) 882–889. doi:10.1107/S1600576715007669.

[36] J.E. Daniels, A. Pramanick, J.L. Jones, Time-Resolved Characterization of Ferroelectrics Using High-Energy X-ray Diffraction, IEEE Trans. Ultrason. Ferroelectr. Freq. Control. 56 (2009) 1539–1545.

[37] J.C. Labiche, O. Mathon, S. Pascarelli, M. a. Newton, G.G. Ferre, C. Curfs, et al., Invited article: The fast readout low noise camera as a versatile x-ray detector for time resolved dispersive extended x-ray absorption fine structure and diffraction studies of dynamic problems in materials science, chemistry, and catalysis, Rev. Sci. Instrum. 78 (2007) 091301. doi:10.1063/1.2783112.

[38] U.L. Olsen, S. Schmidt, H.F. Poulsen, A high-spatial-resolution three-dimensional detector array for 30-200 keV X-rays based on structured scintillators, J. Synchrotron Radiat. 15 (2008) 363–370. doi:10.1107/S0909049508011370.

[39] H.O. Sørensen, S. Schmidt, J.P. Wright, G.B.M. Vaughan, S. Techert, E.F. Garman, et al., Multigrain crystallography, Zeitschrift Fur Krist. 227 (2012) 63–78. doi:10.1524/zkri.2012.1438.

[40] S. Schmidt, GrainSpotter: a fast and robust polycrystalline indexing algorithm, J. Appl. Crystallogr. 47 (2014) 276–284. doi:10.1107/S1600576713030185.

[41] M.A. Groeber, M.A. Jackson, DREAM.3D: A Digital Representation Environment for the Analysis of Microstructure in 3D, Integr. Mater. Manuf. Innov. 3 (2014) 5. doi:10.1186/2193-9772-3-5.

[42] D.A. Hall, A. Steuwer, B. Cherdhirunkorn, P.J. Withers, T. Mori, Texture of poled tetragonal PZT detected by synchrotron X-ray diffraction and micromechanics analysis, Mater. Sci. Eng. A. 409 (2005) 206–210. doi:10.1016/j.msea.2005.05.115.

[43] J.K. Mackenzie, Second paper on statistics associated with the random distribution of cubes, Biometrika. 45 (1958) 229–240.

[44] J.E. Daniels, M. Majkut, Q. Cao, S. Schmidt, J.P. Wright, J. Oddershede, Heterogeneous grain-scale response in ferroic polycrystals under electric field, Sci. Reports, Accept. (2016).

[45] S. Choudhury, Y.L. Li, C. Krill, L.Q. Chen, Effect of grain orientation and grain size on ferroelectric domain switching and evolution: Phase field simulations, Acta Mater. 55 (2007) 1415–1426. doi:10.1016/j.actamat.2006.09.048.

[46] Y. Li, S.Y. Hu, Z.K. Liu, L.Q. Chen, Effect of electrical boundary conditions on ferroelectric domain structures in thin films, Appl. Phys. Lett. 81 (2002) 427–429.

doi:10.1063/1.1492025.

[47] F. Ernst, M.L. Mulvihill, O. Kienzle, M. Rühle, Preferred Grain Orientation Relationships in Sintered Perovskite Ceramics, J. Am. Ceram. Soc. 84 (2001) 1885–1890.

[48] S. Tsurekawa, K. Ibaraki, K. Kawahara, T. Watanabe, The continuity of ferroelectric domains at grain boundaries in lead zirconate titanate, Scr. Mater. 56 (2007) 577–580. doi:10.1016/j.scriptamat.2006.12.029.

[49] A. Haug, J.E. Huber, P.R. Onck, E. Van der Giessen, Multi-grain analysis versus self-consistent estimates of ferroelectric polycrystals, J. Mech. Phys. Solids. 55 (2007) 648–665. doi:10.1016/j.jmps.2006.06.009.

[50] L. Daniel, D.A. Hall, P.J. Withers, A multiscale model for reversible ferroelectric behaviour of polycrystalline ceramics, Mech. Mater. 71 (2014) 85–100. doi:10.1016/j.mechmat.2014.01.006.

[51] J.E. Daniels, J.L. Jones, T.R. Finlayson, Characterization of domain structures from diffraction profiles in tetragonal ferroelastic ceramics, J. Phys. D. Appl. Phys. 39 (2006) 5294–5299. doi:10.1088/0022-3727/39/24/029.

[52] H. Simons, A. King, W. Ludwig, C. Detlefs, W. Pantleon, S. Schmidt, et al., Dark-field X-ray microscopy for multiscale structural characterization, Nat. Commun. 6 (2015) 6098–6103. doi:10.1038/ncomms7098.

[53] M. Kamlah, A.C. Liskowsky, R.M. McMeeking, H. Balke, Finite element simulation of a polycrystalline ferroelectric based on a multidomain single crystal switching model, Int. J. Solids Struct. 42 (2005) 2949–2964. doi:10.1016/j.ijsolstr.2004.09.045.

[54] A. Haug, P.R. Onck, E. Van der Giessen, Development of inter- and intragranular stresses during switching of ferroelectric polycrystals, Int. J. Solids Struct. 44 (2007) 2066–2078. doi:10.1016/j.ijsolstr.2006.07.024.

[55] A. Staroselsky, L. Anand, A constitutive model for hcp materials deforming by slip and twinning, Int. J. Plast. 19 (2003) 1843–1864. doi:10.1016/S0749-6419(03)00039-1.

[56] H. Abdolvand, M.R. Daymond, Multi-scale modeling and experimental study of twin inception and propagation in hexagonal close-packed materials using a crystal plasticity finite element approach—Part I: Average behavior, J. Mech. Phys. Solids. 61 (2013) 783–802. doi:10.1016/j.jmps.2012.10.013.

[57] H. Abdolvand, M.R. Daymond, Multi-scale modeling and experimental study of twin inception and propagation in hexagonal close-packed materials using a crystal plasticity finite element approach; part II: Local behavior, J. Mech. Phys. Solids. 61 (2013) 803–818. doi:10.1016/j.jmps.2012.10.017.

[58] H. Abdolvand, M. Majkut, J. Oddershede, J.P. Wright, M.R. Daymond, Study of 3-D stress development in parent and twin pairs of a hexagonal close-packed polycrystal: Part II – crystal plasticity finite element modeling, Acta Mater. 93 (2015) 235–245. doi:10.1016/j.actamat.2015.04.025.

Figure captions

Fig. 1. For the same [001]-oriented grain (a) the typical raw and integrated (200)/(002) diffraction spots at the initial (F0) and final (F2) electric fields, and (b) the change in volume fraction of domains (bars) with poling and the corresponding non-180° domain switching strain along the poling direction (line). Each segment of the bar represents a domain within the grain of interest and is labeled with the misorientation between the domain c-axis and the applied field direction also illustrated in (c).

Fig. 2. Distribution of non-180° domain switching strains in the initial as-processed state of the BT sample. The distribution width is an indicator of the grain-scale strain heterogeneity in the as-processed state.

Fig. 3. (a) The orientation of the 139 indexed grains color coded according to the ferroelastic strain response from step F0 to F2, and (b) $\varepsilon_{p,F2}-\varepsilon_{p,F0}$ as a function of $\cos^2\phi_{100}$, where ϕ_{100} is the misorientation between the electric field vector and the closest <100> direction in the given grain. The trend line in (b) corresponds to the average behavior expected for a given grain orientation.

Fig. 4. Grain maps of the entire sample color coded according to (a) $\varepsilon_{p,F0}$, and (b) $\varepsilon_{p,F2}$. The poling direction is along the vertical *z*-axis. The grey grains are the ones where the fit of domain volume fractions failed, primarily grains on the top and bottom surfaces that were removed from the analysis because they extend beyond the illuminated volume.

Fig. 5. Ferroelastic strain response difference from average behavior as a function of grain diameter (a), and distribution of ferroelastic strain responses away from average behavior for the 50 bulk grains (b) and 89 surface grains (c).

Fig. 6. Cutouts of the grain map showing grain A and B and their respective neighbors color-coded according to the ferroelastic strain response of each grain, $\varepsilon_{p,F2}-\varepsilon_{p,F0}$. No strain information was fit for the grey neighbor grains, but their sizes and orientations are known.

Fig. 7. Mackenzie type plot for all misorientations of neighboring grains within the sample volume and the theoretical distribution of random orientations (a), neighbor misorientation distribution for grain A (b) and grain B (c).

Tables

Table 1. Properties of the two selected grains A and B. For the neighbor diameters, neighbor orientation relative the poling direction (ϕ_{100}) and neighbor misorientation relative to the grains in question, both the average and spread of the distribution over all neighbors for grains A and B are given

		Grain A	**Grain B**
ϕ_{100} (°)		10.5°	7.17°
Grain diameter (μm)		56	55
$\varepsilon_{p,F2}-\varepsilon_{p,F0}$ (%)		0.617±0.015	0.217±0.0002
Volume fraction switched from F0 to F2		0.61	0.21
Number of neighbors		10	14
Neighbor diameter (μm)	average	84	63
	spread	44	28
Neighbor ϕ_{100} (°)	average	36	43
	spread	15	25
Neighbor misorientation (°)	average	40	32
	spread	8	12

Fig. 1.

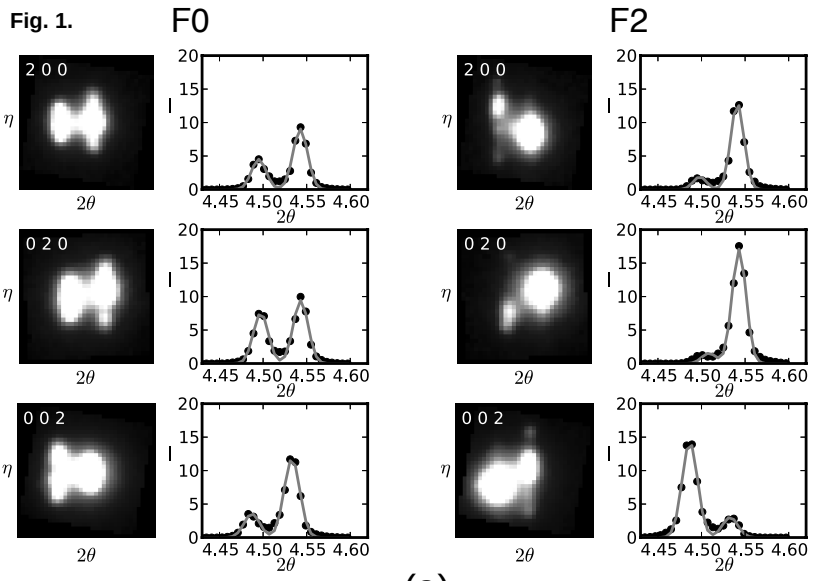
F0
F2
2 0 0
0 2 0
0 0 2
η
2θ
I
4.45 4.50 4.55 4.60

(a)

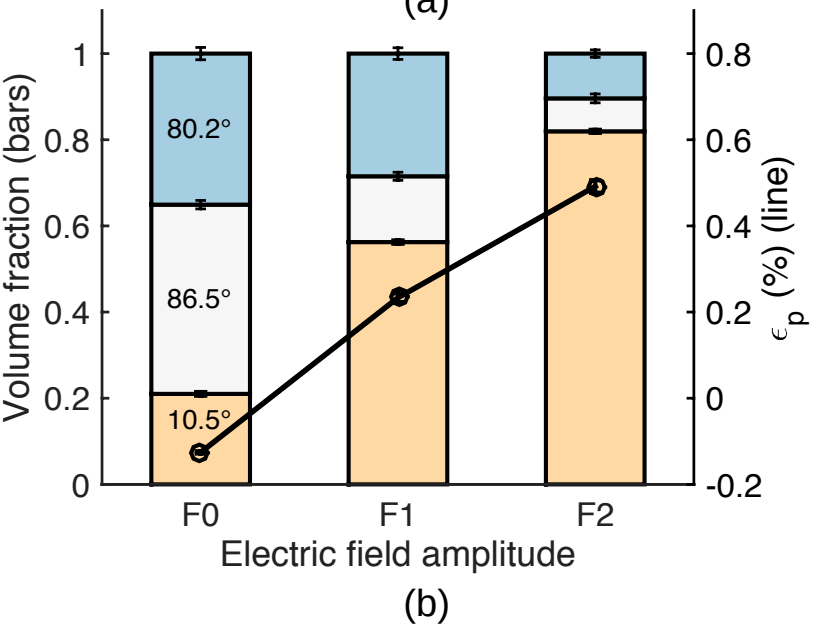
Volume fraction (bars)
ϵ_p (%) (line)
80.2°
86.5°
10.5°
F0
F1
F2
Electric field amplitude

(b)

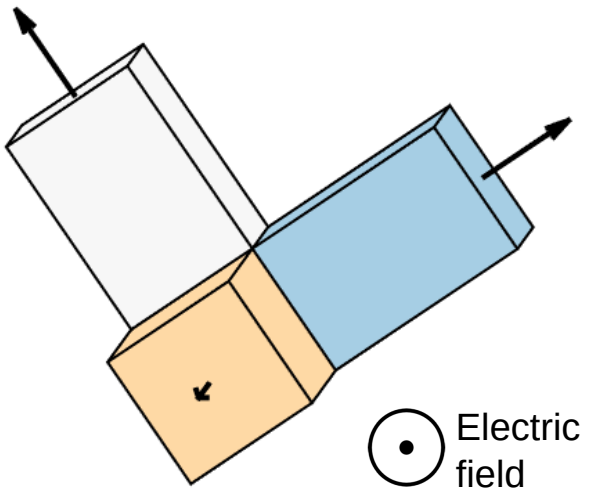
Electric
field

Fig. 2.

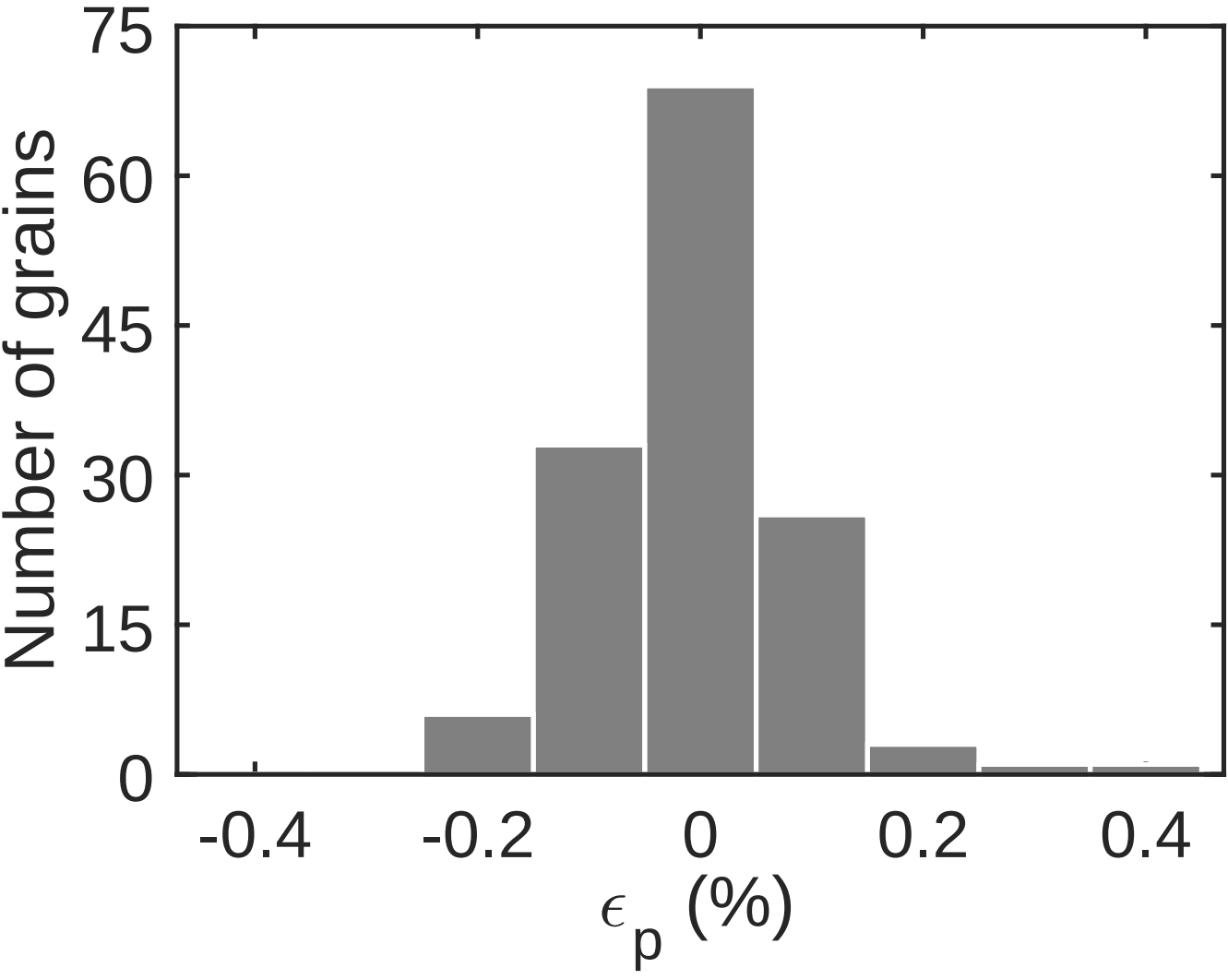

Fig. 3.

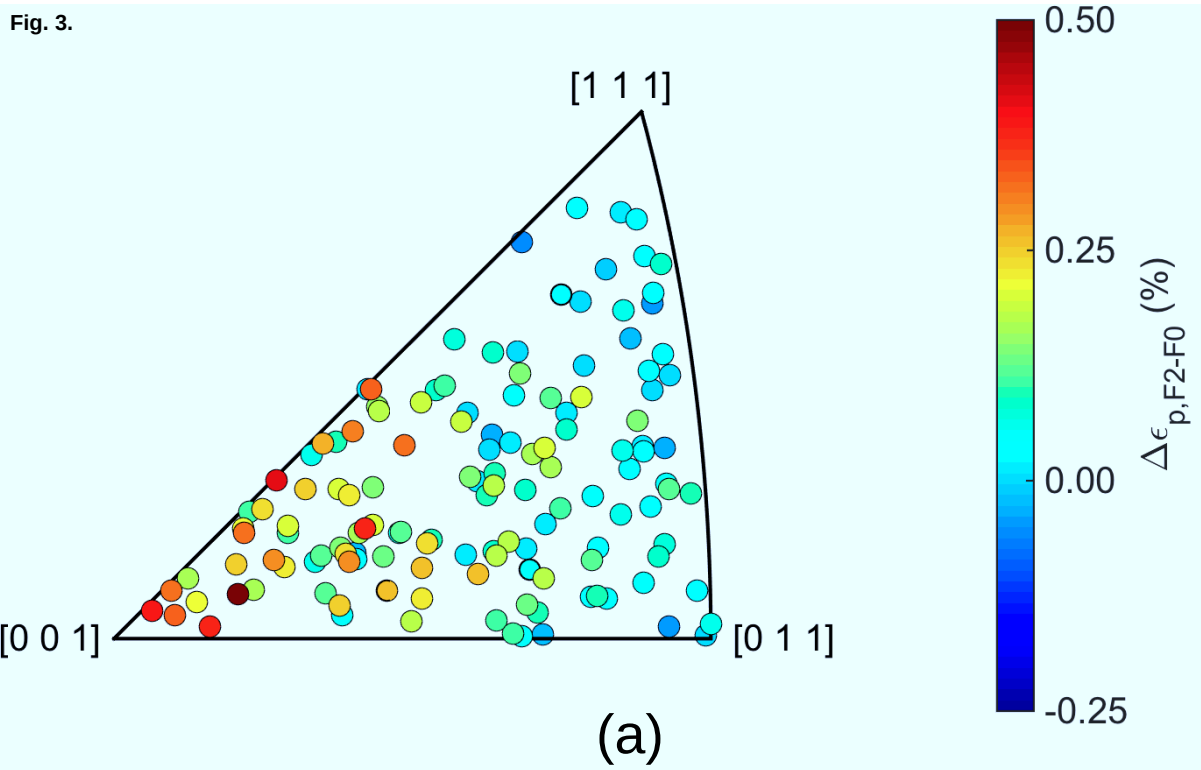
[1 1 1]
[0 0 1]
[0 1 1]
0.50
0.25
0.00
-0.25
$\Delta\epsilon_{p,F2-F0}$ (%)

(a)

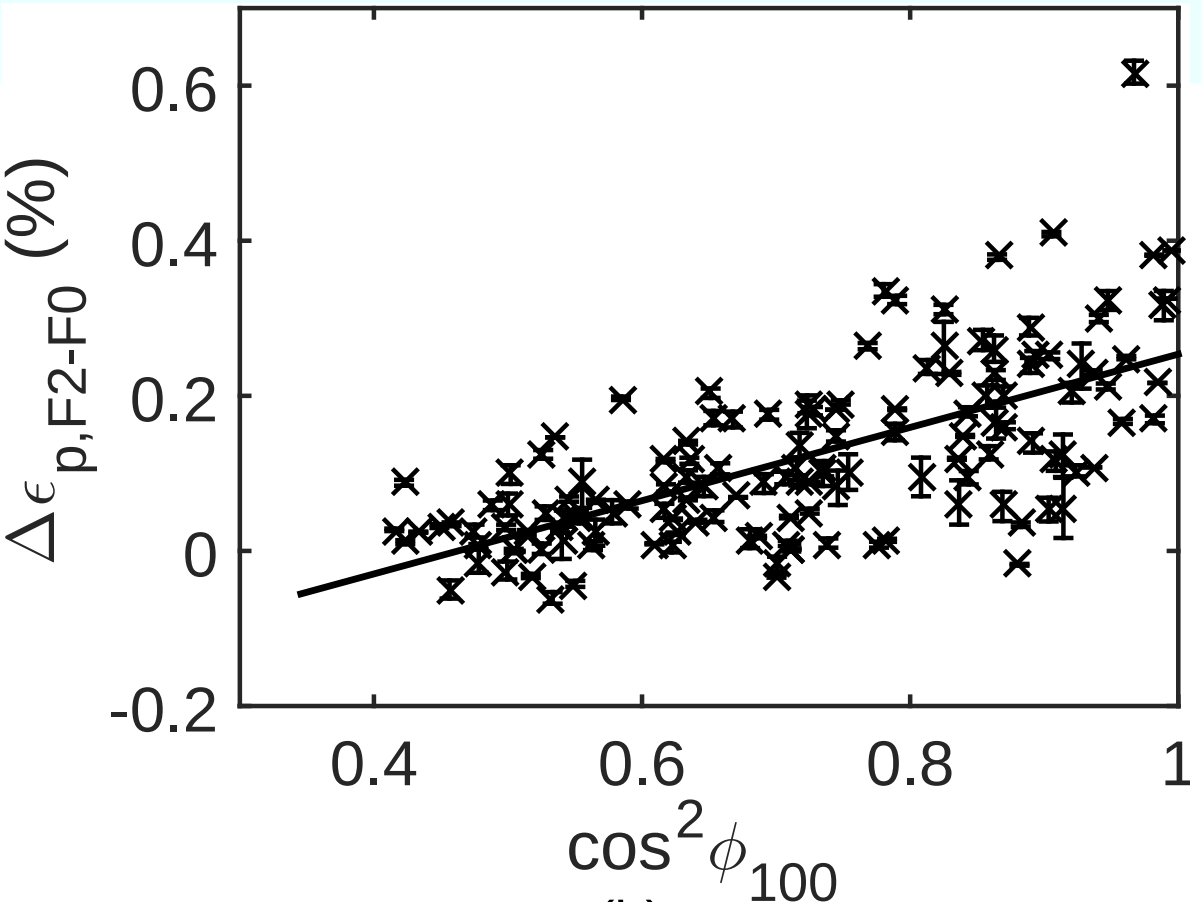
0.6
0.4
0.2
0
-0.2
0.4
0.6
0.8
1
$\Delta\epsilon_{p,F2-F0}$ (%)
$\cos^2\phi_{100}$

Fig. 4.

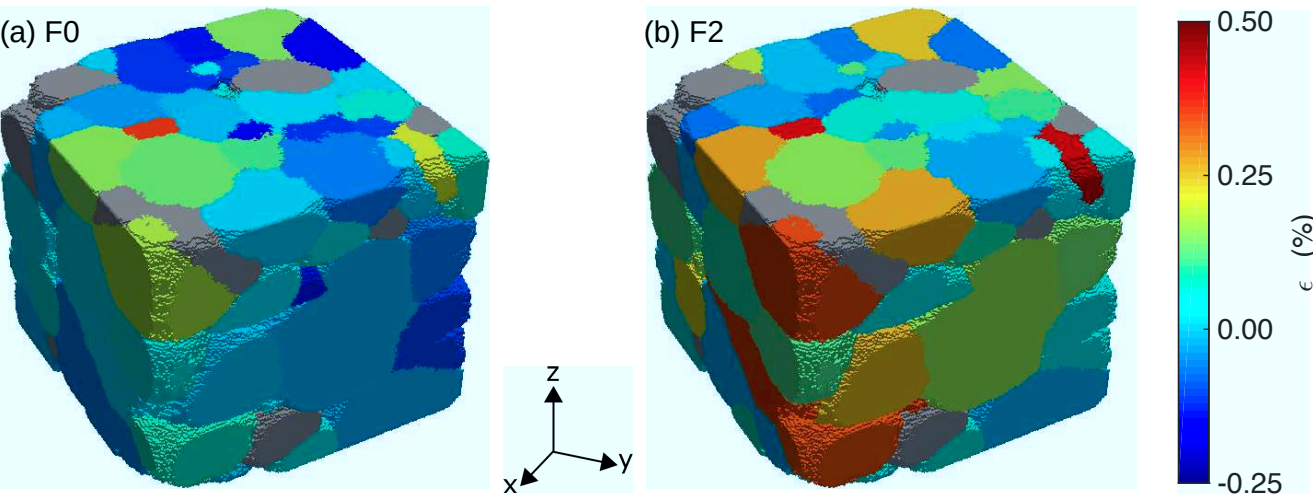

Fig. 5.

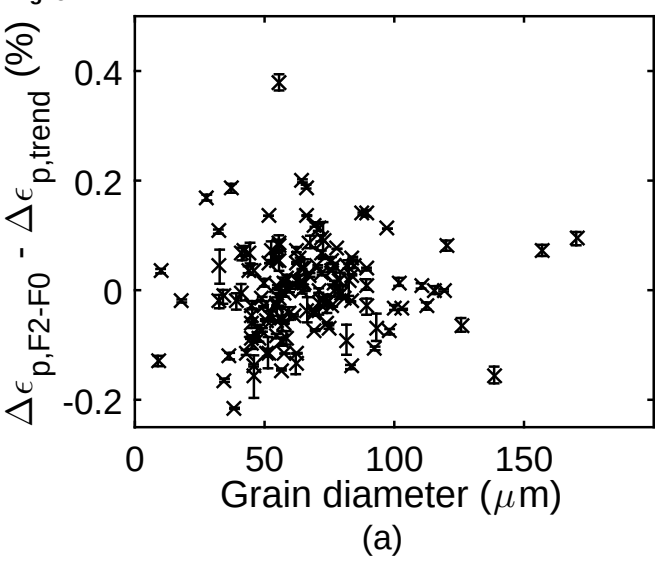
0.4
0.2
0
-0.2
$\Delta\epsilon_{p,F2\text{-}F0}$ - $\Delta\epsilon_{p,trend}$ (%)
0
50
100
150
Grain diameter (μm)

(a)

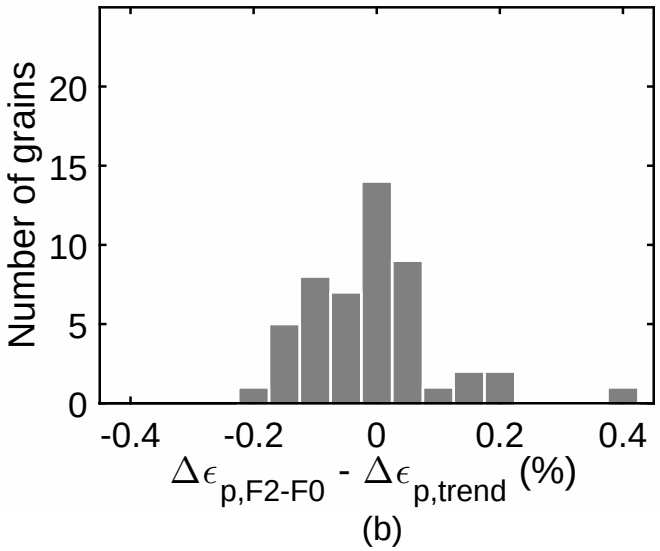
20
15
10
5
0
Number of grains
-0.4
-0.2
0
0.2
0.4
$\Delta\epsilon_{p,F2\text{-}F0}$ - $\Delta\epsilon_{p,trend}$ (%)

(b)

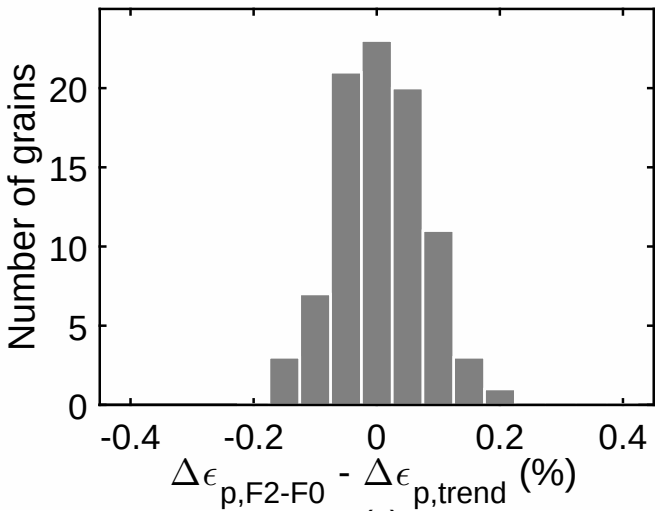
20
15
10
5
0
Number of grains
-0.4
-0.2
0
0.2
0.4
$\Delta\epsilon_{p,F2\text{-}F0}$ - $\Delta\epsilon_{p,trend}$ (%)

Fig. 6.

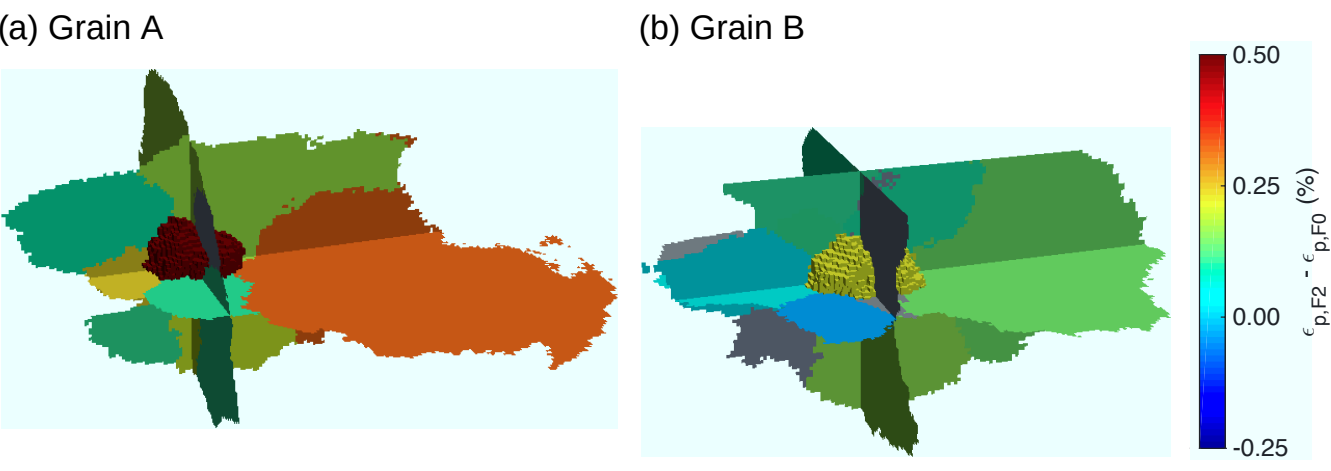

Fig. 7

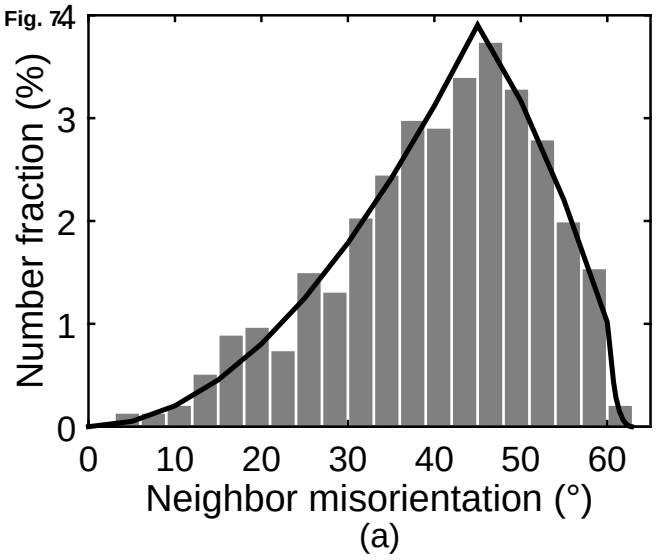
Number fraction (%)
0
1
2
3
4
0
10
20
30
40
50
60
Neighbor misorientation (°)

(a)

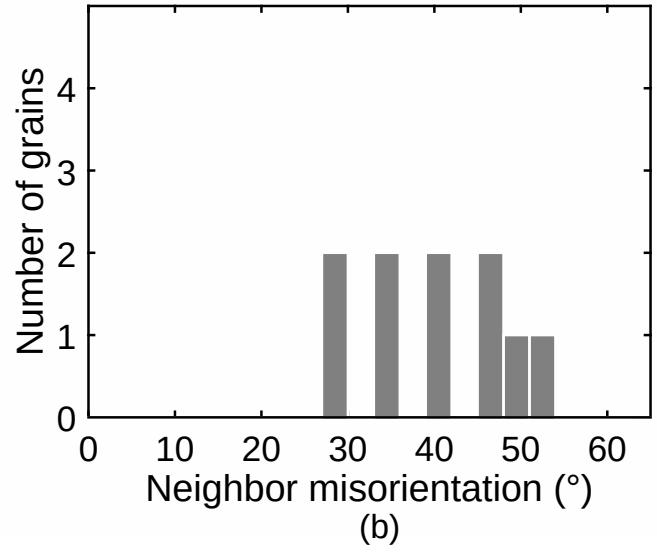
Number of grains
0
1
2
3
4
0
10
20
30
40
50
60
Neighbor misorientation (°)

(b)

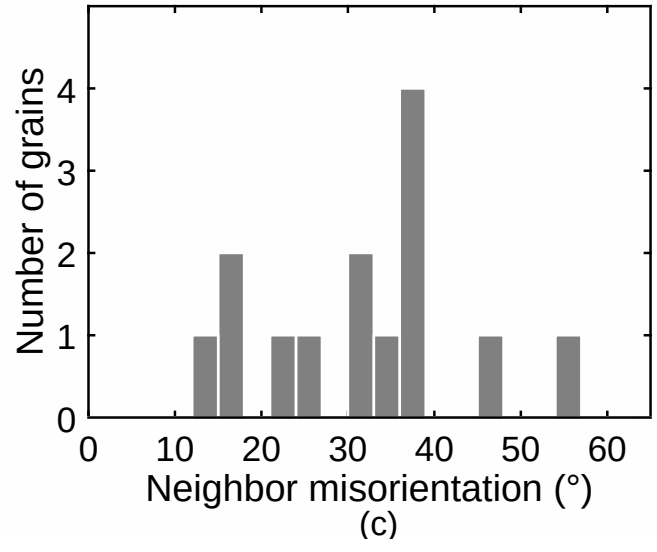
Number of grains
0
1
2
3
4
0
10
20
30
40
50
60
Neighbor misorientation (°)

(c)

*Graphical Abstract

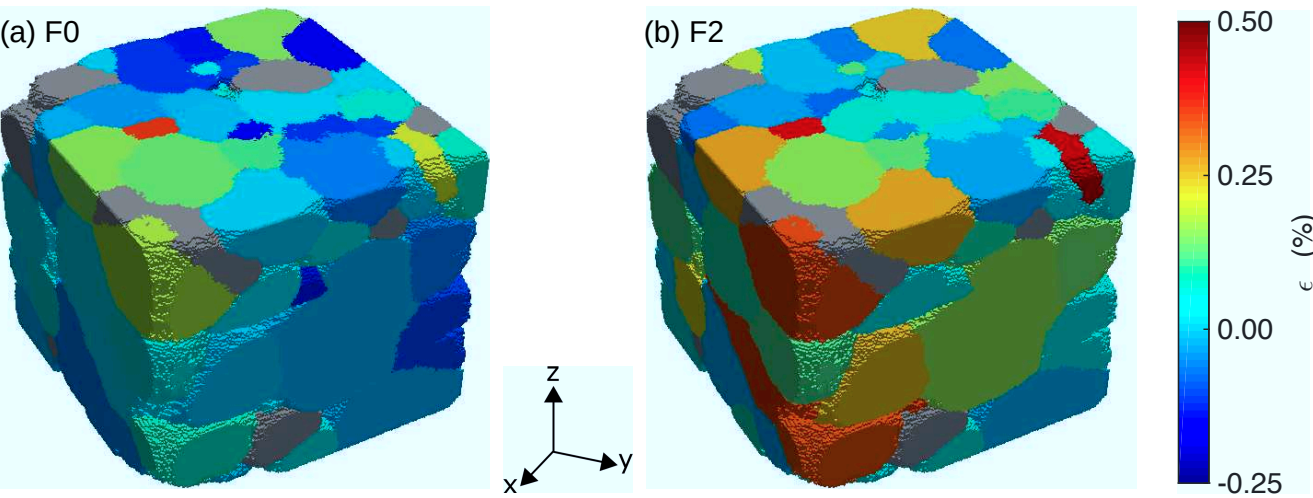

Paper III: Quantitative grain-scale ferroic domain volume fractions and domain switching strains from threedimensional X-ray diffraction data

Jette Oddershede, **Marta Majkut**, Qinghua Cao, Søren Schmidt, Jonathan P. Wright, Peter Keneseid and John E. Daniels

JOURNAL OF APPLIED CRYSTALLOGRAPHY
ISSN 1600-5767

Quantitative grain-scale ferroic domain volume fractions and domain switching strains from three-dimensional X-ray diffraction data

Jette Oddershede,[a]* Marta Majkut,[a] Qinghua Cao,[b] Søren Schmidt,[a] Jonathan P. Wright,[c] Peter Kenesei[d] and John E. Daniels[b]

[a]NEXMAP, DTU Physics, 2800 Kongens Lyngby, Denmark, [b]School of Materials Science and Engineering, UNSW Australia, Sydney, NSW 2052, Australia, [c]European Synchrotron Radiation Facility, Grenoble, BP-220, France, and [d]1ID, Advanced Photon Source, Lemont, IL 60439, USA. *Correspondence e-mail: jeto@fysik.dtu.dk

Received 3 February 2015
Accepted 18 April 2015

Edited by D. Pandey, Indian Institute of Technology (Banaras Hindu University), Varanasi, India

Keywords: ferroic materials; domain volume fractions; grain-scale strain; three-dimensional X-ray diffraction.

A method for the extension of the three-dimensional X-ray diffraction technique to allow the extraction of domain volume fractions in polycrystalline ferroic materials is presented. This method gives access to quantitative domain volume fractions of hundreds of independent embedded grains within a bulk sample. Such information is critical to furthering our understanding of the grain-scale interactions of ferroic domains and their influence on bulk properties. The method also provides a validation tool for mesoscopic ferroic domain modelling efforts. The mathematical formulations presented here are applied to tetragonal coarse-grained $Ba_{0.88}Ca_{0.12}Zr_{0.06}Ti_{0.94}O_3$ and rhombohedral fine-grained $(0.82)Bi_{0.5}Na_{0.5}TiO_3$–$(0.18)Bi_{0.5}K_{0.5}TiO_3$ electroceramic materials. The fitted volume fraction information is used to calculate grain-scale non-180° ferroelectric domain switching strains. The absolute errors are found to be approximately 0.01 and 0.03% for the tetragonal and rhombohedral cases, which had maximum theoretical domain switching strains of 0.47 and 0.54%, respectively. Limitations and possible extensions of the technique are discussed.

1. Introduction

Bulk polycrystalline ferroic materials find a broad range of practical applications, such as AC transformer cores (ferromagnetics), superelastic constant-force springs (ferroelastics) and high-strain electromechanical actuators (ferroelectrics). All of these materials undergo a phase transformation to the ferroic state upon cooling or under the influence of a field, such as magnetic, electric or stress field. During the phase transformation, ferroic domains are formed within the material. The morphology of the resultant domain structures depends on many factors, including (but by no means limited to) the magnitude and crystallographic orientation of the ferroic order parameter, the polycrystalline microstructure, and the anisotropy of the driving field. This morphology is one of the key structural parameters that influence the bulk properties of ferroic materials, as these properties are governed by the movement of domain boundaries and their interactions with one another and with other microstructural defects. Furthermore, the discovery of functionality of domain walls (Seidel *et al.*, 2009) has opened new possibilities with regards to potential ferroic material properties. Characterization of domain structures in the bulk of polycrystalline ferroic materials is therefore critical to further understand and engineer properties of such materials. This paper concentrates on the measurement of non-180° ferroelectric domains, which possess a spontaneous strain; however, as discussed in §5, the

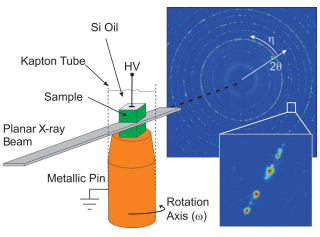

technique may be extended and applied in many other materials.

In the case of ferroelectric materials, domain information can be observed using a range of methods. A recent review article by Wu *et al.* (2015) provides an excellent overview. Optical microscopy, either with preferential etching of domain orientations or using polarized light, can distinguish certain types of domain structures intersecting the surface of a material. These surface images have been used to infer the three-dimensional domain structures in the bulk (Arlt & Sasko, 1980). Likewise, scanning probe techniques can also detect domain structures at the surface but have the additional advantage of being able to resolve ferroelectric polarization vectors (Gruverman *et al.*, 1995). Transmission electron microscopy can be used to observe domain structures at very small length scales and under *in situ* electric fields (Tan *et al.*, 2005) but is only applicable to very small sample sizes. A digital holography technique has been demonstrated to detect domain structures in three dimensions where volume-fraction information is also accessible (Zhi *et al.*, 2009); however, in this case the method is somewhat limited to single crystals with certain optical properties.

Another approach to gain information on domain processes in the bulk is to measure average domain populations amongst grain families using powder X-ray or neutron diffraction (Lupascu *et al.*, 2001; Hall *et al.*, 2004; Pramanick *et al.*, 2011). These methods have significantly advanced our understanding of the effect of non-180° ferroelectric domain wall motion on the properties of bulk electroceramics by allowing for *in situ* measurement of the rearrangement of domains under electric field and stress. Additionally, these methods have allowed for the characterization of general grain-orientation-dependent strains associated with non-180° ferroelectric domain wall motion and have been applied both statically and dynamically under an applied electric field (Wang *et al.*, 2014) and stress (Harrison, 2004).

None of these methods, however, provide access to volume fraction information from isolated grains within bulk polycrystals, leaving remaining questions as to the role of local grain neighbourhoods in determining the bulk properties of ferroic polycrystals.

Here we demonstrate the collection and analysis of three-dimensional X-ray diffraction (3D-XRD) data to obtain the domain volume fractions resolved at the grain scale from within a bulk electroceramic. While anomalous scattering methods have been used to resolve mechanisms of 180° ferroelectric domain switching (Azimonte *et al.*, 2010), the present method is only sensitive to non-180° ferroelectric domain volume fraction changes. These changes give rise to an induced non-180° ferroelectric domain switching strain, the magnitude of which is calculated here for both tetragonal and rhombohedral symmetries. The methods demonstrated are by no means limited to the case of electroceramics. They can be applied to all ferroic materials that possess a spontaneous strain, which results in the separation of scattered intensity from domain components in diffraction space. Possible extensions to the data collection methods can be envisioned where the requirement for a spontaneous strain need not be fulfilled. For example, using neutrons with polarization analysis would allow for the assignment of magnetic domain orientations within ferromagnetic materials. Likewise, resolving all ferroelectric domains without a coupled spontaneous strain could potentially be achieved using anomalous or polarized X-ray scattering.

2. Experimental details

Details of the materials processing for the specific compositions used are provided in subsequent sections. Samples of suitable geometry were cut from bulk polycrystalline ceramics in a rectangular shape. Gold electrodes were sputtered onto two opposing surfaces. The samples were then placed with an electrode surface in contact with a brass pin and electrically contacted using silver paint. A top electrode wire was connected using silver paint and the sample encapsulated in a 1 mm-diameter Kapton tube filled with silicone oil. Such a setup allows the application of high electric fields without the risk of dielectric breakdown around the sample edges (Daniels *et al.*, 2009).

The 3D-XRD method allows for the indexing of many individual grains from a bulk material and gives direct access to grain-resolved information on position, orientation, volume and strain (Poulsen *et al.*, 2001; Poulsen, 2004; Juul Jensen *et al.*, 2006; Oddershede *et al.*, 2010; Bernier *et al.*, 2011; Sørensen *et al.*, 2012). A schematic diagram of the 3D-XRD setup that allows for *in situ* electrical loading and resulting diffraction patterns is shown in Fig. 1. The method requires that the X-ray beam illuminates a limited number of grains at a given time. The total number of grains is a function of (1) the beam size, (2) the sample grain size and (3) the sample thickness. Thus, these parameters need to be optimized in order to obtain scattering patterns appropriate for analysis. To probe a large fraction of reciprocal space for each grain, the sample is rotated around the common rotation and poling axis ω in steps

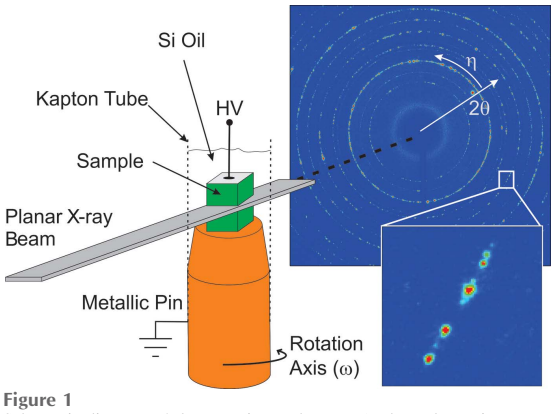

Figure 1
Schematic diagram of the experimental setup. A planar beam intersects the sample giving rise to 'spotty' diffraction rings owing to the limited number of grains sampled. A single image is obtained for each rotational increment $\Delta\omega$.

of $\Delta\omega$. In the ideal setup, the beam width is larger than the sample cross section such that the illuminated volume contains the same grains throughout the full rotation of the sample. However, many ferroelectric materials of interest have grain sizes less than 5 µm, limiting the maximum sample cross section for full illumination to approximately 100 µm or less. Such samples can be difficult to produce, so it is often necessary to reduce the beam width in order to limit the number of overlapping diffraction spots.

The collected sequences of diffraction images were analysed using the *Fable* software package (http://sourceforge.net/p/fable/wiki/Home/). The first step in the analysis procedure is to identify the coordinates $(2\theta, \eta, \omega)$ of all observed diffraction spots, where 2θ refers to the scattering angle (radial direction on the detector), η the azimuthal position on the detector and ω the rotation angle of the sample (see Fig. 1 for reference). In the subsequent indexing step, performed using *GrainSpotter* (Schmidt, 2014), the diffraction spots are assigned to individual grains, and the orientations and positions of these grains are refined. The version of *GrainSpotter* used for the present study only considers grains with a high completeness in terms of the ratio of the number of assigned to expected reflections within specified tolerances in 2θ, η and ω. It does not allow grains to share reflections, and since many reflections are in fact shared between ferroelastic domains, this in practice means that in most cases only one domain from each grain will be indexed. The results from the indexing include a list of grain orientations, positions and corresponding reflections. These, along with the collected sequence of diffraction images, comprise the input for the domain volume fitting algorithm.

3. Algorithm details

3.1. Resolving ferroelastic domain volume fractions

Individual peak families from a given grain are extracted from the data volume (*hkl* indices refer to the primitive cubic unit cell with $a \simeq 4$ Å). For the three non-180° tetragonal domains d_{200}, d_{020} and d_{002} the {002} reflections carry information about the domain volume fractions v_{200}, v_{020} and v_{002}, whereas the {111} reflections can be used to extract domain volume fractions $v_{\bar{1}11}$, $v_{1\bar{1}1}$, $v_{11\bar{1}}$ and v_{111} for the four non-180° rhombohedral domains $d_{\bar{1}11}$, $d_{1\bar{1}1}$, $d_{11\bar{1}}$ and d_{111}. Each reflection is then integrated into a radial profile along 2θ, and the resulting peaks are fitted using two Gaussian peak functions centred at $2\theta_{\rm min}$ and $2\theta_{\rm max}$. The intensities $I(2\theta_{\rm min})$ and $I(2\theta_{\rm max})$ of the two Gaussian peaks are then corrected for the Lorentz and polarization factors. Thereafter, they are proportional to the sum of domain volumes from particular domain variants. For instance, in the case of rhombohedral symmetry, the volume fraction $v_{11\bar{1}}$ of domain $d_{11\bar{1}}$ must equal the ratio of $I^{11\bar{1}}(2\theta_{\rm min})$ to the total intensity $I^{11\bar{1}}_{\rm tot} = I^{11\bar{1}}(2\theta_{\rm min}) + I^{11\bar{1}}(2\theta_{\rm max})$ for each of the $11\bar{1}$ and $\bar{1}11$ reflections. This assumes that all variants of the peak family have the same scattering factors, which is considered a reasonable assumption given that the distortion away from cubic is less than 1% for the sample materials in this study (see §4).

3D-XRD experiments with *in situ* electrical loading typically cover an ω rotation range of 320–340° because the support for the top electrode connection shadows part of the incoming and diffracted beams. Thus, most reflections are measured twice (on the left and right side of the detector). Including Friedel pairs, this gives up to four observations for each domain volume fraction. This enables us to set up a least-squares fit of the domain volume fractions for individual grains. For tetragonal symmetry the residual χ^2 that we need to minimize is defined as

$$\chi^2_{\rm tetr} = \sum_{t=(200,020,002)} \sum_{i=1}^{n(t)} \frac{1}{w_{t,i}} \left[v_t - \frac{I^{t,i}(2\theta_{\rm min})}{I^{t,i}_{\rm tot}} \right]^2, \qquad (1)$$

whereas for rhombohedral symmetry we have

$$\chi^2_{\rm rh} = \sum_{t=(\bar{1}11,1\bar{1}1,11\bar{1},111)} \sum_{i=1}^{n(t)} \frac{1}{w_{t,i}} \left[v_t - \frac{I^{t,i}(2\theta_{\rm min})}{I^{t,i}_{\rm tot}} \right]^2. \qquad (2)$$

Here the sum over i runs over the number of observations $[0 \leq n(t) \leq 4]$ of each reflection type t. In order to constrain the sum of volume fractions to unity we replace v_{002} by $1 - v_{200} - v_{020}$ in $\chi^2_{\rm tetr}$, and v_{111} by $1 - v_{\bar{1}11} - v_{1\bar{1}1} - v_{11\bar{1}}$ in $\chi^2_{\rm rh}$. The weights $w_{t,i}$ can be set to weight all observed reflections equally ($w_{t,i} = 1$), to compensate for the different number of observations of each type $[w_{t,i} = n(t)]$ or to down-weight outlier intensities, caused for example by overlapping reflections from different grains or by the grain of interest rotating partially out of the illuminated volume if the beam width is smaller than the sample cross section. This can for instance be done by using as $w_{t,i}$ the absolute deviation of $I^{t,i}_{\rm tot}$ either from the median over all reflections assigned to the grain or from the median over the type t subset of these reflections.

It is possible to minimize equation (1) if reflections corresponding to two of the three possible tetragonal domains are measured, and likewise for equation (2) with three of the four rhombohedral domains represented. This allows a result to be obtained even when given reflections are missing from the data set owing to incomplete sampling of reciprocal space. The actual minimization of the residuals is performed by means of the Levenberg–Marquardt algorithm (Levenberg, 1944; Marquardt, 1963). The output is a vector containing the domain volume fractions, either $\mathbf{v}_{\rm tetr} = (v_{200}, v_{020}, 1 - v_{200} - v_{020})$ or $\mathbf{v}_{\rm rh} = (v_{\bar{1}11}, v_{1\bar{1}1}, v_{11\bar{1}}, 1 - v_{\bar{1}11} - v_{1\bar{1}1} - v_{11\bar{1}})$, and the corresponding covariance matrix, $\Sigma_{\rm tetr}$ or $\Sigma_{\rm rh}$, respectively.

3.2. Calculating strain along the electric field vector

The strain along the electric field vector resulting from non-180° ferroelectric domain switching can be calculated once the domain volume fractions have been obtained as outlined by Hall and co-workers for tetragonal (Hall *et al.*, 2005) and later also for rhombohedral (Hall *et al.*, 2006) symmetry. The error estimate on a domain switching strain can be propagated from the covariances. In the following we let $\mathbf{l} = (l_1, l_2, l_3)$ be a unit vector along the poling direction in the crystal reference frame, and reproduce the definitions of the poling strain along $\mathbf{l}$, $\varepsilon_{\rm p}$.

3.2.1. Tetragonal symmetry. For tetragonal symmetry the poling strain along **l** is defined as (Hall *et al.*, 2005)

$$\varepsilon_p = \left(\frac{c-a}{a_0}\right)\left(v_{200}l_1^2 + v_{020}l_2^2 + v_{002}l_3^2 - \frac{1}{3}\right) = \left(\frac{c-a}{a_0}\right)\left[(v_{200}, v_{020}, v_{002})\cdot \mathbf{L}_{tetr} - \frac{1}{3}\right], \quad (3)$$

where c and a are the tetragonal lattice parameters, and a_0 is the lattice parameter of the cubic phase. Without an independent measure of the cubic lattice parameter one can use $a_0 = (ca^2)^{1/3}$, thus assuming no volume change at the non-ferroic to ferroic phase transition. For **l** = ⟨111⟩ or $v_{200} = v_{020} = v_{002} = 1/3$ we get $\varepsilon_p = 0$ because $v_{200} + v_{020} + v_{002} = 1$ and $l_1^2 + l_2^2 + l_3^2 = 1$. The maximum poling strain of $2(c-a)/(3a_0)$ is obtained for a single domain with ⟨100⟩ aligned along the electric field direction, while the minimum possible value of ε_p is $(a-c)/(3a_0)$. The error estimate on the poling strain can then be propagated as

$$\sigma(\varepsilon_p) = \left|\frac{c-a}{a_0}\right|\left[\left(l_1^2, l_2^2, l_3^2\right)\Sigma_{tetr}\left(l_1^2, l_2^2, l_3^2\right)^T\right]^{1/2} = \left|\frac{c-a}{a_0}\right|\left(\mathbf{L}_{tetr}\Sigma_{tetr}\mathbf{L}_{tetr}^T\right)^{1/2}, \quad (4)$$

assuming that the experimental error on the orientation of the electric field direction is negligible.

3.2.2. Rhombohedral symmetry. For rhombohedral symmetry the poling strain along **l** is defined as (Hall *et al.*, 2006)

$$\varepsilon_p = 2\gamma\left[v_{\bar{1}11}(-l_1l_2 - l_1l_3 + l_2l_3) + v_{1\bar{1}1}(-l_1l_2 + l_1l_3 - l_2l_3) + v_{11\bar{1}}(l_1l_2 - l_1l_3 - l_2l_3) + v_{111}(l_1l_2 + l_1l_3 + l_2l_3)\right] = 2\gamma(v_{\bar{1}11}, v_{1\bar{1}1}, v_{11\bar{1}}, v_{111})\cdot\mathbf{L}_{rh}, \quad (5)$$

where $2\gamma = \pi(1/2 - \alpha_{rh}/180^\circ)$ is the maximum poling strain, obtained for a single domain with a ⟨111⟩ axis aligned along the electrical field direction. For **l** = ⟨100⟩ or $v_{\bar{1}11} = v_{1\bar{1}1} = v_{11\bar{1}} = v_{111} = 1/4$ we get $\varepsilon_p = 0$, while the minimum value of ε_p is $-\gamma$. The error estimated on the poling strain is then given as

$$\sigma(\varepsilon_p) = 2\gamma\left(\mathbf{L}_{rh}\Sigma_{rh}\mathbf{L}_{rh}^T\right)^{1/2}, \quad (6)$$

where $\mathbf{L}_{rh}$ is defined in equation (5) and again the experimental error on the electric field direction is ignored.

4. Applications

The maximum poling strain possible for a given crystal symmetry and grain orientation is obtained when the grain texture is saturated, meaning that the entire grain is transformed to the domain variant with a polarization axis (and corresponding spontaneous strain) most favourably oriented relative to the applied field direction. The maximum poling strain is therefore also termed the theoretical saturated strain. Fig. 2 shows a simulation of theoretical saturated strains for 10 000 randomly oriented cubic grains that are assumed to transform to either tetragonal or rhombohedral symmetry. The tetragonal and rhombohedral lattice parameters are taken to be the same as in the two experiments described below on samples of the same respective crystallographic symmetries.

4.1. Material 1: tetragonal coarse-grained BCZT

4.1.1. Sample preparation. Samples of $Ba_{0.88}Ca_{0.12}Zr_{0.06}Ti_{0.94}O_3$ (BCZT) were produced by the mixed oxide method. Details of this material system and the resulting electromechanical properties can be found elsewhere (Liu & Ren, 2009; Li *et al.*, 2010). The resulting grain size of the samples was approximately 20–40 µm. A sample was cut and polished into a cuboid shape of dimensions 300 × 300 × 300 µm and prepared for *in situ* measurements as outlined in §2.

4.1.2. Data acquisition. X-ray diffraction experiments were performed at beamline 1-ID-E of the Advanced Photon Source, Argonne National Laboratory. A beam energy of 61.332 keV (Yb *K* edge) was focused and trimmed to a planar beam of dimensions 600 µm in width × 30 µm in height at the sample position, thus illuminating the entire sample cross section. The sample was then rotated around ω while data were collected over 2 × 166° in 0.1° integration angles with an exposure time of 0.2 s per image. A GE 41RT detector with 2048 × 2048 pixels of 200 × 200 µm was employed at a sample-to-detector distance of 1560 mm. Four 30 µm-thick layers perpendicular to the common electric field and rotation axis were collected with an interlayer spacing of 15 µm, both in the initial unpoled state and in the remnant state, after the sample had been electrically poled with a field of 1.5 kV mm^{-1}.

4.1.3. Grain indexing and selection. From the powder diffraction pattern of the same sample the tetragonal lattice parameters of the BCZT composition were refined to a = 3.993 Å and c = 4.021 Å. *GrainSpotter* (Schmidt, 2014) was then used to index 150–160 tetragonal domains in every illuminated layer of the sample. A matching procedure was performed to identify exactly one domain orientation for each grain and to track this orientation from one layer to the next. Because the average grain size is larger than the beam height, reflection intensities corresponding to each grain across the four illuminated layers were then compared to exclude partly illuminated grains with maximum intensities in the top or bottom layers. This leaves 105 grains centrally located in the volume of interest for further analysis.

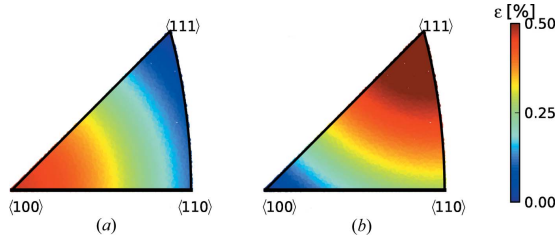

Figure 2
Theoretical saturated domain texture strains for 10 000 randomly oriented grains with (*a*) tetragonal symmetry, a = 3.993 Å, c = 4.021 Å and (*b*) rhombohedral symmetry, $\alpha_{rh} = 89.69^\circ$. For these conditions the maximum poling strain is $\varepsilon_p^{sat} = 0.466\%$ and $\varepsilon_p^{sat} = 0.547\%$ for the tetragonal and rhombohedral cases, respectively.

Table 1
Details of four selected grains for which the domain volume fraction algorithm has been employed.

T_{100} and T_{111} are from coarse-grained tetragonal BCZT (§4.1), while R_{100} and R_{111} are from fine-grained rhombohedral BNKT (§4.2).

	ε_p (%)	ε_p^{sat} (%)	α_{200} (°)	α_{020} (°)	α_{002} (°)	v_{200}	v_{020}	v_{002}
T_{100}	0.064 (3)	0.46	84	89	7	0.203 (4)	0.370 (4)	0.427 (5)
T_{111}	0.0035 (2)	0.03	58	54	52	0.322 (4)	0.224 (3)	0.453 (4)

	ε_p (%)	ε_p^{sat} (%)	$\alpha_{\bar{1}11}$ (°)	$\alpha_{\bar{1}\bar{1}1}$ (°)	$\alpha_{11\bar{1}}$ (°)	α_{111} (°)	$v_{\bar{1}11}$	$v_{\bar{1}\bar{1}1}$	$v_{11\bar{1}}$	v_{111}
R_{100}	−0.07 (1)	0.21	70	40	58	54	0.41 (2)	0.07 (2)	0.30 (5)	0.22 (5)
R_{111}	0.28 (2)	0.52	64	67	81	11	0.23 (3)	0.14 (2)	0.00 (6)	0.63 (3)

To demonstrate the algorithm, two of the 105 grains in the remnant state were selected. These grains have the electric field vector close to the crystallographic [100] (T_{100}) and [111] (T_{111}) axes and are thus expected to display high and low poling strains, respectively (*cf.* Fig. 2*a*). The resulting domain volume fractions and poling strains given in Table 1 are calculated as volume-weighted averages over grain slices from non-overlapping layers. Here the volume of a grain slice is calculated as the median over $I_{tot}^{t,i}$ for all corresponding reflections, while the error bar is estimated from the median absolute deviation of $I_{tot}^{t,i}$. The example reflections in Fig. 3 are from the layer where the slice volume of grain T_{100} was maximum.

4.1.4. Domain volume fitting. Fig. 3 shows the integrated reflections for grain T_{100}. The overall intensities are observed to be very consistent for all 12 measured reflections, and the same holds for the $I(2\theta_{min}):I_{tot}$ ratios for each domain type. On this basis this the weights $w_{t,i}$ of equation (1) range from 0.9 to 3.7, taking into account both the overall intensity consistency and the consistency within the group of reflections corresponding to a certain domain type. The absolute error bars on the resulting domain volume fractions and poling strain in Table 1 are less than 0.01%, and the fits for grain T_{111} are equally consistent.

4.2. Material 2: rhombohedral fine-grained BNKT

4.2.1. Sample preparation. Samples of $(0.82)Bi_{0.5}Na_{0.5}TiO_3$–$(0.18)Bi_{0.5}K_{0.5}TiO_3$ (BNKT) were produced by the mixed oxide route. Details of the synthesis method can be found elsewhere (Tran *et al.*, 2011). The resulting grain size of the samples was approximately 3–5 µm. A sample was cut and polished into a rectangular shape of dimensions 100 × 200 × 90 µm. Gold electrodes were sputtered onto two opposing 100 × 200 µm surfaces.

4.2.2. Data acquisition. X-ray diffraction experiments were performed at beamline ID11 of the European Synchrotron Radiation Facility. A beam energy of 78.395 keV (Pt *K* edge) was focused and trimmed to a planar beam of dimensions 50 µm in width × 5 µm in height at the sample position. During the rotation around ω data were collected over 2 × 160° in 0.25° integration angles with an exposure time of 5 s per image. A FReLoN detector (Labiche *et al.*, 2007) with 2048 × 2048 pixels of 50 × 50 µm was employed at a sample-to-detector distance of 496 mm. After the collection of an initial data set in the unpoled state, the sample was poled with an electric field of 4 kV mm^{-1} and a subsequent data set collected. Upon electrical poling the phase of the sample changed irreversibly from a pseudo-cubic to rhombohedral symmetry.

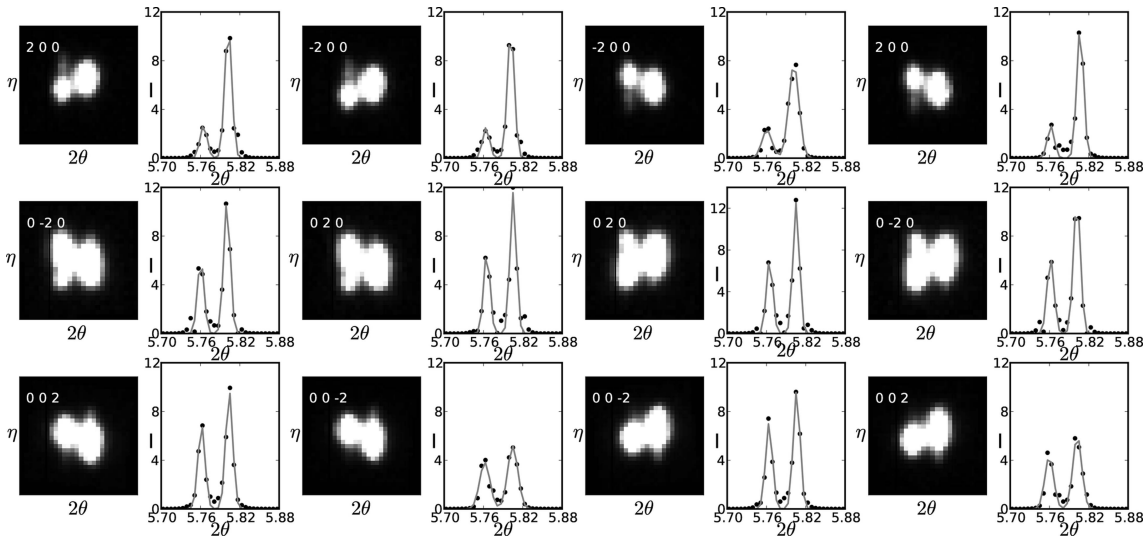

Figure 3
Reflections of the {002} family for a tetragonal grain of BCZT, marked as T_{100} in Table 1. The intensity scale for the integrated data has a maximum of 12 000. The dots represent the measured data and the lines are the Gaussian peak fits. It can be seen that $v_{200} < v_{020} < v_{002}$ as anticipated, since d_{002} is favourably aligned with its polarization axis approximately 7° from the electric field axis.

4.2.3. Grain indexing and selection. From the powder diffraction pattern of the same sample, the pseudo-cubic lattice parameter of BNKT in the unpoled state was refined to a = 3.905 Å, while the rhombohedral lattice parameters after poling were refined to a = 3.905 Å and α_{rh} = 89.69°. The orientations of the grains in the poled state were determined using *GrainSpotter* (Schmidt, 2014). Since the sample cross section is larger than the beam width, grains will move in and out of the beam. By using a high completeness cutoff in terms of the number of observed to expected reflections, the indexing can be limited to the approximately 500 grains that are located within the central part of the sample, which is illuminated throughout the rotation. Here the completeness criterion was set to only include grains where all 16 possible {001} and {002} reflections were present, since these do not split in the 2θ dimension for rhombohedral symmetry. From the 500 central grains, two grains with the poling axis close to the crystallographic [100] (R_{100}) and [111] (R_{111}) axes were selected for further analysis.

4.2.4. Domain volume fitting. The selected grains R_{100} and R_{111} fulfil the criterion that reflections corresponding to all four domain variants were observed. This was deemed necessary here, as opposed to the coarse-grained BCZT case, in order to fit consistent domain volume fractions in the presence of significant peak overlap. In the domain volume fraction minimization [equation (2)] the last 111 and the last two $1\bar{1}1$ reflections shown in Fig. 4 were down-weighted owing to the intensity offsets caused by significant peak overlap. The weights ranged from 0.2 to 7.7, an order of magnitude more than for BCZT, and they were only assigned on the basis of overall intensity consistency. A similar degree of inconsistency was observed for grain R_{111}. However, because of the volume weighting, the resulting absolute error bars on the poling strains of the rhombohedral grains R_{100} and R_{111} remain less than 0.03%.

4.3. Results

Table 1 summarizes the domain volume fractions, poling strains and corresponding error estimates for the four selected grains, T_{100}, T_{111}, R_{100} and R_{111}, described in the previous sections. Here α_{200}, α_{020} and α_{002} are defined as the angles between the electric field vector and the c axis of the tetragonal domains d_{200}, d_{020} and d_{002}, respectively. Likewise, the angles $\alpha_{\bar{1}11}$, $\alpha_{1\bar{1}1}$, $\alpha_{11\bar{1}}$ and α_{111} are defined between the electric field direction and the body diagonals of the respective rhombohedral domains $d_{\bar{1}11}$, $d_{1\bar{1}1}$, $d_{11\bar{1}}$ and d_{111}. If only the domain variant with the smallest corresponding angle is populated, $\varepsilon_p = \varepsilon_p^{sat}$ is obtained. For the tetragonal BCZT grains T_{100} and T_{111} the remnant poling strains are roughly an order of magnitude smaller than the theoretical saturated strains, and $\varepsilon_p(T_{100}) > \varepsilon_p(T_{111})$ as anticipated from Fig. 2(*a*). The rhombohedral grains display the opposite trend in poling strain, $\varepsilon_p(R_{100}) < \varepsilon_p(R_{111})$ [see Fig. 2(*b*)]. The overall remnant strain level in the rhombohedral BNKT sample is about half of the theoretical saturated strain level. Both this difference in strain level between the two samples and the orientation dependence of poling strains for the selected grains of the different symmetries are displayed in Fig. 5. The position of the grains in the stereographic triangle corresponds to the orientation relative to the electric field vector, and the colour code is the observed poling strain due to domain wall motion.

Considering the difference in internal consistency between reflections assigned to a grain of coarse-grained tetragonal BCZT (Fig. 3) and one of fine-grained rhombohedral BNKT

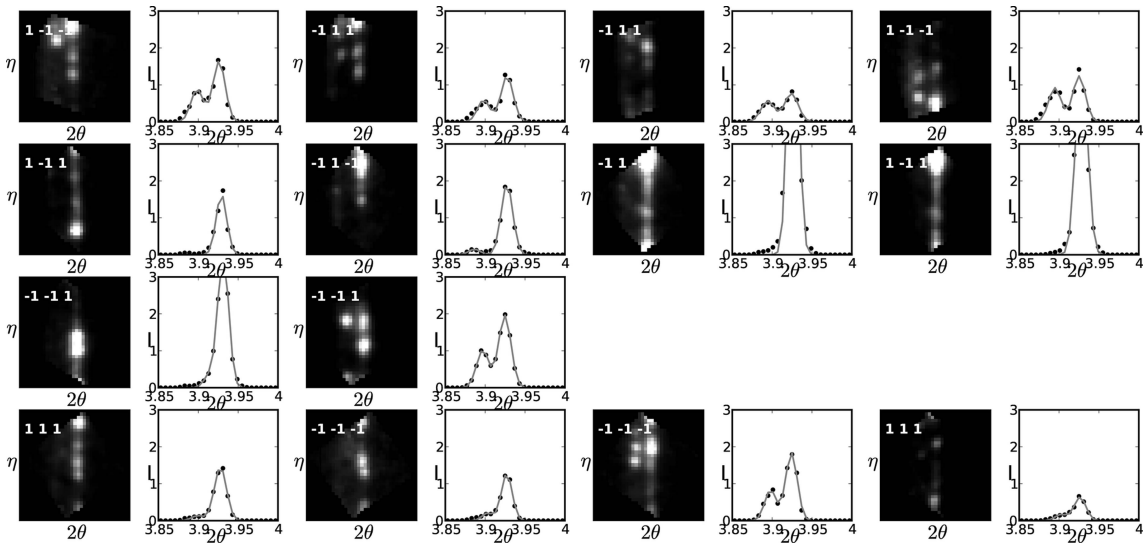

Figure 4
Reflections of the {111} family for a rhombohedral grain of BNKT, marked as R_{100} in Table 1. The intensity scale has a maximum of 3000. Significant splitting is observed for all domain types except $d_{1\bar{1}1}$, consistent with a low volume fraction, $v_{1\bar{1}1} = 0.07\,(2)$, as stated in Table 1.

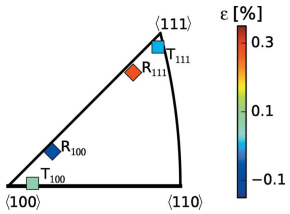

Figure 5
Orientations and poling strains for the four selected grains in Table 1. For the tetragonal grains the maximum poling strain is observed when the electric field vector is close to a ⟨100⟩ axis, while the maximum poling strain for the rhombohedral grains is when the electric field direction is aligned close to a ⟨111⟩ axis (see Fig. 2).

(Fig. 4), it is not surprising that the average absolute error bar on the poling strain for all grains, not just the ones selected in Table 1, is approximately 0.01% for BCZT and 0.03% for BNKT. The reason for this is most likely the increased number of diffraction spots in the fine-grained BNKT compared to coarse-grained BCZT, which increases the likelihood of peak overlap and hence erroneous peak intensities. However, as noted above, the remnant strains observed in the rhombohedral BNKT are also substantially larger than in the tetragonal BCZT, so the relative errors bars in each case are comparable.

5. Discussion

The measurement method demonstrated gives unique access to grain-scale domain volume fraction and resultant non-180° ferroelectric domain switching strains. This information can be used to advance our understanding of ferroic materials at the grain scale and will be critical for experimental verification of mesoscopic materials modelling efforts, for instance phase field models, which have increasing relevance to the study of ferroic systems (Potnis *et al.*, 2011).

The examples in §4 demonstrate that peak overlap is the main limitation of the present algorithm for fitting individual domain volume fractions. In order to avoid possible experimental artefacts from the use of this method, the following factors should be considered when measuring from coarse- and fine-grained materials:

(1) Grain sizes > 10 µm

(*a*) Use a beam height that is roughly double the average grain size and consider at least five non-overlapping layers to get sufficient statistics from fully embedded grains.

(2) Grains sizes < 10 µm

(*a*) Use a sample with a smaller cross section, ideally smaller than the beam width, though this presents its own experimental difficulties, particularly for *in situ* measurements owing to processing difficulties.

(*b*) Scanning beam methods (Bonnin *et al.*, 2014) may be employed in order to also overcome the total number of grains in the beam for any particular orientation.

Further advances of the method can be envisioned. Three significant pieces of information are missing from such an analysis: (1) the spatial distribution of domains within the grain, (2) the orientation relationships between domains within grains and (3) the piezoelectric or elastic compliance strain response of the individual domain variants. It is possible that the spatial distribution of domains could be extracted from the current method if it is combined with space-filling grain maps measured using a high-resolution near-field detector (Schmidt *et al.*, 2008; Ludwig *et al.*, 2008, 2009; Li *et al.*, 2012; Reischig *et al.*, 2013; Pokharel *et al.*, 2014). However, here the minimum domain size would probably have to be of the order of 10 µm in order to resolve such structures. Additional X-ray microscopy methods are being developed, which allow for much higher spatial resolution of sub-grain structures in three dimensions from bulk materials (Simons *et al.*, 2015). It is envisioned that such methods may progress towards 50 nm resolution with improved source and optics characteristics, opening up many opportunities for the study of domain structures and their influence on properties in bulk polycrystalline materials.

The orientation relationships between domains within a grain may also be obtained from the far-field 3D-XRD data (Varlioglu *et al.*, 2010), as the domains are simply entities with distinct orientations and can be indexed in the same way as twins in metallic materials (Aydıner *et al.*, 2009; Oddershede *et al.*, 2011; Bieler *et al.*, 2014; Abdolvand *et al.*, 2015). However, the diffraction spots arising from ferroelastic domains of the same grain in electroceramic materials are not nearly as well separated in 2θ, η and ω as the diffraction spots of parent and twin pairs in previously measured metallic materials, and many reflections are in fact shared between two or more domains.

In addition to the non-180° domain switching strains calculated here, the system will also undergo elastic strains due to the intrinsic piezoelectric effect and compliance strains due to the deformation of surrounding grains. Observing these elastic strain responses of the individual domain variants within the measured grains could also potentially be done if the above two extensions could be achieved. This would allow unprecedented information on the response of ferroic materials in the bulk.

The mathematical formulation and application examples presented here have focused on tetragonal and rhombohedral crystallographic symmetry. However, the algorithm for determining domain volume fractions can be extended to work for orthorhombic domain structures by investigating the threefold splitting in any pseudocubic family of reflections $\{hkl\}$ except those fulfilling $|h| = |k| = |l|$, or for lower symmetries by using combinations of reflection sets. Similarly, extensions to account for domain volume fraction changes in mixed phase systems could be achieved by considering multiple reflection families.

6. Conclusions and outlook

A method has been developed to allow for the measurement of domain volume fractions and associated domain switching strains from isolated grains within a bulk polycrystalline material. The method was demonstrated on two contrasting materials, namely, a coarse-grained (approximately 50 µm)

BCZT and a fine-grained (approximately 3 μm) BNKT. In these cases, absolute domain switching strain errors of 0.01 and 0.03% were found, respectively. It is hoped that the currently presented method will be extended in the future to allow studies incorporating not only domain volume fractions but also spatial distributions, orientation distributions and elastic deformation of individual ferroelastic domains. The methods presented are extendable to multiple ferroic material types. They have the potential to enhance our understanding of ferroic behaviour in the polycrystalline state and will provide critical mesoscale information for the confirmation and/or constraint of modelling efforts at these length scales.

Acknowledgements

The authors acknowledge support from the Danish Independent Research Council | Technology and Production Sciences case No. 12-127449 and Australian Research Council Discovery Project DP120103968. The Danish Independent Research Council | Natural Sciences is acknowledged for covering expenses in relation to the synchrotron experiment (through Danscatt). This research used resources of the Advanced Photon Source, a US Department of Energy (DOE) Office of Science User Facility operated for the DOE Office of Science by Argonne National Laboratory under contract No. DE-AC02-06CH11357. The European Synchrotron Radiation Facility (MA-1919) and Advanced Photon Source (GUP-32411) are acknowledged for granting beamtime for the experiments. JED acknowledges support from an Australian Institute of Nuclear Science and Engineering research fellowship. Finally the authors wish to thank Julia Glaum, UNSW Australia, and Wook Jo, UNIST, South Korea, for providing the sample materials for the current study.

References

Abdolvand, H., Majkut, M., Oddershede, J., Schmidt, S., Lienert, U., Diak, B. J., Withers, P. J. & Daymond, M. R. (2015). *Int. J. Plasticity*, **70**, 77–97.
Arlt, G. & Sasko, P. (1980). *J. Appl. Phys.* **51**, 4956–4960.
Aydıner, C. C., Bernier, J. V., Clausen, B., Lienert, U., Tomé, C. N. & Brown, D. W. (2009). *Phys. Rev. B*, **80**, 024113.
Azimonte, C., Granado, E., Terashita, H., Park, S. & Cheong, S. W. (2010). *Phys. Rev. B*, **81**, 012103.
Bernier, J. V., Barton, N. R., Lienert, U. & Miller, M. P. (2011). *J. Strain Anal. Eng. Des.* **46**, 527–547.
Bieler, T. R., Wang, L., Beaudoin, A. J., Kenesei, P. & Lienert, U. (2014). *Met. Mater. Trans. A*, **45**, 109–122.
Bonnin, A., Wright, J. P., Tucoulou, R. & Palancher, H. (2014). *Appl. Phys. Lett.* **105**, 084103.
Daniels, J. E., Pramanick, A. & Jones, J. L. (2009). *IEEE Trans. Ultrason. Ferroelectr. Freq. Control*, **56**, 1539–1545.
Gruverman, A., Kolosov, O., Hatano, J., Takahashi, K. & Tokumoto, H. (1995). *J. Vac. Sci. Technol. B*, **13**, 1095–1099.
Hall, D. A., Steuwer, A., Cherdhirunkorn, B., Mori, T. & Withers, P. J. (2004). *J. Appl. Phys.* **96**, 4245–4252.
Hall, D. A., Steuwer, A., Cherdhirunkorn, B., Mori, T. & Withers, P. J. (2006). *Acta Mater.* **54**, 3075–3083.
Hall, D. A., Steuwer, A., Cherdhirunkorn, B., Withers, P. J. & Mori, T. (2005). *Mater. Sci. Eng. A*, **409**, 206–210.
Harrison, R. J. (2004). *J. Appl. Phys.* **95**, 1706–1717.
Juul Jensen, D., Lauridsen, E. M., Margulies, L., Poulsen, H. F., Schmidt, S., Sørensen, H. O. & Vaughan, G. M. B. (2006). *Mater. Today*, **9**, 18–25.
Labiche, J.-C., Mathon, O., Pascarelli, S., Newton, M. A., Ferre, G. G., Curfs, C., Vaughan, G., Homs, A. & Carreiras, D. F. (2007). *Rev. Sci. Instrum.* **78**, 091301.
Levenberg, K. (1944). *Q. Appl. Math.* **2**, 164–168.
Li, S. F., Lind, J., Hefferan, C. M., Pokharel, R., Lienert, U., Rollett, A. D. & Suter, R. M. (2012). *J. Appl. Cryst.* **45**, 1098–1108.
Li, W., Xu, Z., Chu, R., Fu, P. & Zang, G. (2010). *Mater. Lett.* **64**, 2325–2327.
Liu, W. & Ren, X. (2009). *Phys. Rev. Lett.* **103**, 257602.
Ludwig, W., King, A., Reischig, P., Herbig, M., Lauridsen, E. M., Schmidt, S., Proudhon, H., Forest, S., Cloetens, P., du Roscoat, S. R., Buffière, J., Marrow, T. & Poulsen, H. (2009). *Mater. Sci. Eng. A*, **524**, 69–76.
Ludwig, W., Schmidt, S., Lauridsen, E. M. & Poulsen, H. F. (2008). *J. Appl. Cryst.* **41**, 302–309.
Lupascu, D. C., Hoffmann, M. J., Hammer, M. & Endriss, A. (2001). *Acta Mater.* **49**, 1301–1310.
Marquardt, D. (1963). *J. Soc. Ind. Appl. Math.* **11**, 431–441.
Oddershede, J., Schmidt, S., Poulsen, H. F., Margulies, M., Wright, J., Moscicki, M., Reimers, W. & Winther, G. (2011). *Mater. Charact.* **62**, 651–660.
Oddershede, J., Schmidt, S., Poulsen, H. F., Sørensen, H. O., Wright, J. & Reimers, W. (2010). *J. Appl. Cryst.* **43**, 539–549.
Pokharel, R., Lind, J., Kanjarla, A., Lebensohn, R., Li, S. F., Kenesei, P., Suter, R. M. & Rollett, A. D. (2014). *Annu. Rev. Condens. Matter Phys.* **5**, 317–346.
Potnis, P. R., Tsou, N.-T. & Huber, J. E. (2011). *Materials*, **4**, 417–447.
Poulsen, H. F. (2004). *Three-Dimensional X-ray Diffraction Microscopy. Mapping Polycrystals and Their Dynamics*, Tracts in Modern Physics, Vol. 205. Berlin: Springer-Verlag.
Poulsen, H. F., Nielsen, S. F., Lauridsen, E. M., Schmidt, S., Suter, R. M., Lienert, U., Margulies, L., Lorentzen, T. & Juul Jensen, D. (2001). *J. Appl. Cryst.* **34**, 751–756.
Pramanick, A., Damjanovic, D., Daniels, J. E., Nino, J. C. & Jones, J. L. (2011). *J. Am. Ceram. Soc. Feature Art.* **94**, 293–309.
Reischig, P., King, A., Nervo, L., Viganó, N., Guilhem, Y., Palenstijn, W. J., Batenburg, K. J., Preuss, M. & Ludwig, W. (2013). *J. Appl. Cryst.* **46**, 297–311.
Schmidt, S. (2014). *J. Appl. Cryst.* **47**, 276–284.
Schmidt, S., Olsen, U. L., Poulsen, H. F., Sørensen, H. O., Lauridsen, E. M., Margulies, L., Maurice, C. & Juul Jensen, D. (2008). *Scr. Mater.* **59**, 491–494.
Seidel, J. *et al.* (2009). *Nat. Mater.* **8**, 229–234.
Simons, H., King, A., Ludwig, W., Detlefs, C., Pantleon, W., Schmidt, S., Snigireva, I., Snigirev, A. & Poulsen, H. F. (2015). *Nat. Commun.* **6**, 6098.
Sørensen, H. O., Schmidt, S., Wright, J. P., Vaughan, G. B. M., Techert, S., Garman, E. F., Oddershede, J., Davaasambuu, J., Paithankar, K. S., Gundlach, C. & Poulsen, H. F. (2012). *Z. Kristallogr.* **227**, 63–78.
Tan, X. L., He, H. & Shang, J. K. (2005). *J. Mater. Res.* **20**, 1641–1653.
Tran, V. D. N., Han, H.-S., Yoon, C.-H., Lee, J.-S., Jo, W. & Rödel, J. (2011). *Mater. Lett.* **65**, 2607–2609.
Varlioglu, M., Lienert, U., Park, J.-S., Jones, J. L. & Üstündag, E. (2010). *Texture Stress Microstruct.* **2010**, 910793.
Wang, Z., Webber, K. G., Hudspeth, J. M., Hinterstein, M. & Daniels, J. E. (2014). *Appl. Phys. Lett.* **105**, 161903.
Wu, H., Li, L., Liang, L.-Z., Liang, S., Zhu, Y.-Y. & Zhu, X.-H. (2015). *J. Eur. Ceram. Soc.* **35**, 411–441.
Zhi, Y., Liu, D., Sun, J., Yan, A., Zhou, Y., Luan, Z., Dai, E., Liu, L. & Qu, W. (2009). *J. Appl. Phys.* **105**, 024106.

Paper IV: Heterogeneous grain-scale response in ferroic polycrystals under electric field

John E. Daniels, **Marta Majkut**, Qingua Cao, Søren Schmidt, Jon Wright, Wook Jo & Jette Oddershede

SCIENTIFIC REPORTS

OPEN

Heterogeneous grain-scale response in ferroic polycrystals under electric field

Received: 18 December 2015
Accepted: 22 February 2016
Published: 09 March 2016

John E. Daniels[1], Marta Majkut[2], Qingua Cao[1], Søren Schmidt[2], Jon Wright[3], Wook Jo[4] & Jette Oddershede[2]

Understanding coupling of ferroic properties over grain boundaries and within clusters of grains in polycrystalline materials is hindered due to a lack of direct experimental methods to probe the behaviour of individual grains in the bulk of a material. Here, a variant of three-dimensional X-ray diffraction (3D-XRD) is used to resolve the non-180° ferroelectric domain switching strain components of 191 grains from the bulk of a polycrystalline electro-ceramic that has undergone an electric-field-induced phase transformation. It is found that while the orientation of a given grain relative to the field direction has a significant influence on the phase and resultant domain texture, there are large deviations from the average behaviour at the grain scale. It is suggested that these deviations arise from local strain and electric field neighbourhoods being highly heterogeneous within the bulk polycrystal. Additionally, the minimisation of electrostatic potentials at the grain boundaries due to interacting ferroelectric domains must also be considered. It is found that the local grain-scale deviations average out over approximately 10–20 grains. These results provide unique insight into the grain-scale interactions of ferroic materials and will be of value for future efforts to comprehensively model these and related materials at that length-scale.

Piezoelectric materials offer the ability to directly couple electrical charge and mechanical strain, and have a vast range of technological applications. Recent progress towards the development of lead-free piezoelectric materials to meet new legislative requirements[1] has directed detailed investigations of the strain mechanisms in both existing lead-containing and promising lead-free systems.

The magnitude of electric-field-induced strain possible in a given material is often a limiting factor for device design, particularly for actuators. Lead-based and lead-free single crystal materials have been shown to exhibit very large reversible strains under external electric field[2,3], however, difficulties and costs associated with crystal growth limit their applicability. Ceramic materials offer significant advantages in terms of processing, however, the total strain achievable in ceramics is much less than that obtainable in single crystals optimised for high strain applications. The limitation of achievable strain in ceramic materials results from the intergranular constraint of the polycrystal, which restricts the large anisotropic responses of the individual grains. Despite this, thorough understanding of the intergranular responses of these materials is lacking, primarily due to experimental difficulties associated with probing polycrystalline materials at this length-scale.

In this study, a variant of the grain-resolved scattering method, 3D-XRD, where the non-180° ferroelectric domain switching strain response of grains can be probed independently[4], is applied to show the phase and domain structure evolution of individual grain orientations within a bulk polycrystalline electro-ceramic under applied electric field. Such investigations provide unique information on the grain-scale electro-mechanical coupling in ceramics and are of benefit to the future engineering of high-strain actuators. Additionally, the information provided by the present measurements is applicable to a broad range of materials that strain via ferroelastic phase transformations and/or subsequent domain wall motion, such as superelastics and shape memory alloys.

The material chosen for the present study is $(0.82)Bi_{0.5}Na_{0.5}TiO_3 - (0.18)Bi_{0.5}K_{0.5}TiO_3$. $Bi_{0.5}Na_{0.5}TiO_3$ (BNT) based ceramics produced in solid solution with (among others) either $BaTiO_3$ (BT)[5], $Bi_{0.5}K_{0.5}TiO_3$ (BKT)[6], $K_{0.5}Na_{0.5}NbO_3$ (KNN)[7] or combinations thereof[8–13] have been shown to possess usable electric-field-induced

[1]School of Materials Science and Engineering, UNSW Australia, Sydney NSW 2052, Australia. [2]NEXMAP, DTU Physics, 2800 Kgs. Lyngby, Denmark. [3]European Synchrotron Radiation Facility, Grenoble 38000, France. [4]School of Mechanical and Advanced Materials Engineering, UNIST, Ulsan, Republic of Korea. Correspondence and requests for materials should be addressed to J.E.D. (email: j.daniels@unsw.edu.au)

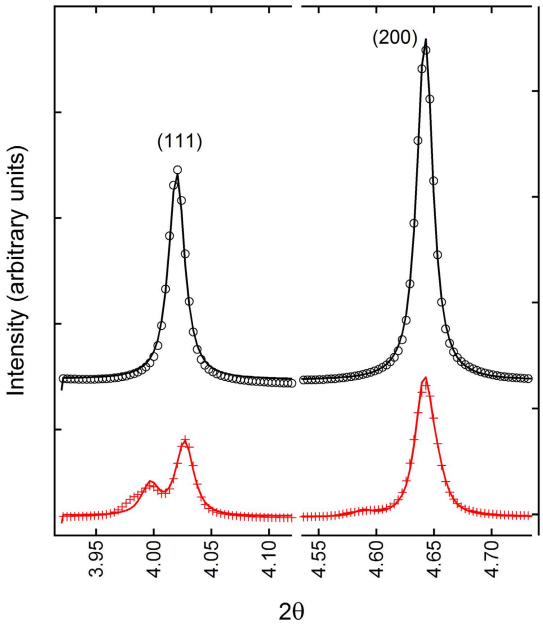

Figure 1. Powder average (111) and (002) diffraction peaks before (top) and after (bottom) the application of an electric field. The as-processed structure has single symmetric diffraction peaks expected from the pseudo-cubic phase. After the application of electric field, the sample has transformed to majority rhombohedral symmetry (splitting of the 111). The peak indices are for the pseudo-cubic perovskite structure.

strains of the order of 0.4%[14]. For given compositions, an initial pseudo-cubic non-ferroic structure has been observed to transform to a ferroic state with majority tetragonal[15], or a phase mixture of tetragonal and rhombohedral symmetries[16]. The process is irreversible under some conditions, as in the present experiments, and reversible at others[17]. The driving force for electric-field-induced transformations in a free single crystal is often attributed to a flattening of the free energy profile in the vicinity of phase boundaries[18]. Thus, the external field in this case can drive or rotate the ferroelectric polar axis within the fixed crystal orientation to align with the external field vector, resulting in multiple phase symmetries. This phase transformation can be the source of either the large useable strain, or the large remnant strain in the cases of a reversible and irreversible transformation, respectively.

Results and Discussion

Selected regions of the resulting powder diffraction patterns are shown above in Fig. 1. In the as-processed state, no peak splitting or peak shape asymmetry is observed, confirming that the materials exists in the "pseudo-cubic" state, which is often observed in this and related compositions[19]. The refined lattice parameter of this pseudo-cubic phase is found to be 3.905 Å. Once poled, the material shows a majority rhombohedral structure, with R3c lattice parameters of $a = 5.510$ Å and $c = 13.609$ Å, or in the alternatively rhombohedral setting, $a = b = c = 3.905$ Å, and $\alpha = \beta = \gamma = 89.686°$.

The 3D-XRD method allows for the indexing of many individual grains from a bulk polycrystalline material and provides direct access to grain orientation resolved information. To extract this information, the sequence of diffraction images were processed using the Fable software package[20]. The original pseudo-cubic orientation of the grains in the poled state was determined in the indexing step using GrainSpotter[21]. By applying a high completeness cut-off in terms of the number of observed reflections compared to expected reflections, the indexing can be limited to the grains that are located within the central part of the sample, which is illuminated throughout the rotation. Within the scattering volume sampled, a total of 507 grains were indexed.

In the rhombohedral structure, four possible domain variants exist with a unique spontaneous strain axis relative to the grain orientation. In order to fit the volume fractions $v_{\bar{1}11}$, $v_{1\bar{1}1}$, $v_{11\bar{1}}$ and v_{111} of these domains within each grain, individual *111* reflection sets assigned to the grain were extracted from the data volume. After correcting the intensities for the Lorentz and polarisation factors, the grain volume and the associated errors were derived. Each *111* reflection was then integrated into a radial profile along 2θ, and the radial intensity splitting was used to fit the domain volume fractions in a weighted least squares procedure with the constraint $v_{\bar{1}11} + v_{1\bar{1}1} + v_{11\bar{1}} + v_{111} = 1$ as outlined in detail by Oddershede *et al.*[4]. The diffraction experiment covered a total angular range, ω, of 320°, including Friedel pairs this gives up to 16 observations of the *111* reflection family for each grain. After fitting the domain volume fractions, the strain parallel to the electric field vector resulting

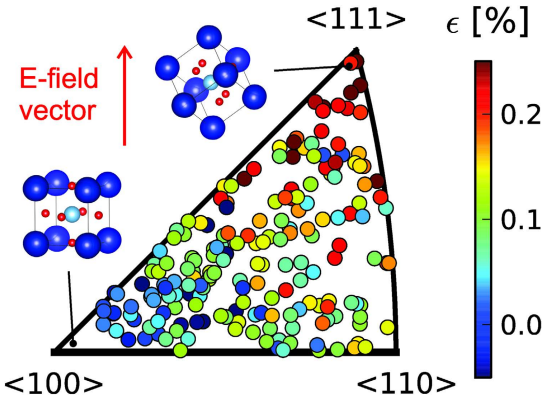

Figure 2. Inverse pole figure of indexed grain orientations. Each marker represents a single grain in the cross section of material intersected by the X-ray beam. The position on the plot represents the pseudo-cubic direction of the grain which lies parallel to the electric field vector, e.g. a grain in the bottom left of the figure has a <001> direction parallel to the electric field, while a grain in the top right has a <111> direction parallel to the electric field (see inset unit cells). The marker colour represents the calculated the non-180° ferroelectric domain switching strain along the field direction.

from the domain texture of the induced phase, ε_p, and the associated errors were determined[4,22]. In the fitting procedure and subsequent analysis, only 191 grains that satisfied the following criteria were considered: 1) at least one unique observation of a *111* reflection for each domain variant, 2) a minimum of eight observations of all possible *111* reflections in total, 3) intensity consistency between all *111* reflections of a given grain, and 4) absolute strain errors less than 0.04%. These criteria eliminate the possibility of experimental errors caused by reflection overlap and/or the associated grains rotating in and out of the illuminated volume.

The initial indexing of the total 507 grains partially or fully sampled confirmed, via a Mackenzie type analysis[23], that the measured grains represent a random distribution of orientations, as expected from the ceramic processing technique used. Figure 2 shows the orientations of the 191 grains, which satisfied the above stated consistency criteria, plotted in an inverse pole figure. Each marker represents a single grain, and its position in the diagram is representative of the pseudo-cubic direction of the grain that lies parallel to the applied electric field vector. This orientation relationship is highlighted with the prototypical ABO_3 perovskite unit cell shown by the inset diagrams of Fig. 2. The <100> corner of the inverse pole figure is relatively empty. In fact, no grains with a <001> direction within approximately 7° of the electric field vector satisfied the consistency criteria outlined above for fitting of rhombohedral domain volume fractions, despite several being initially indexed. Upon inspection of the raw diffraction data, it is concluded that this is most likely due to these grains having a significant volume fraction that either remains in the pseudo-cubic state or transforms partially to a tetragonal or other lower symmetry structure. This is consistent with the fact that related materials have field-induced symmetries that are highly sensitive to small compositional changes. For example, it is observed in the BNT-x%BT system that at a stoichiometry of approximately $x = 7$ the system transforms to a single tetragonal phase[15], while in nominal $x = 6$ compositions, a mixed phase system of tetragonal and rhombohedral symmetries exists[16]. It is therefore likely the current composition sits within a region of the phase diagram just to one side of a mixed phase region and a very slight adjustment to the stoichiometry could result in grains close to the <100> corner of the pole figure transforming to tetragonal or rhombohedral symmetry.

From Fig. 2 it's clear that there is a general trend towards maximum and minimum non-180° ferroelectric domain switching strain values occurring at grain orientations with a <111> and <100> direction lying close to the electric field vector, respectively. This is as expected, since the maximum domain switching strain results when a variant of a grains <111> directions aligns closely to the electric field vector giving a theoretical maximum strain of $\varepsilon_p = 0.547\%$ if the grain was in the saturated monodomain state. Grains with a <100> direction aligned closely to the electric field direction have the minimum strain of 0, as all <111> directions have equal angles to the applied field and a zero spontaneous strain component regardless of the domain populations. However, in addition to the observed first order correlation between grain orientation and strain there are significant variations, or second order perturbations within groups of grains of similar orientations. More interestingly, there are in fact grains that show negative non-180° ferroelectric domain switching strain components along the field direction.

To highlight these variations, the dimensionality of the representation is reduced by showing in Fig. 3(a) the measured (grey with error bars) non-180° ferroelectric domain switching strains resolved in the direction of the electric-field vector for each grain as a function of $\cos^2\phi_{111}$, where ϕ_{111} is the misorientation between the electric field vector and the closest <111> direction in the given grain. Here it is clear that individual grain behaviour varies significantly, and is not dictated solely by the orientation of the grain relative to the applied field vector. To

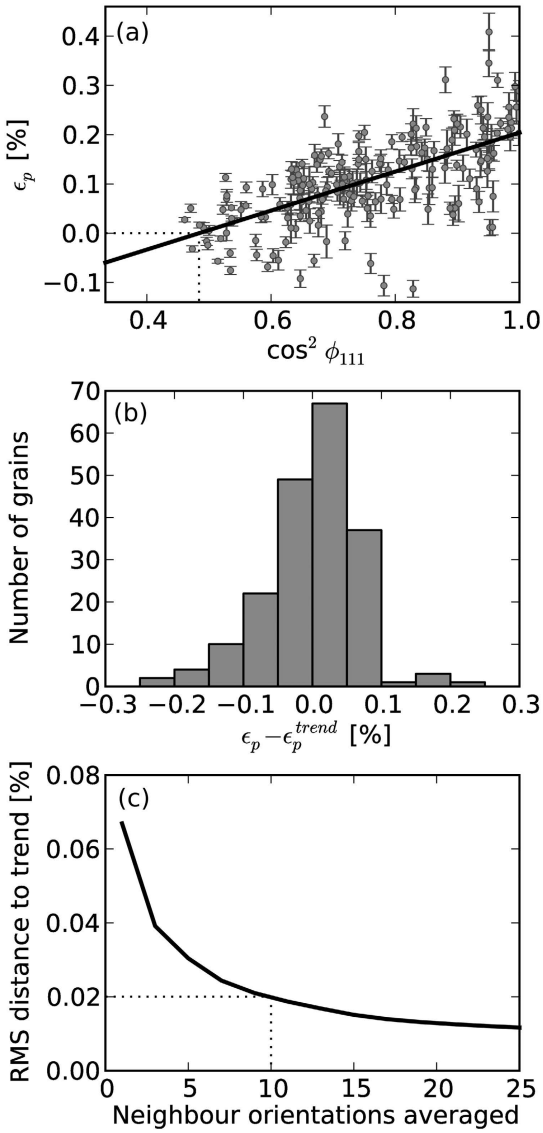

Figure 3. (**a**) domain switching strains along the poling direction as a function of $\cos^2\phi_{111}$, where ϕ_{111} is the misorientation between the electric field vector and the closest $<111>$ direction in the grain, (**b**) distribution of actual domain switching strains away from average behaviour, and (**c**) RMS distance to the trend line in (**a**) as a function of group size when averaging over groups of grains with similar orientations. Based on this it is concluded that the local grain-scale deviations average out over approximately 10–20 grains.

more clearly observe the magnitude of the deviation away from average behaviour, the difference between the calculated strain, and that expected from average behaviour is shown in Fig. 3(b).

These deviations in resultant non-180° ferroelectric domain switching strain in the field-induced phase must be accommodated to some extent by lattice strains of the grains. Such lattice strains may arise from a combination of the intrinsic piezoelectric effect and elastic compliance strains[24], both of which are highly anisotropic with respect to the crystallographic direction. Deconvolution of these two mechanisms is not possible with the current data, however, future extensions to X-ray microscopy methods that allow direct probing of the strain of individual domains may facilitate this[25]. The outlier grains on the strain magnitude distribution likely experience very large intergranular stresses with their neighbours, and thus, are perhaps sources of crack initiation which may lead to reduced fatigue lifetimes upon cycling. Detailed analysis of these individual neighbour interactions is not possible

in the current study, as the combination of grain size and detector resolution does not allow for reconstruction of the spatial distribution of grains, but investigations of this type may become possible in the future by expanding on existing grain mapping techniques[26–28].

The present results provide quantitative measures of the local grain-scale deviations from the bulk average strain response of the piezoelectric ceramic material. The microstructural origins of this grain-scale heterogeneity lie in several possible areas which are likely acting in parallel. Firstly, the highly anisotropic piezoelectric response of these materials will cause the local stress environment of each grain to be different. The domain switching response of the individual grain is thus limited (or enhanced) by the total piezoelectric strain response of the surrounding grains. Secondly, dielectric anisotropy creates inhomogeneous field magnitudes at any point within a polycrystalline material. These inhomogeneous fields have been suggested to cause distributions of domain switching times in related piezoelectric ceramics[29]. Finally, it is often observed in ferroelectric/ferroelastic polycrystals that domain morphologies differ significantly at grain boundaries and in some cases propagate through the boundary[30]. This is a result of the very high electro-static energy resulting from non head-to-tail domain configurations that would inevitably form at grain boundaries between two randomly oriented grains with random domain structures. It may be that this electrostatic energy outweighs the elastic energy required to compensate for the non-uniform strain resulting from continuity of domain walls between grains. Such domain sharing may lead to grain-scale collective dynamics in bulk materials, similar to that observed in polycrystalline films[31,32]. The total system energy will therefore include a combination of electrostatic potential at the grain boundaries and the elastic strain energy associated with compensating the anisotropic non-180° ferroelectric domain switching strain during the phase transformation. The requirement for balance between these effects to minimise the global energy of the polycrystalline system ensures that polycrystalline ferroelectrics are highly inhomogeneous at the grain scale.

A critical question that arises from such a result is at what length-scale, or over how many grains, do these local deviations average out? This length-scale will be particularly important when considering the validity of modelling efforts of bulk materials at the granular and sub-granular scale. In order to quantify this, the measured grains are grouped into nearest orientation neighbours and the groups then compared to the overall trend behaviour for all grains. This is displayed in Fig. 3(c) as the RMS distance to overall trend as a function of grouped grain neighbours. When just single isolated grains are taken, the distribution has a RMS difference to the mean of 0.067%. It can be seen that the difference between the group of grains and the general trend reduces rapidly as the total number of grains included increases. Here, it appears as though the grain clusters approach the bulk average behaviour (i.e. RMS value asymptotes) at cluster sizes between 10 and 20 grains.

In summary, it is shown that in a polycrystalline ceramic of $(0.82)Bi_{0.5}Na_{0.5}TiO_3 - (0.18)Bi_{0.5}K_{0.5}TiO_3$, the grain orientation relative to the applied electric field influences the resulting phase and domain structure of the electric-field-induced phase. In this particular composition, most grains were found to transform to a rhombohedral symmetry, while grains with a $<100>$ direction within 7° of the applied field vector displayed a significant volume fraction that either remained in the cubic state or transformed partially to a tetragonal or other lower symmetry structure. Of the grains that transformed to a rhombohedral symmetry, a variation in the resulting domain texture existed which had the trend from less to more saturated when the $<100>$ and $<111>$ directions of a grain were aligned with the field vector, respectively. However, significant deviations in the magnitude of the response exist at the grain scale, as evidenced by the large variation in resulting domain texture strains observed for grains of similar orientations. The length-scale on which these local variations average out is likely of the order of 10–20 grains. The origin of these deviations is suggested to result from complex interactions of grain-neighbour strain magnitudes, electric field magnitude inhomogeneities and the interaction of ferroic domains at the grain boundaries. These results are of critical importance when considering the validity of grain-scale modelling efforts, and provide additional considerations in the design of novel electro-mechanical materials.

Methods

Samples of $(0.82)Bi_{0.5}Na_{0.5}TiO_3 - (0.18)Bi_{0.5}K_{0.5}TiO_3$ were produced by the mixed oxide route. Details of the synthesis method can be found elsewhere[33]. The resulting grain size of the samples was approximately 3–5 μm. A sample was cut and polished into a rectangular shape of dimensions $100 \times 200 \times 90\,\mu m^3$. Gold electrodes were sputtered onto two opposing $100 \times 200\,\mu m^2$ surfaces. The sample was then placed with an electrode surface in contact with a brass pin and electrically contacted using silver paint. A top electrode wire was connected using silver paint and the sample encapsulated in a 1 mm diameter Kapton tube filled with silicone oil. Such a setup allows the application of high electric fields without the risk of dielectric breakdown[34].

X-ray diffraction experiments were performed at beamline ID11 of the European Synchrotron Radiation Facility. A beam energy of 78.40 keV and dimensions 50 μm in width × 5 μm in height was produced at the sample position. The planar beam transmits through the sample such that it interacts with a limited number of grains creating "spotty" diffraction images. The sample was then rotated around and axis perpendicular to the incident beam, ω, with data collected over 2 × 160° in 0.25° integration angles. A schematic diagram of the 3D-XRD setup can be found in Oddershede[4]. For more details of the data collection strategy see Poulsen[35]. After the collection of an initial data set in the as-processed state, the sample was electrically poled with a field of 4 kV/mm and a subsequent data set collected.

Unit cell parameters for the as-processed and poled materials were found from full pattern refinements using Topas V4.1. The powder diffraction data were generated by creating a sum of all diffraction images recorded as a function of sample rotation angle, ω, and then integrating the resulting 2D diffraction patterns in azimuthal angle, η.

References

1. Rödel, J. *et al.* Perspective on the Development of Lead-Free Piezoceramics. *J. Amer. Ceram. Soc.* **92,** 1153–1177 (2009).
2. Park, S.-E. & Shrout, T. R. Ultrahigh strain and piezoelectric behavior in relaxor based ferroelectric single crystals. **82,** 1804–1811 (1997).
3. Schneider, D., Jo, W., Rödel, J., Rytz, D. & Granzow, T. Anisotropy of ferroelectric behavior of $(1-x)Bi_{1/2}Na_{1/2}TiO_3$–$xBaTiO_3$ single crystals across the morphotropic phase boundary. *J. Appl. Phys.* **116,** 044111 (2014).
4. Oddershede, J. *et al.* Quantitative grain-scale ferroic domain volume fractions and domain switching strains from three-dimensional X-ray diffraction data. *J. Appl. Cryst.* **48,** 882–889 (2015).
5. Takenaka, T., Maruyama, K. & Sakata, K. $(Bi_{1/2}Na_{1/2})TiO_3$-$BaTiO_3$ System for Lead-Free Piezoelectric Ceramics. **30,** 2236–2239 (1991).
6. Sasaki, A., Chiba, T., Mamiya, Y. & Otsuki, E. Dielectric and Piezoelectric Properties of $(Bi_{0.5}Na_{0.5})TiO_3$ –$(Bi_{0.5}K_{0.5})TiO_3$ Systems. *Jpn. J. Appl. Phys.* **38,** 5564–5567 (1999).
7. Kounga, A. B., Zhang, S. T., Jo, W., Granzow, T. & Rödel, J. Morphotropic phase boundary in (1-x)$Bi_{0.5}Na_{0.5}TiO_3$-$xK_{0.5}Na_{0.5}NbO_3$ lead-free piezoceramics. **92,** 222902 (2008).
8. Makiuchi, Y., Aoyagi, R., Hiruma, Y., Nagata, H. & Takenaka, T. $(Bi_{1/2}Na_{1/2})TiO_3$-$(Bi_{1/2}K_{1/2})TiO_3$-$BaTiO_3$-Based Lead-Free Piezoelectric Ceramics. *Jpn. J. Appl. Phys.* **44,** 4350 (2005).
9. Nagata, H., Yoshida, M., Makiuchi, Y. & Takenaka, T. Large Piezoelectric Constant and High Curie Temperature of Lead-Free Piezoelectric Ceramic Ternary System Based on Bismuth Sodium Titanate-Bismuth Potassium Titanate-Barium Titanate near the Morphotropic Phase Boundary. *Jpn. J. Appl. Phys.* **42,** 7401–7403 (2003).
10. Shieh, J., Wu, K. C. & Chen, C. S. Switching characteristics of MPB compositions of $(Bi_{0.5}Na_{0.5})TiO_3$–$BaTiO_3$–$(Bi_{0.5}K_{0.5})TiO_3$ lead-free ferroelectric ceramics. *Acta Mater.* **55,** 3081–3087 (2007).
11. Seifert, K. T. P., Jo, W. & Rödel, J. Temperature-Insensitive Large Strain of $(Bi_{1/2}Na_{1/2})TiO_3$–$(Bi_{1/2}K_{1/2})TiO_3$–$(K_{0.5}Na_{0.5})NbO_3$ Lead-Free Piezoceramics. *J. Am. Ceram. Soc.* **93,** 1392 (2010).
12. Shrout, T. R. & Zhang, S. J. Lead-free piezoelectric ceramics: Alternatives for PZT? *J Electroceram* **19,** 111–124 (2007).
13. Zhang, S. T., Kounga, A. B., Aulbach, E., Ehrenberg, H. & Rodel, J. Giant Strain in Lead-Free Piezoceramics $Bi_{0.5}Na_{0.5}TiO_3$-$BaTiO_3$-$K_{0.5}Na_{0.5}NbO_3$ System. *Appl. Phys. Lett.* **91,** 112906 (2007).
14. Jo, W. *et al.* Giant electric-field-induced strains in lead-free ceramics for actuator applications – status and perspective. *J Electroceram* **29,** 71–93 (2012).
15. Daniels, J. E., Jo, W., Rödel, J. & Jones, J. L. Electric-field-induced phase transformation at a lead-free morphotropic phase boundary: Case study in a 93%$(Bi_{0.5}Na_{0.5})TiO_3$ – 7%$BaTiO_3$ piezoelectric ceramic. *Appl. Phys. Lett.* **95,** 032904 (2009).
16. Simons, H. *et al.* Electric-field-induced strain mechanisms in lead-free 94%$(Bi_{1/2}Na_{1/2})TiO_3$–6%$BaTiO_3$. **98,** 082901 (2011).
17. Hinterstein, M. *et al.* Field-induced phase transition in $Bi_{1/2}Na_{1/2}TiO_3$-based lead-free piezoelectric ceramics. *J. Appl. Crystallogr.* **43,** 1314–1321 (2010).
18. Damjanovic, D. Comments on Origins of Enhanced Piezoelectric Properties in Ferroelectrics. *IEEE Trans. Ultrason. Ferroelectr. Freq. Control* **56,** 1574–1585 (2009).
19. Daniels, J. E., Jo, W., Rödel, J., Honkimäki, V. & Jones, J. L. Electric-field-induced phase-change behavior in $(Bi_{0.5}Na_{0.5})TiO_3$-$BaTiO_3$-$(K_{0.5}Na_{0.5})NbO_3$: A combinatorial investigation. *Acta Mat.* **58,** 2103–2111 (2010).
20. *Fable: A software framework for doing grain mapping experiments in materials science at a synchrotron*, URL http://sourceforge.net/p/fable/wiki/
21. Schmidt, S. GrainSpotter: a fast and robust polycrystalline indexing algorithm. *J. Appl. Cryst.* **47,** 276–284 (2014).
22. Hall, D. A., Steuwer, A., Cherdhirunkorn, B., Mori, T. & Withers, P. J. Analysis of elastic strain and crystallographic texture in poled rhombohedral PZT ceramics. *Acta Mat.* **54,** 3075–3083 (2006).
23. Mackenzie, J. K. Second paper on statistics associated with the random disorientation of cubes. *Biometrika* **45,** 229–240 (1958).
24. Pramanick, A., Damjanovic, D., Nino, J. E. D. J. C. & Jones, J. L. Origins of electro-mechanical coupling in polycrystalline ferroelectrics during subcoercive electrical loading. *J. Amer. Ceram. Soc.* **94,** 293–309 (2011).
25. Simons, H. *et al.* Dark-field X-ray microscopy for multiscale structural characterization. *Nature Comm.* **6,** 6098 –6103 (2015).
26. Reischig, P. *et al.* Advances in X-ray diffraction contrast tomography: flexibility in the setup geometry and application to multiphase materials. *J. Appl. Cryst.* **46,** 297–311 (2013).
27. Schmidt, S. *et al.* Direct observation of 3-D grain growth in Al-0.1% Mn. *Scripta Mat.* **59,** 491–494 (2008).
28. Schuren, J. C. *et al.* New opportunities for quantitative tracking of polycrystal responses in three dimensions. *Curr. Opin. Solid St. M.* **19,** 235–244 (2015).
29. Genenko, Y. A. *et al.* Universal Polarization Switching Behavior of Disordered Ferroelectrics. **22,** 2058–2066 (2012).
30. Tsurekawa, S., Ibaraki, K., Kawahara, K. & Watanabe, T. The continuity of ferroelectric domains at grain boundaries in lead zirconate titanate. *Scripta Mat.* **56,** 577–580 (2007).
31. Bintachitt, P. *et al.* Collective dynamics underpins Rayleigh behavior in disordered polycrystalline ferroelectrics. **107,** 7219–7224 (2010).
32. Wicks, S. *et al.* Collective dynamics in nanostructured polycrystalline ferroelectric thin films using local time-resolved measurements and switching spectroscopy. *Acta Mat.* **58,** 67–75 (2010).
33. Dittmer, R., Jo, W., Daniels, J., Schaab, S. & Rodel, J. Relaxor Characteristics of Morphotropic Phase Boundary $(Bi_{1/2}Na_{1/2})TiO_3$-$(Bi_{1/2}K_{1/2})TiO_3$ Modified with $Bi(Zn_{1/2}Ti_{1/2})O_3$. *J. Am. Ceram. Soc.* **94,** 4283–4290 (2011).
34. Daniels, J. E., Pramanick, A. & Jones, J. L. Time-resolved characterization of ferroelectrics using high-energy X-ray diffraction. **56,** 1539–1545 (2008).
35. Poulsen, H. F. *et al.* Three-dimensional maps of grain boundaries and the stress state of individual grains in polycrystals and powders. **34,** 751–756 (2001).

Acknowledgements

The authors acknowledge support from the Danish Independent Research Council | Technology and Production Sciences case no. 12-127449 and Australian Research Council Discovery Project DP120103968. The Danish Independent Research Council | Natural Sciences is acknowledged for covering expenses in relation to the synchrotron experiment (through Danscatt). The European Synchrotron Radiation Facility is acknowledged for granting experimental beamtime. JED acknowledges support from an Australian Institute of Nuclear Science and Engineering research fellowship and travel funding provided by the International Synchrotron Access Program (ISAP) managed by the Australian Synchrotron and funded by the Australian Government.

Author Contributions

J.O. and J.D. initiated the project and designed the experiments with S.S. Samples were prepared by Q.C. and W.J. and experiments performed by J.D., M.M., Q.C., J.W. and J.O. Data analysis was done by J.O. who also interpreted the results with J.D., M.M. and S.S. The manuscript draft was prepared by J.D. and all Authors contributed to its final text.

Additional Information

Competing financial interests: The authors declare no competing financial interests.

How to cite this article: Daniels, J. E. *et al.* Heterogeneous grain-scale response in ferroic polycrystals under electric field. *Sci. Rep.* **6**, 22820; doi: 10.1038/srep22820 (2016).